

**Universidade Federal do Rio Grande – FURG**  
**Instituto de Oceanografia**  
Programa de Pós-Graduação em Oceanologia

**A INFLUÊNCIA DO DIPOLO SUBTROPICAL  
DO ATLÂNTICO SUL NA DINÂMICA DE  
RESSURGÊNCIA COSTEIRA AO LONGO  
DAS COSTAS SUDESTE-SUL DO BRASIL E  
SUDOESTE DA ÁFRICA**

Luiz Henrique Oliveira da Silva

Dissertação apresentada ao Programa  
de Pós-Graduação em Oceanologia,  
como parte dos requisitos para  
obtenção do Título de Mestre.

Orientador: *Prof.* Dr. José Luiz Lima de Azevedo

Rio Grande, RS, Brasil  
Abril de 2020

# **A INFLUÊNCIA DO DIPOLO SUBTROPICAL DO ATLÂNTICO SUL NA DINÂMICA DE RESSURGÊNCIA COSTEIRA AO LONGO DAS COSTAS SUDESTE-SUL DO BRASIL E SUDOESTE DA ÁFRICA**

Dissertação apresentada ao Programa de Pós-Graduação em Oceanologia,  
como parte dos requisitos para a obtenção do Título de Mestre

por

**Luiz Henrique Oliveira da Silva**

Rio Grande, RS, Brasil  
Abril de 2020

© A cópia parcial e citação de trechos dessa tese são permitidas sobre a condição de que qualquer pessoa que a consulte reconheça os direitos autorais do autor. Nenhuma informação derivada direta e indiretamente desta obra deve ser publicada sem o consentimento prévio e por escrito do escritor.

da Silva, Luiz Henrique Oliveira

Influência do Dipolo Subtropical do Atlântico Sul na Dinâmica de Ressurgência Costeira ao Longo das Costas Sudeste-Sul do Brasil e Sudoeste da África./ Luiz Henrique Oliveira da Silva. - Rio Grande: FURG, 2020.

Número de páginas p. 84

Dissertação – Universidade Federal do Rio Grande. Mestrado em Oceanologia. Área de Concentração: Física dos Oceanos e Clima.

1. Dipolo Subtropical do Atlântico Sul. 2. Ressurgência Costeira 3. Costa Sudeste-sul do Brasil. 4. Costa Sudoeste Africana. 5. Anéis das Agulhas. I. Título. Influência do Dipolo Subtropical do Atlântico Sul na Dinâmica de Ressurgência Costeira ao Longo das Costas Sudeste-Sul do Brasil e Sudoeste da África



UNIVERSIDADE FEDERAL DO RIO GRANDE - FURG  
IO - INSTITUTO DE OCEANOGRAFIA  
PROGRAMA DE PÓS-GRADUAÇÃO EM OCEANOLOGIA  
E-mail: [ccofoaa@furg.br](mailto:ccofoaa@furg.br) - home-page: [www.ppgoo.furg.br](http://www.ppgoo.furg.br)



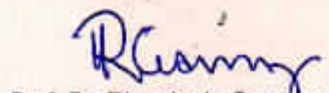
## ATA ESPECIAL DE DEFESA DE DISSERTAÇÃO DE MESTRADO - 03/2020

Às 14:00h do dia 23 de abril do ano de dois mil e vinte, no LEOC - FURG/Carreiros, reuniu-se a Comissão Examinadora da Dissertação de **MESTRADO** intitulada "**A Influência do Dipolo Subtropical do Atlântico Sul na Dinâmica de Ressurgência Costeira ao Longo das Costas Sul/Sudeste do Brasil e Sudoeste da África**", do **Acad. Luiz Henrique Oliveira da Silva**. A Comissão Examinadora foi composta pelos seguintes membros: Prof. Dr. José Luiz Lima de Azevedo - (Orientador- IO-FURG), Prof. Dr. Mauricio Magalhães Mata (IO/FURG), Prof. Dr. Leopoldo Rota de Oliveira (IO-FURG) e Prof. Dr. Ricardo de Camargo (USP). Dando início à reunião, o Presidente da Sessão, Prof. Dr. José Luiz Lima de Azevedo, agradeceu a presença de todos; e fez a apresentação da Comissão Examinadora. Logo após, esclareceu que o Candidato terá de 45 a 60 min para explanação do tema, e cada membro da Comissão Examinadora, um tempo máximo de 30 min para perguntas. A seguir, passou à palavra ao Candidato, que apresentou o tema e respondeu às perguntas formuladas. Após ampla explanação, a Comissão Examinadora reuniu-se em reservado para discussão do conceito a ser atribuído ao Candidato. Foi estabelecido que as sugestões de todos os membros da Comissão Examinadora, que seguem em pareceres em anexo, foram aceitas pelo Orientador/Candidato para incorporação na versão final da Dissertação. Finalmente, a Comissão Examinadora considerou o candidato Aprovado por unanimidade. Nada mais havendo a tratar, foi lavrada a presente ATA, que após lida e aprovada, será assinada pela Comissão Examinadora, pelo Candidato e pelo Coordenador o Programa de Pós-Graduação em Oceanologia (PPGO).

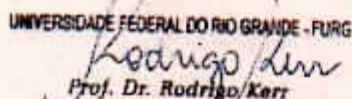
Prof. Dr. José Luiz Lima de Azevedo  
Presidente

  
Prof. Dr. Mauricio Magalhães Mata

  
Prof. Dr. Leopoldo Rota de Oliveira

  
Prof. Dr. Ricardo de Camargo

  
Acad. Luiz Henrique O. da Silva

UNIVERSIDADE FEDERAL DO RIO GRANDE - FURG  
  
Prof. Dr. Rodrigo Kerr  
Instituto de Oceanografia

Prof. Dr. Rodrigo Kerr  
Coordenador PPGO

# Agradecimentos

Meus infinitos agradecimentos aos meus pais e meu irmão. Esses nunca deixaram de me apoiar e me ajudar a manter uma saúde mental que me permitisse realizar este trabalho. Pode ser clichê, mas, com certeza, sem eles nada disso seria possível.

Agradeço aos ex-colegas de laboratório DinaMO, Dr. Rodrigo Mogollón e Claus Toledo, os quais desprenderam inúmeras horas para discutir sobre oceanografia, seja no laboratório, em casa, na praia ou qualquer lugar que estivessemos.

Ainda do DinaMO, laboratório onde dei início a essa dissertação, agradeço ao Prof. Paulo Calil, quem me incentivou e me auxiliou nos primeiros movimentos deste trabalho.

Aos maravilhosos eternos amigos que a oceanografia me trouxe, Pedro e Walkiria. Indescritível o que ter pessoas maravilhosas como esses dois por perto. Pessoas que sabe exatamente o que fazer nas situações mais obscuras em que me perdi pelo caminho. Estavam nos meus agradecimentos do TCC, estão aqui e tenho certeza absoluta que nossa amizade vai levá-los até o momento em que eu escrever os agradecimentos do doutorado. Um amor muito grande por esses dois. Muito obrigado!

Agradeço ao Laboratório de Estudo dos Oceanos e Clima, que me propiciou a infraestrutura necessária após o período que deixei o DinaMO. Em conjunto ao LEOC, agradeço ao prof. José Luiz, quem abraçou a ideia no meio do caminho e fez com que se tornasse o resultado final que aqui chegamos. Uma gigantesca pessoa, um amigo que fiz nesse último ano.

Por fim, agradeço ao PPGO que não permitiu com que o trabalho acabasse no meio do caminho e correu atrás da manutenção da minha bolsa. Agradeço também a CAPES pelo financiamento através de bolsa de estudo de Mestrado ao longo dos 24 meses.

# Índice

<b>Agradecimentos</b> .....	IV
<b>Lista de Figuras da Dissertação</b> .....	VII
<b>Lista de Figuras do Artigo</b> .....	VIII
<b>Lista de Acrônimos e Abreviações</b> .....	XI
<b>Resumo</b> .....	XIII
<b>Abstract</b> .....	XV
<b>Capítulo I: Introdução</b> .....	1
1.1. Ressurgência Costeira.....	1
1.2. Ressurgência Costeira no Oceano Atlântico Sul.....	3
1.3. Dipolo Subtropical do Atlântico Sul.....	10
1.4. Área de Estudo.....	13
<b>Capítulo II: Objetivos</b> .....	16
2.1. Objetivo Geral.....	16
2.2. Objetivos Específicos.....	16
<b>Capítulo III: Materiais e Métodos</b> .....	17
3.1. Produtos Utilizados.....	17
3.1.1. Reanálises Atmosféricas.....	17
3.1.2. Reanálises Oceânicas.....	18
3.1.3. Concentração de Clorofila-a.....	18
3.2. Metodologia.....	19
3.2.1. Índice do DSAS.....	20
3.2.2. Dinâmica de Ressurgência.....	20
3.2.3. Fluxo Líquido de Calor.....	22
3.2.4. Parâmetro de Estratificação.....	22
3.2.5. Composições.....	23
3.2.6. Clorofila-a.....	24
<b>Capítulo IV: Artigo Científico</b> .....	26
1. Introduction.....	26
2. Methods.....	33
2.1. Reanalysis Products.....	33
2.2. Methodology.....	34

3. Results and Discussion.....	37
3.1. Southern-South Brazilian Coast.....	39
3.1.1. Positive SASD.....	39
3.1.2. Negative SASD.....	46
3.2. Southwestern African Coast.....	53
3.2.1. Positive SASD.....	54
3.2.2. Negative SASD.....	63
4. Conclusions.....	69
<b>Capítulo V: Síntese da Discussão e Conclusões.....</b>	<b>72</b>
<b>Referências Bibliográficas.....</b>	<b>77</b>



# Lista de Figuras da Dissertação

**Figura 1:** Esquema simplificado da interação entre o vento e os oceanos, para o hemisfério Sul. Inicialmente, a) o vento sopra paralelo a direção da costa (vetor verde), b) ocasionando o transporte integrado horizontal de Ekman à esquerda da direção do vento (vetor azul), o que resulta em c) advecção vertical positiva (em direção a superfície) de águas de subsuperfície (vetor lilás).....**pág. 1**

**Figura 2:** Esquematização, para o hemisfério Sul, da dinâmica de subsidência e ressurgência associadas ao rotacional da tensão de cisalhamento do vento. a-c) o rotacional do vento será positivo, indicando convergência, quando o vento possuir uma tendência de rotação anti-horária, resultando em velocidades verticais negativas da água na base da camada de Ekman. b-d) o rotacional do vento será negativo, indicando divergência, quando o vento possuir uma tendência de rotação horária, resultando em velocidades verticais positivas da água na base da camada de Ekman.....**pág. 3**

**Figura 3:** Circulação superficial do oceano Atlântico Sul. Vetores representam as direções das principais correntes. O sistema do grande Giro subtropical é representado pela coloração rosa claro, em verde é representado o sistema da Corrente Circumpolar Antártica. Abreviações: Frente Angola-Benguela (ABF), Frente Brasil-Malvinas (BCF), Frente Subtropical (STF), Frente Subantártica (SAF), Frente Polar (PF). Retirado de Tomczack & Godfrey [2003].....**pág. 4**

**Figura 4:** Padrão climatológico de a) pressão ao nível do mar (PNM, hPa), mostrada na forma de isóbaras e b) da intensidade ( $m.s^{-1}$ ) e direção dos ventos para o período de 1993 a 2018 sobre o oceano Atlântico Sul. Médias climatológicas calculadas utilizando dados de reanálise ERA-Interim.....**pág. 6**

**Figura 5:** Representação do desenvolvimento da fase positiva do DSAS. a) O processo se inicia com a intensificação da ASAS e deslocamento desta para sul, modificando o sistema de vento, b) o que resulta em anomalias no fluxo de calor latente para a atmosfera ( $\delta QLH$ ). c) Este último, por sua vez, altera a profundidade da camada de mistura ( $\delta MLD$ ), d) contribuindo para o enfraquecimento (intensificação) da contribuição da radiação solar (QSW). Retirado de Morioka *et al.* [2011].....**pág. 11**

**Figura 6:** Padrão climatológico da intensidade (cores de fundo) e direção dos ventos (vetores) sobre o oceano Atlântico Sul para o período de 1993-2018. Os retângulos em magenta indicam as áreas de estudo da costa sudeste-sul do Brasil (CSB) e da costa sudoeste africana (CSA). As caixas em preto contornam as áreas do polo nordeste ( $15^{\circ}S - 25^{\circ}S$  e  $0^{\circ}W - 20^{\circ}W$ ) e do polo sudoeste ( $30^{\circ}S - 40^{\circ}S$  e  $10^{\circ}W - 30^{\circ}W$ ) das quais foram calculadas as médias espaciais das anomalias da temperatura da superfície do mar (TSM) aplicadas no cálculo do índice do Dipolo Subtropical do Atlântico Sul (IDSAS).....**pág. 13**

**Figura 7:** Em a) e b) padrão climatológico da TSM das regiões demarcadas pelos retângulos em magenta da CSB e da CSA na figura 6, respectivamente. Os traços em magenta indicam as seções utilizadas neste estudo para Cabo Frio (CFB) e Cabo Santa Marta (CSM) na CSB e Cape Frio (CFN) e Santa Helena Bay (SHB) na CSA. As climatologias foram calculadas utilizando os produtos de TSM ESA-CCI.....**pág. 14**



# Lista de Figuras do Artigo

**Fig. 1.** a) Climatological pattern of intensity (shading) and wind direction (vectors) over the South Atlantic Ocean for the period 1993-2018. The magenta rectangles indicate the study areas of the Southeast-South Brazilian coast (SBC) and the Southwest African coast (SAC). The black boxes outline the areas of the northeast pole (15°S - 25°S and 0°W - 20°W) and the southwest pole (30°S - 40°S and 10°W - 30°W) from which the spatial averages of sea surface temperature (SST) anomalies were calculated and applied in the calculation of the South Atlantic Subtropical Dipole index (SASDI). In b) and c) climatological pattern of SST of the regions demarcated by the magenta rectangles of SBC and SAC in a), respectively. The magenta lines indicate the sections used in this study for Cabo Frio (CFB) and Cabo Santa Marta (CSM) at SBC and Cape Frio (CFN) and Santa Helena Bay (SHB) at SAC. The climatology shown in a) was calculated using the ERA-Interim products and in b) and c) through the SST ESA-CCI products.....**pág. 31**

**Fig. 2.** SASDI time series computed based on Morioka *et al.* [2011], using ERAI SST products. The horizontal red (blue) line represents the SASDI = +0.8 °C (SASDI = -0.8 °C) thresholds.....**pág. 39**

**Fig. 3.** Neutral composites (October-December) of a) the intensity (shading) and direction (vectors) of the wind ( $m.s^{-1}$ ), b) the intensity (shading) and direction (vectors) of the Ekman transport ( $M_H$ , in  $m^2.s^{-1}$ ) and c) the Ekman pumping ( $W_{EK}$ ,  $m.day^{-1}$ ) for the southeastern-south Brazilian coast (SBC). The lower figures show the difference between the SASD+ and neutral composites of d) intensity (shading) and direction (vectors) of the wind speed ( $\Delta WSPD$ ,  $m.s^{-1}$ ), e) the intensity (shading) and direction (vectors) of Ekman transport ( $\Delta M_H$ ,  $m^2.s^{-1}$ ) and the f) Ekman pumping ( $\Delta W_{EK}$ ,  $m.day^{-1}$ ). The solid black lines in the lower figures indicate the regions with significant differences for the 80% confidence interval. In f) the dashed contour line show the position in c) where  $W_{EK} = 0$ .....**pág. 40**

**Fig. 4.** a) Neutral years composite (October-December) of the net heat flux (NHF, in  $W.m^{-2}$ ) and b) SASD+ anomalies composite of the NHF ( $\Delta NHF$ , in  $W.m^{-2}$ ) in the southeastern-south Brazilian coast (SBC). Positive values in a) indicate a NHF from the atmosphere to the ocean.....**pág. 42**

**Fig. 5.** a) Cabo Frio (CFB) and b) Cabo Santa Marta (CSM) time series of the neutral composites of the chlorophyll-a (chl-a, green line, in  $mg.m^{-3}$ ), Ekman pumping ( $W_{EK}$ , blue line, in  $m.day^{-1}$ ) and stratification parameter  $\Phi$  calculated according to equation 5 of the text ( $\Phi$ , red line, in  $J.m^{-3}$ ). In c) and d) the time of the SASD+ anomalies composite of the same variables ( $\Delta chl-a$ ,  $\Delta W_{EK}$ ,  $\Delta \Phi$ ) as a) and b). The time series were smoothed with a 3-month moving average filter.....**pág. 43**

**Fig. 6.** Vertical section of a) the neutral years composite (December-February) and b) the SASD+ anomalies composite of the water column temperature (T, in °C) at Cabo Frio (CFB). The dashed line show the 18 °C isotherm (SACW <18°C) of a) the neutral years composite and b) the SASD+ events composite.....**pág. 45**

**Fig. 7.** Vertical section of a) the neutral years composite (December-February) and b) the SASD+ anomalies composite of the water column temperature (T, in °C) at Cabo Santa Marta (CSM). The dashed line show the 18 °C isotherm (SACW <18°C) of a) the neutral years composite and b) the SASD+ events composite.....**pág. 46**

**Fig. 8.** Neutral composites (October-December) of a) the intensity (shading) and direction (vectors) of the wind ( $m.s^{-1}$ ), b) the intensity (shading) and direction (vectors) of the Ekman transport ( $M_H$ , in  $m^2.s^{-1}$ ) and c) the Ekman pumping ( $W_{EK}$ ,  $m.day^{-1}$ ) for the southeastern-south Brazilian coast (SBC). The lower figures show the difference between the SASD- and neutral composites of d) intensity (shading) and direction (vectors) of the wind speed ( $\Delta WSPD$ ,  $m.s^{-1}$ ), e) the intensity (shading) and direction (vectors) of Ekman transport ( $\Delta M_H$ ,  $m^2.s^{-1}$ ) and the f) Ekman pumping ( $\Delta W_{EK}$ ,  $m.day^{-1}$ ). The solid black lines in the lower figures indicate the regions with significant differences for the 80% confidence interval. In f) the dashed contour line show the position in c) where  $W_{EK} = 0$ .....**pág. 47**

**Fig. 9.** a) Neutral years composite (October-December) of the net heat flux (NHF, in  $W.m^{-2}$ ) and b) SASD- anomalies composite of the NHF ( $\Delta NHF$ , in  $W.m^{-2}$ ) in the southeastern-south Brazilian coast (SBC). Positive values in a) indicate a NHF from the atmosphere to the ocean. The solid black lines indicate the regions with significant differences for the 80% confidence interval.....**pág. 49**

**Fig. 10.** a) Cabo Frio (CFB) and b) Cabo Santa Marta (CSM) time series of the neutral composites of the chlorophyll-a (chl-a, green line, in  $mg.m^{-3}$ ), Ekman pumping ( $W_{EK}$ , blue line, in  $m.day^{-1}$ ) and stratification parameter  $\Phi$  calculated according to equation 5 of the text ( $\Phi$ , red line, in  $J.m^{-3}$ ). In c) and d) the time of the SASD- anomalies composite of the same variables ( $\Delta chl-a$ ,  $\Delta W_{EK}$ ,  $\Delta \Phi$ ) as a) and b). The time series were smoothed with a 3-month moving average filter.....**pág. 51**

**Fig. 11.** Vertical section of a) the neutral years composite (December-February) and b) the SASD- anomalies composite of the water column temperature ( $T$ , in  $^{\circ}C$ ) at Cabo Frio (CFB). The dashed line show the  $18^{\circ}C$  isotherm (SACW  $<18^{\circ}C$ ) of a) the neutral years composite and b) the SASD- events composite.....**pág. 52**

**Fig. 12.** Vertical section of a) the neutral years composite (December-February) and b) the SASD- anomalies composite of the water column temperature ( $T$ , in  $^{\circ}C$ ) at Cabo Santa Marta (CSM). The dashed line show the  $18^{\circ}C$  isotherm (SACW  $<18^{\circ}C$ ) of a) the neutral years composite and b) the SASD- events composite.....**pág. 53**

**Fig. 13.** Neutral composites (October-December) of a) the intensity (shading) and direction (vectors) of the wind ( $m.s^{-1}$ ), b) the intensity (shading) and direction (vectors) of the Ekman transport ( $M_H$ , in  $m^2.s^{-1}$ ) and c) the Ekman pumping ( $W_{EK}$ ,  $m.day^{-1}$ ) for the southwestern African coast (SAC). The lower figures show the difference between the SASD+ and neutral composites of d) intensity (shading) and direction (vectors) of the wind speed ( $\Delta WSPD$ ,  $m.s^{-1}$ ), e) the intensity (shading) and direction (vectors) of Ekman transport ( $\Delta M_H$ ,  $m^2.s^{-1}$ ) and the f) Ekman pumping ( $\Delta W_{EK}$ ,  $m.day^{-1}$ ). The solid black lines in the lower figures indicate the regions with significant differences for the 80% confidence interval. In f) the dashed contour line show the position in c) where  $W_{EK} = 0$ .....**pág. 55**

**Fig. 14.** a) Neutral years composite (October-December) of the net heat flux (NHF, in  $W.m^{-2}$ ) and b) SASD+ anomalies composite of the NHF ( $\Delta NHF$ , in  $W.m^{-2}$ ) in the southwestern African coast (SAC). Positive values in a) indicate a NHF from the atmosphere to the ocean.....**pág. 57**

**Fig. 15.** a) Cape Frio (CFN) and b) St. Helena Bay (SHB) time series of the neutral composites of the chlorophyll-a (chl-a, green line, in  $mg.m^{-3}$ ), Ekman pumping ( $W_{EK}$ , blue line, in  $m.day^{-1}$ ) and stratification parameter  $\Phi$  calculated according to equation 5 of the text ( $\Phi$ , red line, in  $J.m^{-3}$ ). In c) and d) the time of the SASD+ anomalies composite of the same variables ( $\Delta chl-a$ ,  $\Delta W_{EK}$ ,  $\Delta \Phi$ ) as a) and b). The time series were smoothed with a 3-month moving average filter.....**pág. 58**

**Fig. 16.** Vertical section of a) the neutral years composite (December-February) and b) the SASD+ anomalies composite of the water column temperature ( $T$ , in  $^{\circ}\text{C}$ ) at Cape Frio (CFN). The dashed line show the  $16^{\circ}\text{C}$  isotherm ( $\text{SACW} < 16^{\circ}\text{C}$ ) of a) the neutral years composite and b) the SASD+ events composite.....**pág. 61**

**Fig. 17.** Vertical section of a) the neutral years composite (December-February) and b) the SASD+ anomalies composite of the water column temperature ( $T$ , in  $^{\circ}\text{C}$ ) at St. Helena Bay (SHB). The dashed line show the  $14^{\circ}\text{C}$  isotherm ( $\text{ESACW} < 14^{\circ}\text{C}$ ) of a) the neutral years composite and b) the SASD+ events composite.....**pág. 62**

**Fig. 18.** Neutral composites (October-December) of a) the intensity (shading) and direction (vectors) of the wind ( $\text{m}\cdot\text{s}^{-1}$ ), b) the intensity (shading) and direction (vectors) of the Ekman transport ( $M_H$ , in  $\text{m}^2\cdot\text{s}^{-1}$ ) and c) the Ekman pumping ( $W_{EK}$ ,  $\text{m}\cdot\text{day}^{-1}$ ) for the southwestern African coast (SAC). The lower figures show the difference between the SASD- and neutral composites of d) intensity (shading) and direction (vectors) of the wind speed ( $\Delta WSPD$ ,  $\text{m}\cdot\text{s}^{-1}$ ), e) the intensity (shading) and direction (vectors) of Ekman transport ( $\Delta M_H$ ,  $\text{m}^2\cdot\text{s}^{-1}$ ) and the f) Ekman pumping ( $\Delta W_{EK}$ ,  $\text{m}\cdot\text{day}^{-1}$ ). The solid black lines in the lower figures indicate the regions with significant differences for the 80% confidence interval. In f) the dashed contour line show the position in c) where  $W_{EK} = 0$ .....**pág. 63**

**Fig. 19.** a) Neutral years composite (October-December) of the net heat flux (NHF, in  $\text{W}\cdot\text{m}^{-2}$ ) and b) SASD- anomalies composite of the NHF ( $\Delta\text{NHF}$ , in  $\text{W}\cdot\text{m}^{-2}$ ) in the southwestern African coast (SAC). Positive values in a) indicate a NHF from the atmosphere to the ocean. The solid black lines indicate the regions with significant differences for the 80% confidence interval.....**pág. 65**

**Fig. 20.** a) Cape Frio (CFN) and b) St. Helena Bay (SHB) time series of the neutral composites of the chlorophyll-a (chl-a, green line, in  $\text{mg}\cdot\text{m}^{-3}$ ), Ekman pumping ( $W_{EK}$ , blue line, in  $\text{m}\cdot\text{day}^{-1}$ ) and stratification parameter  $\Phi$  calculated according to equation 5 of the text ( $\Phi$ , red line, in  $\text{J}\cdot\text{m}^{-3}$ ). In c) and d) the time of the SASD- anomalies composite of the same variables ( $\Delta\text{chl-a}$ ,  $\Delta W_{EK}$ ,  $\Delta\Phi$ ) as a) and b). The time series were smoothed with a 3-month moving average filter.....**pág. 66**

**Fig. 21.** Vertical section of a) the neutral years composite (December-February) and b) the SASD- anomalies composite of the water column temperature ( $T$ , in  $^{\circ}\text{C}$ ) at Cape Frio (CFN). The dashed line show the  $16^{\circ}\text{C}$  isotherm ( $\text{SACW} < 16^{\circ}\text{C}$ ) of a) the neutral years composite and b) the SASD- events composite.....**pág. 67**

**Fig. 22.** Vertical section of a) the neutral years composite (December-February) and b) the SASD- anomalies composite of the water column temperature ( $T$ , in  $^{\circ}\text{C}$ ) at St. Helena Bay (SHB). The dashed line show the  $14^{\circ}\text{C}$  isotherm ( $\text{ESACW} < 14^{\circ}\text{C}$ ) of a) the neutral years composite and b) the SASD- events composite.....**pág. 68**

# Lista de Acrônimos e Abreviações

## A

**ACAS** – Água Central do Atlântico Sul

**ASAS** – Alta Subtropical do Atlântico Sul

## B

**BC** – Brazil Current

**BUS** – Benguela Upwelling System

## C

**CB** – Corrente do Brasil

**CFB** – Cabo Frio/Brazil

**CFN** – Cape Frio/Namibia

**Chla-a** – Chlorophyll-a concentration

**CMEMS** – Copernicus Marine Environment Monitoring Service

**CSA** – Costa Sudoeste Africana

**CSB** – Costa Sudeste-Sul do Brasil

**CSM** – Cabo Santa Marta/Brazil

## D

**DSAS** – Dipolo Subtropical do Atlântico Sul

**DSAS+** – Fase positiva do Dipolo Subtropical do Atlântico Sul

**DSAS-** – Fase negativa do Dipolo Subtropical do Atlântico Sul

## E

**ECMWF** – European Centre for Medium-Range Weather Forecasts

**ERA-Interim**

**ESACW** – East South Atlantic Central Water

## F

**f** – Parâmetro de Coriolis (Coriolis Parameter)

**FCL** – Fluxo de Calor Latente

**FCS** – Fluxo de Calor Sensível

## G

**g** – Aceleração da Gravidade (Gravitational Acceleration)

**GLO** – GLORYS12v1

## I

**IDSAS** – Índice do Dipolo Subtropical do Atlântico Sul

## L

**LHF** – Latent Heat Flux

**LWR** – Long-Wave Radiation

## N

**NHF** – Net Heat Flux

## M

**M<sub>x</sub>** – Transporte Zonal de Ekman  
(Zonal Ekman Transport)

**M<sub>y</sub>** – Transporte Meridional de  
Ekman (Meridional Ekman  
Transport)

## O

**OAS** – oceano Atlântico Sul

**OC-CCI** – Ocean Color – Climate  
Change Initiative

## P

**PNM** – Pressão ao Nível do Mar

## Q

**Q<sub>NET</sub>** – Fluxo Líquido de Calor

## R

**ROC** – Radiação de Onda Curta

**ROL** – Radiação de Onda Longa

## S

**SACW** – South Atlantic Central  
Water

**SAO** - South Atlantic ocean

**SASD** – South Atlantic Subtropical  
Dipole

**SASD+** – Positive South Atlantic  
Subtropical Dipole

**SASD-** – Negative South Atlantic  
Subtropical Dipole

**SASDI** – South Atlantic Subtropical  
Index

**SHB** – St. Helena Bay/South Africa

**SHF** – Sensible Heat Flux

**SRB** – Sistema de Ressurgência de  
Benguela

**SST** – Sea Surface Temperature

**SWR** – Short-Wave Radiation

## T

**TSM** – Temperatura da Superfície do  
Mar

## W

**W<sub>EK</sub>** – Bombeamento de Ekman  
(Ekman Pumping)

# Resumo

A interação entre modos de variabilidade climática e a dinâmica de sistemas de ressurgência costeira vem sendo extensivamente estudada globalmente. Sabe-se que o modo climático conhecido como Dipolo Subtropical do Atlântico Sul (SASD) atua sobre o oceano Atlântico Sul modificando os campos de ventos próximos à superfície do oceano. Neste oceano encontram-se importantes sistemas de ressurgência costeira, tais como o Sistema de Ressurgência de Benguela (BUS), associado à corrente de Benguela na costa sudoeste do continente africano (SAC), e os sistemas de ressurgência de Cabo Frio e Cabo Santa Marta na costa sudeste-sul do Brasil (SBC). No sistema de Cabo Frio na SBC, os ventos de nordeste (favoráveis ao processo de ressurgência costeira) são intensificados em ambas as fases positiva e negativa do SASD, o que potencializa o bombeamento de Ekman e resulta em anomalias positivas na concentração superficial de clorofila-a. Na região do Cabo Santa Marta há uma intensificação do bombeamento de Ekman durante os eventos positivos do SASD. Contudo, em Cabo Santa Marta a resposta da concentração de clorofila-a às modificações da interação oceano-atmosfera não é direta, indicando ação de outros processos não abordados neste estudo, como o deságue de grandes rios e a proximidade com a Confluência Brasil-Malvinas. Na SAC a resposta para a fase positiva do SASD é dependente da latitude. Na porção norte do BUS (norte de 27°S) o bombeamento de Ekman é intensificado devido ao incremento na velocidade dos ventos alísios de sudeste. Entretanto, esse incremento na velocidade do vento também intensifica a mistura turbulenta na coluna de água, o que faz com que o aumento na concentração de clorofila-a tenha um certo atraso em relação ao bombeamento de Ekman. Ao sul de 27°S, a fase positiva do SASD resulta em um enfraquecimento na dinâmica de ressurgência, com conseqüente enfraquecimento no transporte de Ekman no sentido *offshore*. Durante a fase negativa do SASD na região da SAC destaca-se a interação entre a porção sul do BUS e os anéis das Agulhas. As anomalias negativas no fluxo líquido de calor na região indicam uma possível maior liberação de vórtices durante esse período. Este aumento na

liberação dos vórtices das Agulhas pode estar relacionada com a migração dos ventos de oeste para sul durante os eventos de SASD negativos, o que desloca a posição do rotacional nulo do estresse do vento sobre a superfície do mar em direção ao polo Sul. Entretanto, esta interação SASD-Agulhas carece de maiores estudos.



# Abstract

It is known that the climatic mode known as the South Atlantic Subtropical Dipole (SASD) acts on the South Atlantic Ocean by modifying wind fields close to the ocean's surface. There are important coastal upwelling systems in this ocean, such as the Benguela Upwelling System (BUS), associated with the Benguela current in the southwest African coast (SAC), and the Cabo Frio and Cabo Santa Marta upwelling systems in the southeast-south Brazilian coast (SBC). In the Cabo Frio system at SBC the northeast winds (upwelling favorable) are intensified in both the positive and negative SASD phases, which enhances the Ekman pumping and results in positive anomalies in the surface chlorophyll-a concentration. In the Cabo Santa Marta region there is an intensification of Ekman pumping during the positive events of the SASD. However, in Cabo Santa Marta the response of chlorophyll-a concentration to changes in the ocean-atmosphere interaction is not direct, which indicates the action of other processes not addressed in this study, such as the large rivers discharge and the proximity to the Brazil-Malvinas confluence. The SAC response to the SASD positive phase is latitude dependent. In the northern portion of the BUS (north of 27°S) the Ekman pumping is intensified due to the increase in the speed of the southeast trade winds. On the other hand, this increase in wind speed also intensifies the turbulent mixing in the water column, which means that the increase in chlorophyll-a concentration has a certain delay in relation to Ekman pumping anomalies. South of 27°S the positive phase of the SASD results in a weakening in the offshore Ekman transport and consequent decrease of coastal upwelling dynamics. During the negative phase of the SASD in the SAC region, the interaction between the southern portion of the BUS and the Agulhas rings stands out. Negative anomalies in the net heat flux at this region indicate a likelihood greater release of rings during this period. This increase in the release of the Agulhas rings may be related to the westerlies poleward displacement during negative SASD events, which dislocate the zero wind stress curl position towards the Pole. This SASD-Agulhas interaction still needs further studies.

# Capítulo I: Introdução

## 1.1 Ressurgência costeira

O processo de ressurgência costeira está entre os principais processos associados à produtividade primária em regiões de plataforma continental. São processos que envolvem o transporte vertical de águas de subsuperfície (mais frias e ricas em nutrientes) para a região fotossinteticamente ativa, vinculado ao transporte horizontal de Ekman no sentido *offshore* o qual é, por sua vez, associado à direção dos ventos sobre a superfície dos oceanos (Fig. 1) [e.g. Ekman 1905, Carr 2001, Mann & Lazier 2005].

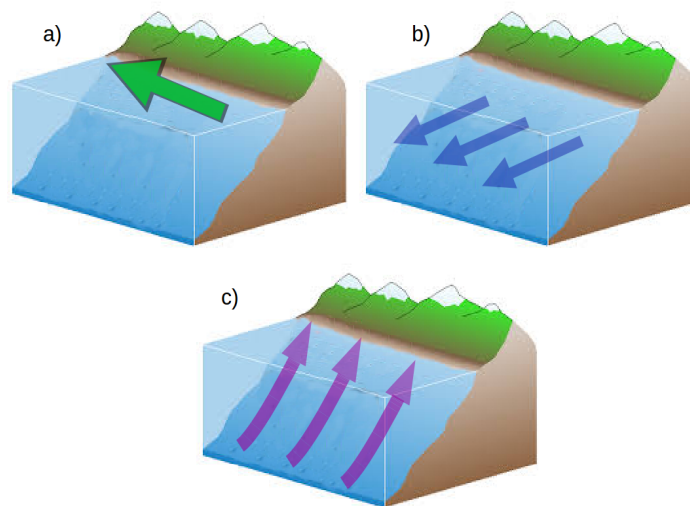


**Figura 1:** Esquema simplificado da interação entre o vento e os oceanos, para o hemisfério Sul. Inicialmente, a) o vento sopra paralelo a direção da costa (vetor verde), b) ocasionando o transporte integrado horizontal de Ekman à esquerda da direção do vento (vetor azul), o que resulta em c) advecção vertical positiva (em direção a superfície) de águas de subsuperfície (vetor lilás).

Esse deslocamento da camada superficial dos oceanos (da superfície até a profundidade da camada de Ekman), quando ocorre no hemisfério Sul (Norte), se dá em ângulo reto à esquerda (direita) da direção do vento atuante. Essa remoção de águas no sentido *offshore*, quando ocorre ao longo de barreiras físicas (e.g. nas bordas de continentes), é então compensada pela ascensão

de águas de subsuperfície. Foi Walfrid Ekman [Ekman 1905], no início do século XX, quem demonstrou como era o transporte integrado, da superfície do mar até a chamada profundidade da camada de Ekman, resultante da interação entre a tensão de cisalhamento do vento na superfície dos oceanos e a rotação da Terra.

A partir da noção do funcionamento da interação entre os ventos e as camadas superficiais dos oceanos, podemos então deduzir as velocidades verticais da água com base no rotacional da tensão de cisalhamento do vento na superfície do mar. Este rotacional está diretamente conectado, através da divergência e convergência do transporte de águas superficiais, com os processos de ressurgência e subsidência nos oceanos, respectivamente (Fig. 2). Deste modo, no hemisfério Sul (HS), quando o vento possui uma rotação ciclônica ou quando o transporte horizontal de Ekman por ele gerado (em regiões costeiras) resulta em um transporte *offshore*, a divergência do transporte de águas superficiais é refletida em valores negativos do rotacional da tensão de cisalhamento do vento na superfície do mar, indicando então uma condição favorável à ressurgência. Essa condição resulta em uma velocidade vertical positiva (ressurgência) induzida pelo vento, o chamado Bombeamento de Ekman. Situação oposta ocorre quando o vento possui uma rotação anticiclônica ou quando o transporte horizontal de Ekman associado é na direção da região costeira, o que é refletido em um cenário de convergência e numa velocidade vertical negativa (subsidência).

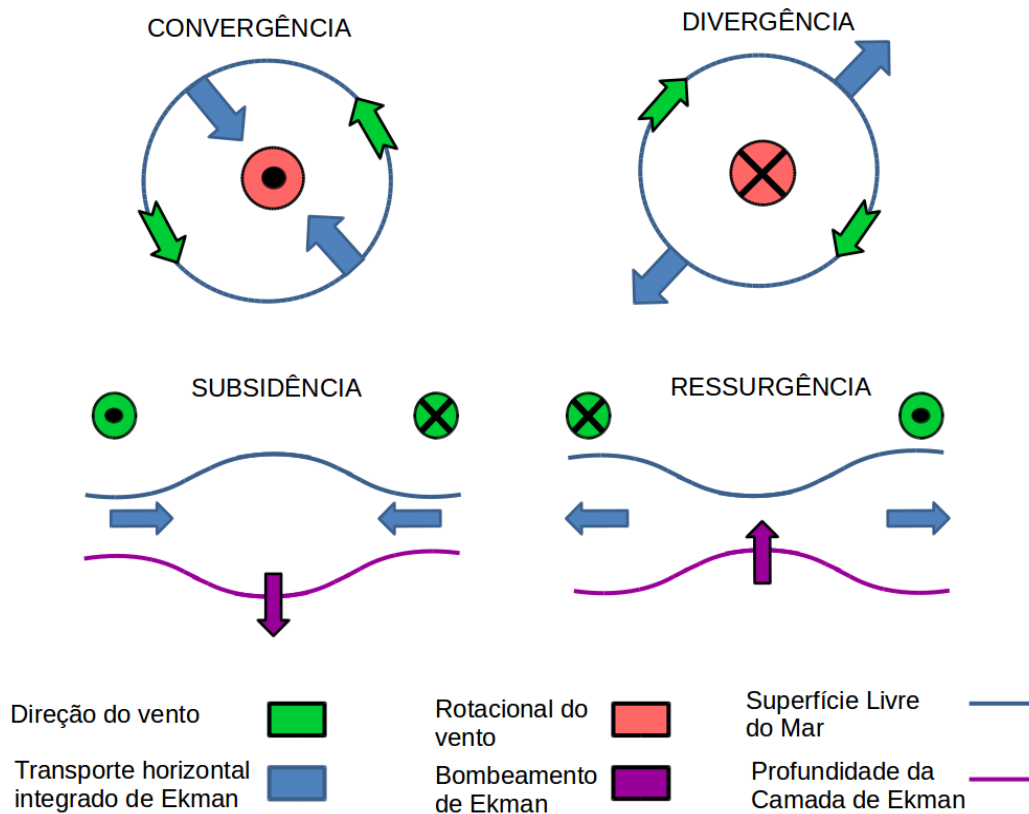


**Figura 2:** Esquemática, para o hemisfério Sul, da dinâmica de subsidência e ressurgência associadas ao rotacional da tensão de cisalhamento do vento. a-c) o rotacional do vento será positivo, indicando convergência, quando o vento possuir uma tendência de rotação anti-horária, resultando em velocidades verticais negativas da água na base da camada de Ekman. b-d) o rotacional do vento será negativo, indicando divergência, quando o vento possuir uma tendência de rotação horária, resultando em velocidades verticais positivas da água na base da camada de Ekman.

## 1.2 Ressurgência Costeira no Oceano Atlântico Sul

Para iniciar este tópico apresentaremos uma breve descrição da circulação geral superficial do oceano Atlântico Sul (OAS), detalhadamente documentada em trabalhos pretéritos [Peterson & Stramma 1991, Stramma & England 1999, Tomczak & Godfrey 2003, Talley *et al.* 2011]. Na figura 3, podemos visualizar as principais feições presentes nesta bacia oceânica.

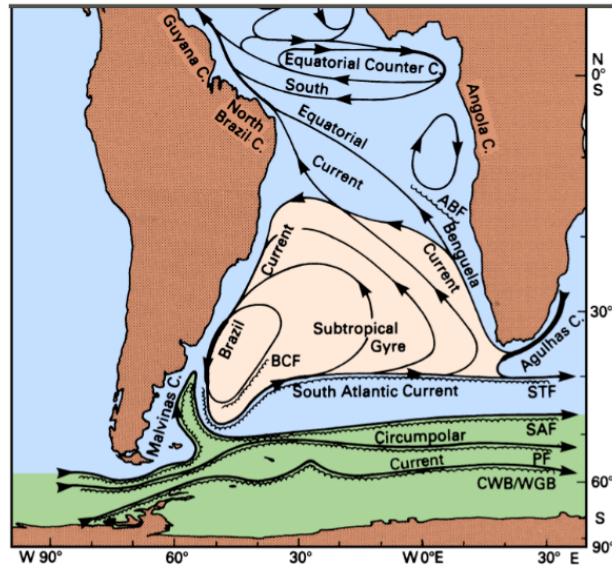


**Figura 3:** Circulação superficial do oceano Atlântico Sul. Vetores representam as direções das principais correntes. O sistema do grande Giro subtropical é representado pela coloração rosa claro, em verde é representado o sistema da Corrente Circumpolar Antártica. Abreviações: Frente Angola-Benguela (ABF), Frente Brasil-Malvinas (BCF), Frente Subtropical (STF), Frente Subantártica (SAF), Frente Polar (PF). Retirado de Tomczack & Godfrey [2003].

A circulação superficial (0 ~ 1000 m) do OAS é caracterizada pela presença de um grande giro subtropical anticiclônico induzido pelo vento. A borda leste do OAS é contornada pela Corrente de Benguela, caracterizada por ser mais larga, pouco profunda e de águas frias. Esta corrente inicia nas proximidades do limite sul do continente africano e segue para noroeste, quando adentra o sistema de correntes equatoriais, se integrando ao ramo sul do sistema, dando origem a Corrente Sul Equatorial, a qual segue seu percurso numa direção praticamente zonal de Leste para Oeste. Quando esta corrente encontra a barreira continental da costa do Brasil, aproximadamente em torno de 10°S, ela bifurca dando origem à Corrente Norte do Brasil, a qual sai do sistema do OAS e se desloca para o hemisfério Norte, e à Corrente do Brasil, o ramo da bifurcação que é mantido dentro do OAS e que se dirige para sul.

A corrente do Brasil (CB) é conhecida por ser uma corrente de contorno oeste, o que faz com que tenha características muito bem marcadas:

relativamente mais estreita, mais profunda, mais quente e mais intensa. Contornando a costa do Brasil, a CB se desloca para Sul até aproximadamente a latitude de 40°S onde, nas proximidades da frente subtropical, se desprende da costa e assume um deslocamento praticamente zonal de Oeste para Leste, na forma da Corrente do Atlântico Sul. Esta, por sua vez, segue o seu trajeto até o limite sul do continente africano (~35°S), onde fecha o sistema do giro subtropical do Atlântico Sul, se integrando ao início da Corrente de Benguela.

Outras interações do sistema de correntes superficiais do OAS devem ser destacadas. Na borda leste do giro, no limite sul do continente africano, ocorre uma interação entre as águas do OAS e as do oceano Índico através dos Anéis das Agulhas [e.g. Garzoli *et al.* 1999, Beal 2009, Biastoch *et al.* 2015]. Esses anéis são vórtices liberados para dentro do OAS pelo processo de retroflexão da Corrente das Agulhas, corrente de borda oeste do oceano Índico. Ainda na borda leste do OAS encontra-se uma interação que está associada ao Giro de Angola, um giro ciclônico, centrado em aproximadamente 10°S, responsável por levar águas quentes para a região costeira contornada pela Corrente de Benguela através da frente Angola-Benguela [Hutchings *et al.* 2009, Bachèlery *et al.* 2016, Tchupalanga *et al.* 2018]. Importante também é a confluência Brasil-Malvinas [Garzoli 1993, Garzoli & Garraffo 1989]. Esta região, na borda Oeste do OAS, é caracterizada pelo encontro da Corrente do Brasil, trazendo águas quentes vindas de regiões intertropicais, com a Corrente das Malvinas, que traz águas frias vindas de médias latitudes. A região da confluência Brasil-Malvinas é caracterizada ainda pela liberação de vórtices de mesoescala.

Para além da dinâmica já descrita, o OAS possui regiões com importantes sistemas de ressurgência costeira associados. No Sistema de Ressurgência de Benguela (SRB), localizado na costa sudoeste do continente Africano, os padrões de vento são principalmente forçados pelo gradiente de pressão entre o anticiclone semipermanente do Atlântico Sul, sistema denominado de Alta Subtropical do Atlântico Sul (ASAS), e o sistema de baixa pressão localizado sobre parte do continente Africano. Essa configuração da atmosfera (Fig. 4), associada ao ambiente continental árido do sudoeste do continente Africano, induz os ventos alísios de sudeste, os quais assumem um deslocamento paralelo à linha de costa da Namíbia e da costa oeste da África do Sul, contribuindo para que a região possua uma dinâmica favorável à ocorrência de processos de ressurgência [Nelson & Hutchings 1983, Shannon & Nelson 1996, Mackas *et al.* 2006, Hutchings *et al.* 2009].

**Figura 4:** Padrão climatológico da a) pressão ao nível do mar (PNM, hPa), mostrada na forma de isóbaras e b) da intensidade ( $m.s^{-1}$ ) e direção dos ventos para o período de 1993 a 2018 sobre o oceano Atlântico Sul. Médias climatológicas calculadas utilizando dados de reanálise ERA-Interim.

Adicionalmente ao sistema atmosférico previamente descrito, Nelson & Hutchings [1983] descrevem formações de células de baixas pressões associadas às ondulações observadas no cinturão dos ventos de oeste. Estas células são caracteristicamente aprisionadas à costa e atuam em escala



sinótica, enfraquecendo os ventos de sudeste durante suas passagens, alterando a sazonalidade da porção Sul do SRB (sul de 27°S). Levando em conta a dinâmica de Ekman, o sistema atmosférico e a orientação da linha de costa do SRB, Bakun & Nelson [1991], Fennel [1999] e Tim *et al.* [2015] demonstram que os processos de ressurgência na região são majoritariamente forçados pelo rotacional da tensão de cisalhamento dos ventos de sudeste, o que resulta em divergência de águas superficiais nas proximidades da costa e, conseqüentemente, em uma ressurgência costeira.

Assim como na borda leste, o oceano Atlântico Sul também possui sistemas de ressurgência em sua borda oeste. Cabo Frio (CFB) e Cabo de Santa. Marta (CSM), localizados na costa sudeste-sul do Brasil (CSB), são os principais sistemas de ressurgência da região [Campos *et al.* 1995, 2013, Guimaraens & Coutinho, 2000, Castelao *et al.* 2004, Möller *et al.* 2008, Mazzini & Barth, 2013]. O padrão dos ventos nesses locais e, conseqüentemente, a ressurgência na CSB têm importante relação com a sazonalidade do posicionamento da ASAS, de modo que os ventos de nordeste são considerados como favoráveis a processos de ressurgência costeira na região. O contexto atmosférico favorável pode ser observado durante a primavera/verão, quando a direção dos ventos de nordeste é paralela à costa nas regiões do Cabo Frio e do Cabo de Santa Marta. Durante esse período, esses dois sistemas da costa do Brasil estão sob as melhores condições para que ocorram processos de ressurgência. Estas condições são evidenciadas pelo rotacional da tensão de cisalhamento do vento, o qual é negativo no entorno dos dois locais, indicando favorecimento de velocidades verticais positivas induzidas pelo vento [Castelao & Barth 2006, Mazzini & Barth 2013].

Adicionalmente, Möller *et al.* [2008] e Campos *et al.* [2013] mostram como a passagem de sistemas ciclônicos móveis, com deslocamento para nordeste, podem alterar a direção e a intensidade dos ventos na região do CSM, resultando em convergência sobre a plataforma continental, desfavorecendo o processo de ressurgência.

Como já citado anteriormente, o regime de ventos é resultado do padrão atmosférico característico da ASAS. Essa, por sua vez, varia em intensidade e posição do seu centro em distintas escalas de espaço e tempo, além da comunidade científica já possuir evidências da intensificação desse sistema, como um todo, nas últimas décadas [Vizy & Cook 2016, Sun *et al.* 2017, Marcello *et al.* 2018]. Deste modo, padrões espaço-temporais das direções e intensidades dos ventos sobre o oceano Atlântico Sul e, conseqüentemente, da dinâmica de ressurgência costeira, são modulados por processos de interação oceano-atmosfera com variadas escalas de espaço e tempo. Além dos trabalhos posteriormente citados, muitos outros buscaram descrever as respostas oceânicas ligadas à variabilidade dos ventos sobre o Atlântico Sul.

Para a borda leste do oceano, Cury & Shannon [2004] e Hutchings *et al.* [2009] descreveram importantes mudanças na estrutura ecossistêmica na região do SRB, as quais estão fisicamente conectadas às mudanças nos regimes local e global de ventos. Peard [2007] utilizou dados *in situ* para estudar a variabilidade temporal dos regimes de vento e da dinâmica de ressurgência na costa da Namíbia, descrevendo um comportamento oscilatório desde a escala de tempo diária até interanual. Com isso, o autor mostra o período de primavera/verão como o mais favorável ao processo de ressurgência, além de discutir sobre a relação entre o enfraquecimento dos

ventos, eventos de aquecimento anômalo da região e a intrusão de águas pobres em oxigênio originadas ao norte da região [Roux & Shannon 2004]. Esse padrão de variabilidade é também observado em trabalhos anteriores [Nelson & Hutchings 1983, Bakun & Nelson, 1991, Shannon & Nelson 1996] e posteriores [Hutchings *et al.* 2009, Chen *et al.* 2012, Lamont *et al.* 2017], quando o assunto é o compartimento norte do SRB (Norte de 27°S). Já para o compartimento sul da SRB (Sul de 27°S), a interação com o cinturão de ventos de oeste conduz a periodicidades um pouco defasadas em relação ao compartimento norte, de modo que é possível observar, durante os meses de inverno austral, a inversão do rotacional da tensão de cisalhamento do vento [Andrews & Hutchings 1980, Bakun & Nelson 1991, Hutchings *et al.* 2009]. A variabilidade do regime de ventos sobre o Atlântico Sul não é exclusividade da borda leste do oceano. Entretanto, há um número maior de publicações associadas ao SRB do que à região da CSB. Campos *et al.* [2013] exploraram o uso da modelagem numérica para compreender com mais detalhes a dinâmica de ressurgência do extremo sul do Brasil, região no entorno do CSM, destacando sua importante associação com o regime sazonal de ventos. Mahiques *et al.* [2005] estudaram a dinâmica de ressurgência na região do CF com base em análise sedimentológica de testemunhos. Neste estudo mostram que, nos últimos 700 anos, os valores de temperatura da superfície do mar (TSM) assumem uma tendência de queda, indicando que a intensificação do sistema da ASAS e, conseqüentemente, dos ventos de NE, resultaram na intensificação do sistema de ressurgência costeira local.

### **1.3. O Dipolo Subtropical do Atlântico Sul**

De modo a complementar as informações sobre os sistemas de ressurgência costeira do OAS, o foco deste trabalho é identificar como o Dipolo Subtropical do Atlântico Sul [Venegas *et al.*, 1996, 1997, Palastanga *et al.* 2002, Fauchereau *et al.* 2003, Sterl & Hazeleger, 2003, Haarsma *et al.* 2005] pode modificar os sistemas de ressurgência costeira associados à CSB e à CSA. O Dipolo Subtropical do Atlântico Sul (DSAS) é caracterizado como um modo de variabilidade climática, ou seja, é a oscilação de determinadas propriedades com certa periodicidade interanual e amplitude variável, sendo caracterizado por anomalias no campo de pressão ao nível do mar (PNM) na região da ASAS e por um gradiente nordeste/sudoeste na distribuição espacial das anomalias de TSM [Venegas *et al.* 1996, 1997, Palastanga *et al.* 2002, Haarsma *et al.* 2005]. Essas anomalias de TSM estão associadas com oscilações atmosféricas na pressão ao nível do mar, as quais modificam a intensidade dos ventos alísios de sudeste e, conseqüentemente, o fluxo de calor latente entre o oceano e a atmosfera [Fauchereau *et al.* 2003, Haarsma *et al.* 2003, Sterl & Hazeleger, 2003].

O processo de desenvolvimento e decaimento do DSAS foi descrito por Morioka *et al.* [2011]. O esquema da figura 5, retirada de Morioka *et al.* [2011], traz a seqüência de processos desde as primeiras alterações no campo de PNM até as anomalias de TSM resultantes. A caracterização de um evento positivo ou negativo, é proposto por Morioka *et al.* [2011] através do Índice do Dipolo Subtropical do Atlântico Sul (IDSAS). Para computar o IDSAS, o autor leva em consideração duas regiões do OAS, as quais são denominadas de polo sudoeste (30°S – 40°S; 10°W – 30°W) e polo nordeste (15°S – 25°S; 0° –

20°W). Com isso, o IDSAS é computado através da diferença da média espacial das anomalias de temperatura da superfície do mar entre o polo sudoeste e polo nordeste, para todo o intervalo dos meses de dezembro, janeiro, fevereiro e março. Serão então considerados anos em que a região está sob um evento de DSAS positivo aqueles em que o valor do IDSAS, segundo Morioka *et al.* [2011], for maior ou igual ao valor de 0,8 °C, enquanto que, serão considerados eventos de DSAS negativos, os anos em que a diferença for menor ou igual a -0,8 °C.

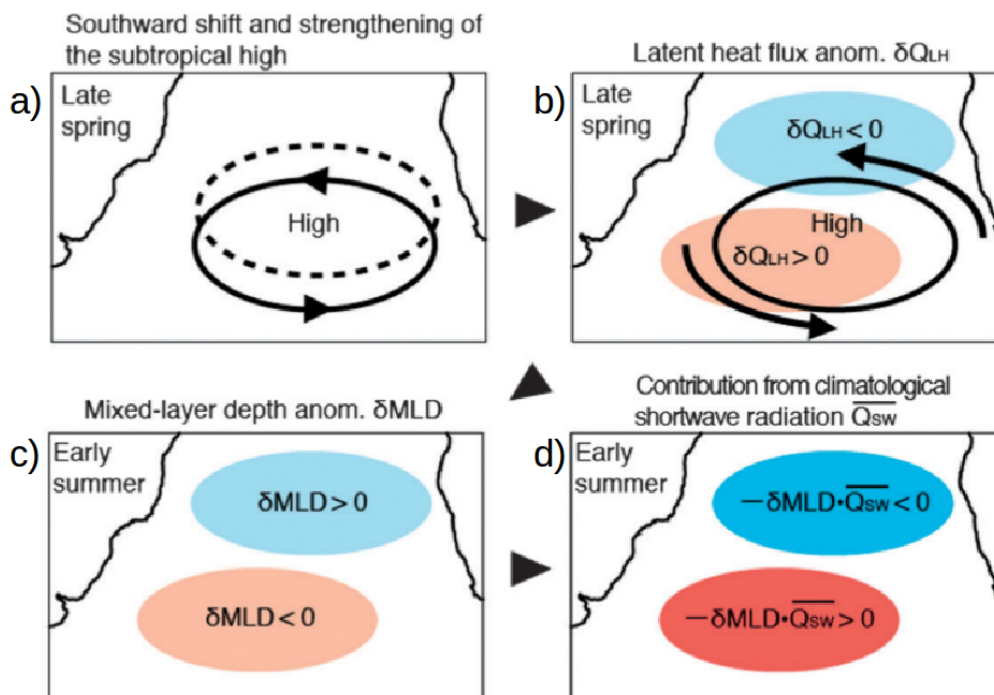


**Figura 5:** Representação do desenvolvimento da fase positiva do DSAS. a) O processo se inicia com a intensificação da ASAS e deslocamento desta para sul, modificando o sistema de vento, b) o que resulta em anomalias no fluxo de calor latente para a atmosfera ( $\delta Q_{LH}$ ). c) Este último, por sua vez, altera a profundidade da camada de mistura ( $\delta MLD$ ), d) contribuindo para o enfraquecimento (intensificação) da contribuição da radiação solar ( $Q_{sw}$ ). Retirado de Morioka *et al.* [2011].

Durante o processo de formação da fase positiva do DSAS (DSAS+), podemos observar um aumento anômalo na PNM na região do anticiclone semipermanente do Atlântico Sul (Fig. 5a). Esse centro de alta pressão atmosférica sobre o oceano Atlântico Sul é o que origina os ventos alísios de

sudeste. Com o aumento da intensidade deste centro, a velocidade dos alísios também aumenta, contribuindo para um fluxo de calor latente anômalo (Fig. 5b) em direção à atmosfera na região do polo nordeste. Estas anomalias do fluxo de calor acarretam o aumento da profundidade da camada de mistura (Fig. 5c) que, por sua vez, reduz a capacidade de aquecimento das radiações de onda curta (Fig. 5d). O oposto é observado na região do polo sudoeste, deste modo, originando a configuração com anomalias de TSM negativas no polo nordeste e positivas no polo sudoeste. Todo esse processo se inverte durante as fases negativas do DSAS (DSAS-). Durante este período há, então, um enfraquecimento anômalo da PNM, ocasionando um enfraquecimento da intensidade dos ventos alísios no polo nordeste, seguido da consequente redução do fluxo de calor latente para a atmosfera. Com isso, a profundidade da camada de mistura no polo nordeste fica mais rasa, intensificando a capacidade de aquecimento da radiação de onda curta. O inverso ocorre no polo sudoeste. Durante a fase negativa, esses processos resultam em anomalias positivas da TSM no polo nordeste e negativas no polo sudoeste.

Como consequência desses processos, o DSAS vem sendo associado a modificações no regime de pluviosidade em algumas regiões da América do Sul, de modo que a fase negativa do DSAS, a qual esta associada à redução na intensidade dos ventos alísios e à anomalia positiva na TSM no polo nordeste, é colocada como sendo responsável por anomalias positivas nas taxas de pluviosidade no Nordeste do Brasil e em regiões do centro-sul do continente Africano [Reason 1998, Pezzi & Cavalcanti 2001, Haarsma *et al.* 2003, Wainer *et al.* 2014]. Com relação às interconexões, característica de modos de variabilidade climática, Rodrigues *et al.* [2015] utilizaram a

modelagem numérica com o objetivo de explicar o que seria o “gatilho” para os processos que resultariam na formação do DSAS. Os autores o associam às anomalias da altura geopotencial em determinados níveis atmosféricos, apontando ligação entre anos de El-Niño (La-Niña) no Pacífico central e eventos de DSAS- (DSAS+) no SAO. Essa ligação se dá por ondas de Rossby, as quais que se deslocam do oceano Pacífico ao oceano Atlântico Sul, através da região do extremo sul da América Sul.

### 1.3. Áreas de estudo

Levando em conta as modificações atmosféricas e oceânicas relacionadas ao DSAS, podemos considerar que a dinâmica do Atlântico Sul, principalmente os sistemas de ressurgência costeira associados às bordas oceânicas, deve sofrer alguma alteração sob a influência deste modo climático. Com isso, as áreas de estudo do presente trabalho englobam os três distintos sistemas de ressurgência costeira no oceano Atlântico Sul supracitados (Fig. 6).

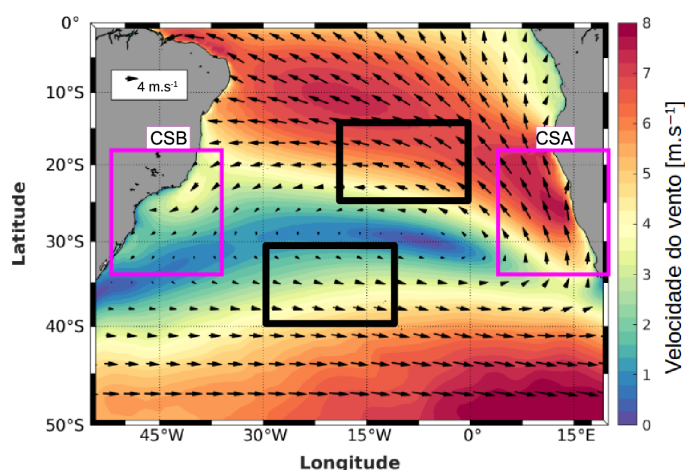


**Figura 6:** Padrão climatológico da intensidade (cores de fundo) e direção dos ventos (vetores) sobre o oceano Atlântico Sul para o período de 1993-2018. Os retângulos em magenta indicam as áreas de estudo da costa sudeste-sul do Brasil (CSB) e da costa sudoeste africana (CSA). As caixas em preto contornam as áreas do polo nordeste (15°S – 25°S e 0°W – 20°W) e do polo sudoeste (30°S – 40°S e 10°W – 30°W) das quais foram calculadas as médias espaciais das anomalias da temperatura da superfície do mar (TSM) aplicadas no cálculo do índice do Dipolo Subtropical do Atlântico Sul (IDSAS).



As figuras 7a e 7b apresentam uma visão aproximada das áreas de estudo. Na borda oeste do OAS (Fig. 7a), a região é delimitada pelas coordenadas 18°S – 34°S e 52°W – 36°W, cobrindo a região da costa sudeste-sul do Brasil (CSB), tendo os sistemas de ressurgência costeira de Cabo Frio (CFB) e Cabo Santa Marta (CSM) associados. Na borda leste do OAS (Fig. 7b), a área de estudo é delimitada pelas coordenadas 18°S – 34°S e 4°E – 20°E, abrangendo a costa da Namíbia e a costa sudoeste da África do Sul, região associada ao Sistema de Ressurgência de Benguela. Neste trabalho iremos nos referir a essa região como Costa Sudoeste Africana (CSA).

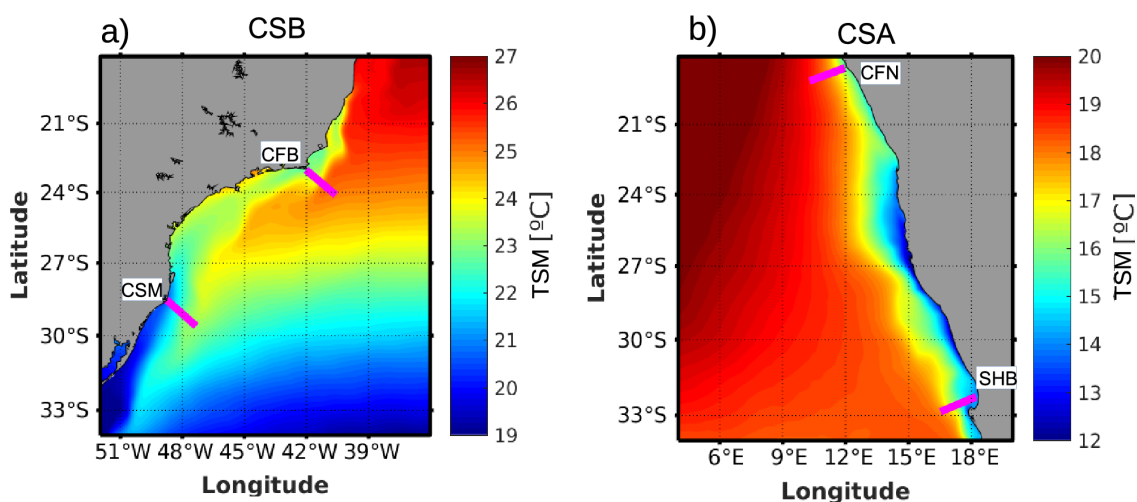


**Figura 7:** Em a) e b) padrão climatológico da TSM das regiões demarcadas pelos retângulos em magenta da CSB e da CSA na figura 6, respectivamente. Os traços em magenta indicam as seções utilizadas neste estudo para Cabo Frio (CFB) e Cabo Santa Marta (CSM) na CSB e Cape Frio (CFN) e Santa Helena Bay (SHB) na CSA. As climatologias foram calculadas utilizando os produtos de TSM ESA-CCI.

Em virtude da importância social, ecológica e econômica dos processos de ressurgência costeira do Atlântico Sul, o presente estudo busca compreender de que maneira o sistema atmosférico associado ao DSAS, seja em sua fase positiva ou negativa, interage com a dinâmica de ressurgência na costa sul/sudeste do Brasil e nas costas oeste da Namíbia e sudoeste da África do Sul. A presente dissertação será apresentada em formato de artigo. Após

essa introdução, apresentamos os objetivos os quais buscamos alcançar durante a construção deste estudo, a metodologia aplicada e, na sequência, o artigo científico submetido originado desta dissertação. O documento então é finalizado com uma síntese das discussões e conclusões apresentadas no artigo.

## **Capítulo II: Objetivos**

O presente estudo visa descrever a interação entre os padrões de variabilidade do Dipolo Subtropical do Atlântico Sul e os processos de ressurgência nas áreas de estudo descritas anteriormente. Para isso, neste capítulo, serão apresentados os objetivos os quais buscamos alcançar para a descrição dessas interações.

### **2.1: Objetivo Geral**

Descrever a variabilidade espaço-temporal dos processos de ressurgência, em regiões costeiras do oceano Atlântico Sul, durante a ocorrência de eventos associados com o modo de variabilidade Dipolo Subtropical do Atlântico Sul

### **2.2: Objetivos Específicos**

- Obter a variabilidade espacial das anomalias de direção e intensidade dos ventos e do fluxo líquido de calor entre o oceano e a atmosfera, sobre a região do oceano Atlântico Sul;
- Identificar e quantificar padrões de alterações na estratificação local e nos transportes de Ekman horizontal e vertical, para a costa sudeste-sul do Brasil e costa sudoeste da África;
- Verificar modificações na concentração superficial de clorofila, na região da costa sudeste-sul do Brasil e costa sudoeste da África, durante os anos de ocorrência do DSAS.

## **Capítulo III: Materiais e Métodos**

Neste capítulo serão apresentados os produtos utilizados e os processos realizados para que fosse possível atingir os objetivos deste estudo. No subtópico 3.1, apresentamos quais os produtos atmosféricos e oceânicos utilizados, bem como sua fonte e resoluções espaço-temporais. Para o subtópico 3.2, trazemos as informações de como esses produtos foram trabalhados, desde a metodologia aplicada para computar os IDSAS, passando pela dinâmica de Ekman, construção das composições e, por fim, o estudo da evolução temporal das anomalias de clorofila-a durante os períodos de DSAS.

### **3.1: Produtos Utilizados**

Produtos de reanálises são construídos a partir de dados obtidos de diversas fontes (satélites, boias, navios, estações em terra e etc.), buscando cobrir espacialmente todo o planeta e uma larga janela temporal. Com isso, são importantes ferramentas para o estudo de interações oceano-atmosfera ligadas a modos de variabilidade climática. O presente capítulo visa trazer as informações sobre os produtos de reanálises atmosféricas (3.1.1) e oceânicas (3.1.2) utilizados neste estudo, bem como os dados de clorofila-a obtidos por satélites.

#### **3.1.1: Reanálises Atmosféricas**

Os produtos de reanálises atmosféricas (Tab. 1) utilizados neste trabalho foram obtidos através do portal do European Centre for Medium-Range Weather Forecast (<https://www.ecmwf.int/>, ECMWF). Os produtos escolhidos foram os dados de reanálises ERA-Interim (ERA-I), os quais compreendem o período de 1979 até 2018, com uma resolução temporal mensal. Para este trabalho, utilizamos a janela de 1993 a 2018 das reanálises com resolução

espacial de 0,125°, de modo a manter a janela de tempo dos produtos de reanálises oceânicas.

### 3.1.2: Reanálises Oceânicas

Para representar as condições oceânicas, fez-se uso de produtos de reanálise oceânica global, GLORYS12v1 (GLO), do Copernicus Marine Environment Monitoring Service (CMEMS), o qual tem como forçantes atmosféricas os produtos de reanálises ERAI. Os produtos GLO possuem assimilação de dados de perfis de temperatura e salinidade *in situ*, superfície livre do mar e temperatura da superfície do mar. Esta é a primeira versão do produto com resolução espacial de 12 km e 50 níveis de profundidade, a qual possui produtos diários e mensais, cobrindo o período de 1993 a 2018. Para esse trabalho, fez-se uso da resolução temporal mensal de todo o período disponível. As variáveis utilizadas estão expressas na tabela 1.

**Tabela 1:** Síntese das informações dos produtos de reanálises atmosféricas e oceânicas utilizados neste estudo. As variáveis utilizadas foram a temperatura da superfície do mar (TSM), componentes horizontais da velocidade do vento a 10 m (u e v), fluxo líquido de calor latente (FCL), fluxo líquido de calor sensível (FCS), radiação de onda curta (ROC), radiação de onda longa (ROL) e temperatura e salinidade da coluna de água.

Produto	Variáveis	Resolução Espacial	Resolução Temporal	Janela de tempo
ERA-Interim	TSM, vento (u, v), FCL, FCS, ROC e ROL	0,125°	mensal	1993-2018
Glorys12v1	Temperatura e salinidade da coluna de água	Horizontal: 12 km Vertical: 50 níveis $\sigma$	mensal	1993_2018

### 3.1.3: Concentração de Clorofila- $\alpha$

Para o estudo da variabilidade da clorofila- $\alpha$ , foram utilizados os produtos globais do Ocean Color – Climate Change Initiative (OC-CCI), os quais são construídos a partir de dados obtidos por distintos sensores (MERIS,

Aqua-MODIS, SeaWiFS e VIIRS). Disponíveis através do portal online da instituição (<https://esa-oceancolour-cci.org/>), os produtos distribuídos possuem uma resolução espacial de 4 km e resolução temporal mensal. Para o presente estudo, utilizou-se a janela de tempo total disponível de 1999 a 2015.

### **3.2: Metodologia**

Neste subtópico será apresentado uma breve descrição da sequência metodológica aplicada no presente estudo, seguido de subtópicos (de 3.2.1. até 3.2.5) destinados ao detalhamento da metodologia.

Para que pudéssemos alcançar os objetivos propostos neste estudo, inicialmente foi necessário encontrar os períodos de ocorrência do DSAS. Para isso, fez-se uso dos dados de temperatura da superfície do mar para que fosse computado o índice do DSAS. O próximo passo foi calcular as variáveis relacionadas a interação oceano-atmosfera que sofrem alguma modificação durante o período de atuação do DSAS. Deste modo, utilizamos os dados de velocidade do vento ( $u$  e  $v$ ) para estudarmos a dinâmica de Ekman dos oceanos, e as componentes do fluxo de calor (FCL, FCS, ROC e ROL) para encontrar o fluxo líquido de calor ( $Q_{NET}$ ) entre o oceano e a atmosfera. Sabendo os anos de ocorrência do DSAS através do índice previamente calculado, foram calculadas composições que representam os anos de DSAS positivo, negativo e anos neutros (sem ocorrência do DSAS).

Tanto a velocidade do vento quanto a fluxo líquido de calor são utilizados para o cálculo do parâmetro de estratificação ( $\Phi$ ). Com esse parâmetro, junto com as velocidades verticais obtidas através da dinâmica de Ekman e a concentração superficial de clorofila- $\alpha$  foi possível então discutir sobre a

influência do DSAS na dinâmica de ressurgência costeira nas áreas de estudo anteriormente descritas.

### **3.2.1: Índice do DSAS**

O índice do Dipolo Subtropical do Atlântico Sul (IDSAS) foi introduzido por Morioka *et al.* [2011], e vem sendo utilizado nos trabalhos que procuram observar alterações relacionadas a este modo climático. Seguindo Morioka *et al.* [2011] computamos o IDSAS fazendo uso dos dados de temperatura da superfície do mar (TSM) das reanálises do ERAI. O índice toma como base a diferença da média espacial das anomalias de TSM entre o polo sudoeste ( $aTSM_{SO}$ ), compreendido entre as coordenadas 30°S – 40°S; 10°W – 30°W, e o polo nordeste ( $aTSM_{NE}$ ), compreendido entre as coordenadas 15°S – 25°S; 0° – 20°W, para o período de dezembro, janeiro fevereiro e março (Eq. 1).

$$IDSAS = aTSM_{SO} - aTSM_{NE} \quad (1)$$

Para o período compreendido neste estudo, de janeiro de 1993 a dezembro de 2018, o cálculo dos índices se iniciou em dezembro de 1993. Com isso, cada valor do IDSAS representa a média dos relativos meses a cada dois anos (1993/1994, 1994/1995, 1995/1996 e assim sucessivamente). Realizados os cálculos dos índices, são considerados anos de ocorrência da fase positiva do DSAS aqueles nos quais o IDSAS é maior ou igual a +0,8°C, enquanto que anos de ocorrência de DSAS negativo são aqueles em que o IDSAS é menor ou igual a -0,8°C.

### **3.2.2: Dinâmica de Ressurgência Costeira**

O estudo dos processos de ressurgência leva em conta o bombeamento de Ekman ( $W_{EK}$ ), o qual é um resultado direto da convergência ou divergência

dos transportes integrados de Ekman horizontais, intrinsecamente ligados ao rotacional da tensão de cisalhamento do vento na superfície do mar (Fig. 1 e Fig. 2). Para computarmos os transportes horizontais de Ekman precisamos calcular a tensão de cisalhamento  $\mathbf{T}$  exercida pelo vento sobre a superfície dos oceanos, expressa por  $\mathbf{T} = T_x \mathbf{i} + T_y \mathbf{j}$ , e cujas componentes podem ser encontradas através das seguintes equações:

$$\tau_x = \rho_{ar} \cdot Cd \cdot u \cdot (\overrightarrow{W}_{SPD}) \quad (2)$$

$$\tau_y = \rho_{ar} \cdot Cd \cdot v \cdot (\overrightarrow{W}_{SPD}) \quad (3)$$

onde  $\tau_x$  e  $\tau_y$  representam as componentes das tensões de cisalhamento do vento sobre a superfície do mar nas direções zonal e meridional, respectivamente ( $N \cdot m^{-2}$ ),  $\rho_{ar}$  é a densidade do ar ( $1,255 \text{ Kg} \cdot m^{-3}$ ),  $Cd$  é o coeficiente de arrasto o qual é adimensional e proporcional a magnitude da velocidade do vento [Smith *et al.* 1988],  $u$  e  $v$  representam as componentes de velocidade do vento nas direções zonal e meridional, respectivamente ( $m \cdot s^{-1}$ ), e  $W_{SPD}$  é a magnitude do vetor velocidade horizontal do vento ( $m \cdot s^{-1}$ ). A partir das tensões de cisalhamento obtidas podemos então deduzir a dinâmica de Ekman nas três dimensões. O próximo passo, então, foi calcular os transportes integrados horizontais de Ekman (Eq. 4 e Eq. 5) e a velocidade vertical da água do mar, induzida pela tensão de cisalhamento na superfície dos oceanos (Eq. 6).

$$M_x = -\frac{\tau_y}{\rho_0 f} \quad (4)$$

$$M_y = \frac{\tau_x}{\rho_0 f} \quad (5)$$



$$W_{EK} = \frac{1}{\rho_0 f} \left( \frac{\partial \tau_y}{\partial x} - \frac{\partial \tau_x}{\partial y} \right) \quad (6)$$

Nestas equações  $M_x$  e  $M_y$  são, respectivamente, as componentes zonal e meridional do transporte horizontal de Ekman ( $m^2.s^{-1}$ ),  $W_{EK}$  a velocidade do Bombeamento de Ekman ( $m.s^{-1}$ ),  $\rho_0$  é a densidade média dos oceanos ( $1024 \text{ kg.m}^{-3}$ ) e  $f$  o parâmetro de Coriolis (o qual varia com a latitude, em  $s^{-1}$ ). Sendo que,  $W_{EK}$  assume um valor positivo em regiões favoráveis aos processos de ressurgência e negativos em regiões com condições desfavoráveis a esses processos.

### 3.2.3: Fluxo Líquido de Calor

O fluxo líquido de calor ( $Q_{NET}$ , em  $W.m^{-2}$ ) é encontrado a partir das diferentes componentes da troca de calor entre o oceano e a atmosfera, em  $W.m^{-2}$ : fluxo líquido de calor sensível (FCS), fluxo líquido de calor latente (FCL), radiação de onda curta incidente na superfície dos oceanos (ROC), radiação de onda longa emitida pela superfície dos oceanos (ROL). Com isso, o  $Q_{NET}$  é o resultado da soma entre todas as componentes citadas acima, como demonstrado na equação 7 a seguir:

$$Q_{NET} = FCS + FCL + ROC + ROL \quad (7)$$

Sempre que  $Q_{NET} > 0$  teremos um fluxo líquido de calor da atmosfera para o oceano, indicando um aumento na quantidade de calor do oceano. Quando  $Q_{NET} < 0$  o fluxo líquido será do oceano para a atmosfera, indicando uma perda de calor do oceano para a atmosfera.

### 3.2.4 Parâmetro de estratificação

O parâmetro de estratificação  $\Phi$  (em  $J.m^{-3}$ ) [Simpson & Bowers, 1981] é utilizado como um “proxy” do estado da estrutura vertical da coluna de água

sobre a plataforma continental. O parâmetro descreve a coluna de água com base na relação entre a flutuabilidade do fluido, a qual é diretamente relacionada ao fluxo líquido de calor entre a superfície do oceano e atmosfera, e a mistura induzida pelo trabalho realizado pelo vento. A relação é descrita pela equação a seguir:

$$\Phi = \left( \frac{\alpha g Q_{NET}}{2C_p} \right) \Delta t - e_s k_s \rho_a \left( \frac{S^3}{h} \right) \Delta t \quad (8)$$

onde  $\alpha$  é o coeficiente de expansão volumétrica da água do mar ( $1,67 \times 10^{-4} \text{ } ^\circ\text{C}^{-1}$ ),  $g$  a aceleração da gravidade ( $9,81 \text{ m.s}^{-2}$ ),  $Q_{NET}$  é o fluxo líquido de calor na superfície dos oceanos,  $C_p$  é a capacidade térmica da água do mar ( $4000 \text{ J.kg}^{-1}.\text{ } ^\circ\text{C}^{-1}$ ),  $e_s$  é o coeficiente de eficiência de mistura pelo vento (0.023) [Simpson *et al.* 1978],  $k_s$  ( $\sim 2,4 \times 10^{-5}$ ) é o produto entre o coeficiente de arrasto do vento ( $C_D$ ) e o coeficiente de arrasto da primeira camada de água induzida pela ação do vento ( $\sim 0,02$ ),  $S$  é a velocidade horizontal do vento ( $\text{m.s}^{-1}$ ),  $h$  (m) é a profundidade da coluna de água e  $\Delta t$  o intervalo de um mês expresso em segundos (neste estudo utilizamos produtos que representam médias mensais de dados diários).

Com isso, o parâmetro de estratificação  $\Phi$  nos diz se o trabalho realizado pela ação do vento foi capaz de quebrar a estratificação vertical induzida pelo fluxo de calor. Deste modo, quando  $\Phi > 0$ , a coluna de água estará estratificada e para  $\Phi < 0$  a coluna de água estará misturada.

### 3.2.5: Composições

Para identificar as anomalias de velocidade do vento,  $M_X$  e  $M_Y$ ,  $W_{EK}$ ,  $Q_{NET}$  e temperatura da coluna d'água foram construídas composições de médias temporais dos anos de ocorrência do DSAS (positivos e negativos,

separadamente) e dos anos neutros. Com isso, as diferenças entre os anos de ocorrência do DSAS são encontradas subtraindo a composição de anos neutros das composições dos anos de DSAS.

Com base em Sterl & Hazeleger [2003] e Morioka *et al.* [2011], as composições dos sistemas atmosféricos (e.g. vento e  $Q_{NET}$ ) e de seus processos derivados (e.g.  $W_{EK}$ ) foram construídas utilizando os meses de outubro, novembro e dezembro, indicados como os meses em que as modificações atmosféricas estão mais intensas. Para a temperatura da água, utilizamos os meses de dezembro, janeiro e fevereiro. As composições foram construídas após a remoção do ciclo anual e da tendência linear de longo período, computadas para todas as variáveis.

### **3.2.6: Clorofila-a**

Como não se sabe qual o período exato, e nem se os organismos fitoplanctônicos respondem as mudanças dinâmicas associadas ao DSAS, optou-se por construir séries temporais das composições da concentração superficial de clorofila-a para este estudo. O objetivo é que esta série viesse a cobrir o período de desenvolvimento e enfraquecimento do DSAS, com intervalo de tempo indo de junho (anterior ao pico do DSAS) a abril (posterior ao pico do DSAS). Com isso, podemos buscar uma possível ligação entre as anomalias na concentração de clorofila-a e as anomalias da dinâmica de ressurgência.

Para este fim, foram selecionados quatro locais específicos em ambas as áreas de estudo (Fig. 7), de onde extraímos seções verticais que vão da costa até 200 km de distância (região aproximada da ação do bombeamento de Ekman). Na costa do Brasil, selecionamos a secção em frente a ressurgência

de CFB (Fig. 7a) e em frente a ressurgência no CSM (Fig. 7a). Para a área de estudo da costa sudoeste do continente Africano, selecionamos as regiões próximas a Cape Frio (CFN, Fig. 7b) na Namíbia e Santa Helena Bay (SHB, Fig. 7b) na África do Sul. Computou-se, então, médias espaciais levando em conta à distância de até 200 km da costa, em frente a cada local, para o bombeamento de Ekman ( $W_{EK}$ ), parâmetro de estratificação  $\Phi$  e concentração superficial de clorofila-a ( $mg.m^{-3}$ ). O que permite computar as composições de séries temporais para eventos de DSAS positivo, negativo e anos sem a ocorrência do DSAS (neutros). As séries temporais das composições das anomalias dos anos de ocorrência do DSAS são calculadas da subtração entre as composições das séries de DSAS (positivo e negativo) e a série das composições dos anos neutros.

Destes mesmos quatro locais, foram extraídas seções verticais de temperatura na coluna de água produto GLO, com 200 km de comprimento a partir da costa e 200 m de profundidade. Estas seções possibilitaram a observação de modificações relacionadas aos eventos do DSAS na coluna de água. Entretanto, as composições e as diferenças foram construídas com base no capítulo 3.2.5.

## Capítulo IV: Artigo Científico

Para a obtenção do título de Mestre pelo Programa de Pós-Graduação em Oceanologia, é requerido que o discente realize a submissão de, pelo menos, um artigo científico como primeiro autor em periódico com corpo indexado. Desse modo, os resultados da pesquisa desenvolvida durante o período de mestrado e a discussão dos resultados serão apresentados em forma de artigo neste Capítulo. O primeiro manuscrito, de autoria de Luiz Henrique Oliveira da Silva e José Luiz Lima de Azevedo, é intitulado “**On the South Atlantic coastal upwelling variability: The influence of the South Atlantic Subtropical Dipole**” e foi submetido para publicação no periódico “**Journal of Marine Systems**”.

### 1. INTRODUCTION

Coastal upwelling is among the main processes associated with primary productivity in continental shelf regions. These are processes that involve the vertical transport of subsurface water (colder and nutrient-rich) to the surface, linked to the offshore Ekman transport which is, in turn, associated with the direction of the near ocean surface winds (e.g. Ekman, 1905; Carr, 2001; Mann and Lazier, 2005).

A great effort has been made in recent years to understand the relationship between coastal upwelling processes and atmospheric changes observed during climate modes of variability. On the east coast of the Pacific Ocean, more specifically on the Peru coast, Espinoza-Morriberón et al. (2017) and Mogollón and Calil (2017) used physical-biogeochemical coupled models to describe changes in the water column during El-Niño Southern Oscillation (ENSO) mode. The authors show that, during El-Niño (La-Niña) periods, the anomalous warming (cooling) of the ocean surface layer in coastal regions

intensifies (weakens) the vertical stratification, making it difficult (facilitating) the transport of nutrients to the photic zone. Espinoza-Morriberón et al. (2017) also show that, even with the intensification of winds during the El-Niño period, there is a weakening of vertical transport due to increased stratification. In the South China Sea Jing et al. (2011) studied changes in the dynamics of Ekman pumping directly associated with changes in the wind field during the 1997/1998 El-Niño. Through in situ data and numerical modeling, the authors found that during this period there is an intensification of winds favorable to the upwelling processes in the China coast and, at the same time, a disadvantage of the process in the Vietnam coast. On the contrary to what was observed in Peru coast, the intensification (weakening) of winds in the South China Sea amplifies (reduces) the rise of subsurface waters. In the Indian Ocean, Sankar et al. (2019) investigated eastern Arabian Sea coastal dynamics during the Indian Ocean Dipole (e.g. Saji et al., 1999), bringing as a result the importance of anomalous westerly winds during the negative events of the climatic mode. Due to these anomalies there is an intensification of wind speed in the extreme south of India, touching the coastal region and resulting in the intensification of surface chlorophyll-a (chl-a) concentration. The association of climate modes of variability with changes in coastal upwelling dynamics in the South Atlantic Ocean (SAO) is still something to be investigated, however, it is known that the SAO has the South Atlantic Subtropical Dipole (SASD) as the main climate mode of variability (Venegas *et al.*, 1997; Sterl and Hazeleger, 2003; Haarsma et al., 2005).

The general circulation of SAO is characterized by the presence of a large wind-induced subtropical gyre (e.g. Peterson and Stramma, 1991;

Stramma and England, 1999; Tomczak and Godfrey, 2003; Talley et al., 2011). In the eastern edge of this ocean the Benguela Current flows north, bringing cool waters to tropical regions and joining the south branch of the South Equatorial Current (SEC) that runs from east to west. Upon reaching Brazil coast the SEC bifurcate and one of its branches flow southward as the Brazil Current (BC). At approximately 40°S, BC meets the Malvinas Current, generating the region of the Brazil-Malvinas Confluence. The two currents come off the coast and flow eastern to the South Africa coast as the South Atlantic Current.

Over the SAO act the high pressure atmospheric system know as South Atlantic Subtropical High, which generates a climatological anticyclonic rotation winds pattern (Fig. 1a). There are associated upwelling systems in both the western and eastern boundary of the SAO. The two major upwelling regions located in the southeast-south Brazilian coast (SBC) are the Cabo Frio (CFB, Fig. 1b) and Cabo Santa Marta (CSM, Fig. 1b) upwelling systems (Campos *et al.*, 1995, 2013; Guimaraens and Coutinho, 2000; Castelao *et al.*, 2004; Möller *et al.*, 2008; Mazzini and Barth, 2013). Coastal upwelling processes in these regions are favored mainly by northeast winds, which blow almost parallel to the coast and with more intensity during the austral summer. In addition to the winds, other mechanisms are also important for the development of the upwelling processes in CFB region, such as bathymetry and the coastline orientation change, the meandering of BC and the interaction between BC and the shelf break (Rodrigues and Lorenzetti, 2001; Aguiar *et al.*, 2014). In the CSM region, the northeast winds do not always dominate. The CSM is near to great freshwater discharge rivers (Patos Lagoon and Rio de la Plata). According

to Möller *et al.* (2008), Palma and Matano (2009) and Campos *et al.* (2013), the passage of cyclonic atmospheric systems (changing the predominant winds direction to the south/southwest during the austral winter) disfavor the coastal upwelling system and fill the CSM platform with waters from river discharge.

In the eastern boundary of the SAO is the Benguela Upwelling System (BUS) (Nelson and Hutchings, 1983; Shannon and Nelson, 1996; Mackas *et al.*, 2006; Hutchings *et al.*, 2009). As part of the Eastern Boundary Upwelling Systems, BUS is one of the most productive coastal regions in the world (Carr, 2001; Chavez and Messié, 2009). The main mechanism of local coastal upwelling is linked to the southeastern trade winds, which blow parallel to the coast of Namibia and the west coast of South Africa. The northern limit of the BUS (~18°S) is the Angola Gyre, a cyclonic gyre centered on approximately 10°S-5°E responsible for bringing warm waters to the coastal region bypassed by the Benguela Current through the Angola-Benguela front (Hutchings *et al.*, 2009; Bachèlery *et al.*, 2016; Tchupalanga *et al.*, 2018). To the south, the BUS interacts with the Indian Ocean waters through the Agulhas rings, which carry warm and saline waters from this ocean to the OAS (e.g. Garzoli *et al.*, 1999; Beal, 2009; Biastoch *et al.*, 2015). In addition, the region is also characterized by the passage of cyclonic atmospheric systems linked to the wave oscillation of the southern hemisphere westerly winds (Nelson and Hutchings, 1983).



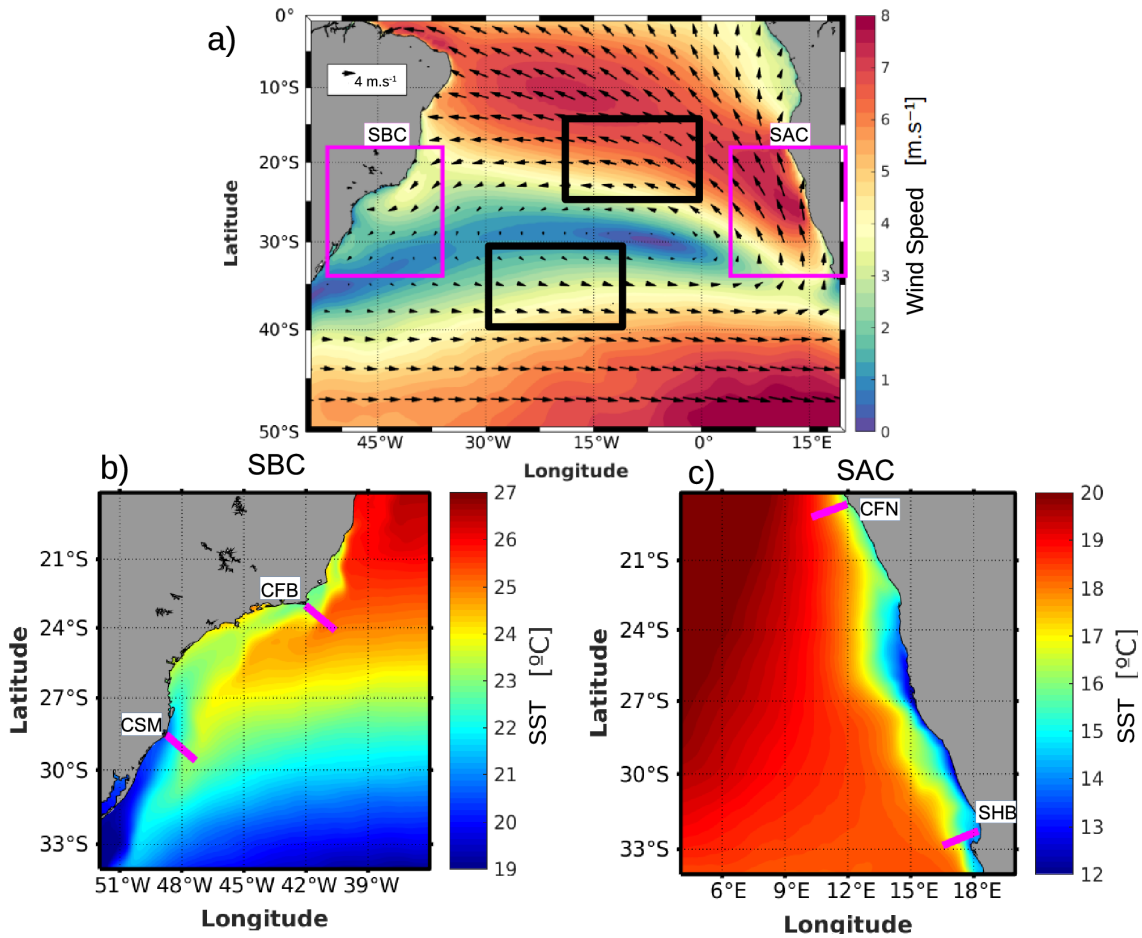


**Fig. 1.** a) Climatological pattern of intensity (shading) and wind direction (vectors) over the South Atlantic Ocean for the period 1993-2018. The magenta rectangles indicate the study areas of the Southeast-South Brazilian coast (SBC) and the Southwest African coast (SAC). The black boxes outline the areas of the northeast pole (15°S - 25°S and 0°W - 20°W) and the southwest pole (30°S - 40°S and 10°W - 30°W) from which the spatial averages of sea surface temperature (SST) anomalies were calculated and applied in the calculation of the South Atlantic Subtropical Dipole index (SASDI). In b) and c) climatological pattern of SST of the regions demarcated by the magenta rectangles of SBC and SAC in a), respectively. The magenta lines indicate the sections used in this study for Cabo Frio (CFB) and Cabo Santa Marta (CSM) at SBC and Cape Frio (CFN) and Santa Helena Bay (SHB) at SAC. The climatology shown in a) was calculated using the ERA-Interim products and in b) and c) through the SST ESA-CCI products.

**South Atlantic Subtropical Dipole (SASD)** - This dipole is a climate mode of variability characterized by sea level pressure (SLP) anomalies in the Subtropical South Atlantic High (SASH) region and by a northeast-southwest gradient in the spatial distribution of sea surface temperature (SST) anomalies during the austral summer (Venegas et al., 1997; Palastanga et al., 2002; Haarsma et al., 2005). These SST anomalies are associated with atmospheric

oscillations in the SLP, which modify the intensity of the southeast trade winds and, consequently, the latent heat flux between the ocean and the atmosphere (Fauchereau et al., 2003; Sterl and Hazeleger, 2003). The development and decay process of SASD was described by Sterl and Hazeleger (2003) and later by Morioka et al. (2011). The latter included the variability of the mixed layer depth in their study. The characterization of a positive or negative event is proposed by Morioka et al. (2011) through the South Atlantic Subtropical Dipole Index (SASDI). To compute the SASDI the authors take into account two regions of the SAO, which are called the southwest pole (30°S - 40°S; 10°W - 30°W) and the northeastern pole (15°S - 25°S; 0° - 20°W), indicated in Fig. 1a as black rectangles. Thus, the SASDI is computed through the difference of the spatial averaged sea surface temperature anomalies between the southwest and northeast poles, for the entire interval from December to March. Years in which the region is under a positive SASD event (SASD+) are considered to be those in which the value of SASDI is greater than or equal to +0.8 °C, whereas years of negative SASD (SASD-) event will be considered years in which that this difference is less than or equal to -0.8 °C. The years in which the SASDI value is between -0.8 °C and +0.8 °C are considered neutral years. The SASD+ is characterized by an anomalous increase in SLP in the SASH region, which intensifies the trade winds and, consequently, results in negative SST anomalies in the northeast pole. The opposite is observed in the region of the southwest pole, thus resulting in negative SST anomalies. This entire process is reversed during the SASD- years. As a consequence of these processes, SASD has been associated with changes in the rainfall regime in some regions of South America and Africa. The negative phase of SASD, which is associated

with the reduction in the intensity of the trade winds and a positive SST anomalies at northeast pole, is placed as being responsible for positive anomalies in the rainfall rates in Northeast Brazil and South Africa central regions (Reason, 1998; Pezzi and Cavalcanti, 2001; Haarsma et al., 2003; Wainer et al., 2014). Regarding interconnections characteristics of this mode, (Rodrigues et al., 2015) used results from numerical modeling to explain what would be the trigger for the processes that would result in the formation of SASD. The authors associate it with geopotential height anomalies at certain atmospheric levels, pointing out a link between El-Niño (La-Niña) years in the central Pacific and SASD- (SASD+) events in SAO. This connection occurs through Rossby waves, which move from the Pacific Ocean to the South Atlantic through the southernmost region of South America.

Taking into account the atmospheric and oceanic changes related to SASD, we can consider that the dynamics of the SAO, especially the coastal upwelling systems associated with oceanic borders, must undergo some change under the influence of climatic mode. In this way, the present study seeks to understand how the atmospheric system associated with SASD, whether in its positive or negative phase, interacts with the coastal upwelling dynamics in the SBC and on the west coast of Namibia and southwest South Africa, here referred to as the southwestern African coast (SAC). Thus, the study areas of the present work include the three distinct coastal upwelling systems in the SAO mentioned above: Cabo Frio (CFB) and Cabo Santa Marta (CSM) at SBC (Fig. 1b) and the Benguela Upwelling System (BUS) at SAC (Fig. 1c).

This paper is organized as follows: the present introduction, the applied methodology is presented in chapter 2 and, subsequently, the results obtained and discussions are presented in chapter 3 (this chapter is subdivided in chapter 3.1., about SBC, and in chapter 3.2., about SAC). Finally, section 4 presents the conclusions of this work.

## 2. METHODS

In this chapter will be presented the reanalysis products used and the methodological procedures applied to achieve the objectives of this study. In chapter 2.1, we present the atmospheric and oceanic products used. In chapter 2.2 we provide information on how these products were worked on, from the methodology applied to compute the SASDI through the Ekman dynamics, construction of the compositions and, finally, the study of the temporal evolution of chl-a anomalies during the SASD periods.

### 2.1. Reanalysis products

The atmospheric reanalysis products used in this work were obtained from the European Center for Medium-Range Weather Forecast portal (<https://www.ecmwf.int/>, ECMWF). The data from ERA-Interim (ERA-I) reanalysis of SST, wind (u, v) and the components of the net heat flux (NHF), comprise the period from 1979 to 2018, with a monthly temporal resolution. For this study we used the reanalysis interval from 1993 to 2018 with a spatial resolution of  $0.125^\circ$ , in order to coincide with the time interval of the oceanic reanalysis products presented below.

To represent oceanic conditions, global oceanic reanalysis products, GLORYS12v1 (GLO), from the Copernicus Marine Environment Monitoring Services (CMEMS) were used, which have ERAI reanalysis products as atmospheric forcing. GLO products have data assimilation of temperature and salinity profiles in situ, free sea surface and sea surface temperature. This is the first version of the product with a spatial resolution of 12 km and 50 levels of depth, which has daily and monthly products, covering the period from 1993 to 2018. For this work, we used the monthly temporal resolution of the entire available period of temperature and salinity.

To study the variability of chl-a, the global products of the Ocean Color - Climate Change Initiative (OC-CCI) were used, which are constructed from data obtained by different satellite sensors (MERIS, Aqua-MODIS, SeaWiFS and VIIRS). Available through the institution's portal (<https://esa-oceancolor-cci.org/>), the products distributed have a spatial resolution of 4 km and a monthly temporal resolution. For the present study was used the time interval from 1999 to 2018.

## 2.2. Methodology

Initially it was necessary to find the periods of occurrence of SASD and, for that, the SASDI was computed (Morioka *et al.*, 2011) calculated by the difference in SST anomalies, over the months of December-March, between the southwest pole and the northeast pole (Fig. 1a). Differences  $\geq +0.8$  are SASD+ events and  $\leq -0.8$  are SASD- events.

The study of upwelling processes takes into account the Ekman pumping ( $W_{EK}$ ) and the Ekman transport. The first is a direct result of convergence or

divergence of the depth integrated Ekman transport, intrinsically linked to the wind stress curl at the sea surface. The Ekman transport and the  $W_{EK}$  vertical velocities are calculated from equations 1, 2 and 3 below:

$$M_x = -\frac{\tau_y}{\rho_0 f} \quad (1)$$

$$M_y = \frac{\tau_x}{\rho_0 f} \quad (2)$$

$$W_{EK} = \frac{1}{\rho_0 f} \left( \frac{\partial \tau_y}{\partial x} - \frac{\partial \tau_x}{\partial y} \right) \quad (3)$$

In these equations  $M_x$  and  $M_y$  are, respectively, the zonal and meridional horizontal Ekman transport components ( $m^2 \cdot s^{-1}$ ),  $W_{EK}$  is the vertical velocity associated with Ekman pumping ( $m \cdot s^{-1}$ ),  $\rho_0$  is the average density of the oceans (here considered as  $1024 \text{ kg} \cdot m^{-3}$ ),  $f$  is the Coriolis parameter (which varies with latitude, in  $s^{-1}$ ) and  $\tau_x$  and  $\tau_y$  are, respectively, the zonal and meridional components of the sea surface wind stress curl.  $W_{EK}$  assumes a positive (negative) value in regions favorable (unfavorable) to resurgence processes.

The NHF (in  $W \cdot m^{-2}$ ) is calculated from the sum of the different components involved in the heat exchange between the ocean and the atmosphere: net sensible heat flux (SHF), net latent heat flux (LHF), short wave radiation on the ocean surface (SWR) and long wave radiation emitted by the ocean surface (LWR) as shown in equation 4 below:

$$NHF = SHF + LHF + SWR + LWR \quad (4)$$

Whenever  $NHF > 0$  there will be a heat flux from the atmosphere to the ocean, indicating an increase in the ocean heat content. When  $NHF < 0$  the net

flux will be from the ocean to the atmosphere, indicating a decrease in ocean heat content.

The stratification parameter  $\Phi$  (in  $\text{J}\cdot\text{m}^{-3}$ ) (Simpson and Bowers, 1981), calculated using equation 5, is used as a proxy for the state of the vertical structure of the water column on the continental shelf, describing the relationship between the buoyancy of the fluid and the stirring induced by the working of the wind stress.

$$\Phi = \left( \frac{\alpha g NHF}{2C_p} \right) t - e_s k_s \rho_a \left( \frac{S^3}{h} \right) t \quad (5)$$

where  $\alpha$  is the coefficient of volumetric expansion of seawater ( $1.67 \times 10^{-4} \text{ }^\circ\text{C}^{-1}$ ),  $g$  gravitational acceleration ( $9.81 \text{ m}\cdot\text{s}^{-2}$ ),  $NHF$  ( $\text{W}\cdot\text{m}^{-2}$ ) is the monthly average of the NHF,  $C_p$  is the thermal capacity of seawater ( $4000 \text{ J}\cdot\text{kg}^{-1} \text{ }^\circ\text{C}^{-1}$ ),  $e_s$  is the efficiency of wind mixing (0.023) (Simpson *et al.*, 1978),  $k_s$  ( $\sim 2.4 \times 10^{-5}$ ) is the product between the wind drag coefficient and the drag coefficient of the first layer of water induced by the wind action ( $\sim 0.02$ ),  $S$  is the wind speed ( $\text{m}\cdot\text{s}^{-1}$ ) monthly averaged,  $t$  the interval of one month expressed in seconds and  $h$  (m) is the depth of the water column.

We calculated the composites of the NHF data, wind at 10 m,  $W_{EK}$ , Ekman transport ( $M_x$  and  $M_y$ ) and temperature of the water column for the years of occurrence of SASD+, SASD- and neutral years. For NHF, wind speed and Ekman dynamics we use the months of October-December as a base, while for the water column temperature we use the December-February interval and . The time series of composite of the neutral years and the time series of composite anomalies of the SASD+ and SASD- years was calculated for  $W_{EK}$ , stratification parameter  $\Phi$  and chl-a considering the period throughout the

grow and decay of SASD. The time series correspond to space averaged values within 200 km from the coast (approximately the distance of the favorable Ekman pumping) at CFB and CSM at SBC (magenta lines in Fig. 1b) and at Cape Frio (CFN) and St. Helena Bay (SHB) at SAC (magenta lines in Fig. 1c).

### 3. RESULTS AND DISCUSSION

Before any analysis about the coastal dynamics at the study areas, we will first identify the SASD years during the interval from 1993 to 2018. Afterwards, we will then be able to assess and discuss changes in coastal upwelling processes in the SBC and SAC and their possible relations with the SASD.

Calculating the SASDI (Morioka *et al.*, 2011) nine SASD years were identified in the interval from 1993 to 2018, which were used in the construction of the composites of wind speed, Ekman transport ( $M_H$ ),  $W_{EK}$ , NHF and water column temperature, with four SASD+ and five SASD- events. The remaining 16 years were considered to be neutral periods. As the time chla-a product time interval used in this study is from 1999 to 2018, for the time series of the chla-a composites, we use four SASD- events (2002/2003, 2004/2005, 2009/2010 and 2015/2016), two SASD+ events (2011/2012 and 2017/2018) and thirteen neutral years. The SASDI time series is shown in Fig. 2, with emphasis on the years of occurrence SASD events, which are also highlighted in table 1. In Fig. 2 it is possible to observe the SASDI interannual variability, with the red (blue) vertical bars illustrating the years of SASD+ (SASD-). Between the SASD+ years of 1998/1999 and 2011/2012, SASDI indicates a sequence of three occurrences of



SASD- (2002/2003, 2004/2005 and 2009/2010) without any SASD+ events being identified among them. Regarding the intensity of the events, the summer of 1996/1997 had the most intense SASD+ event, reaching a SASDI = 1.2 °C, and in the summer of 2009/2010 the most intense SASD- with SASDI = -1.3 °C. Within the interval in which the present study coincides with the past studies by Morioka *et al.* (2011) and Rodrigues *et al.* (2015) (from 1993 to 2010), the same events were identified, that is, SASD+ of 1996/1997 and 1998/1999 and SASD- of 1994/1995, 2002/2003, 2004/2005 and 2009/2010, being that Goes *et al.* (2019) identified the SASD- event of the summer of 2009/2010 by analyzing in situ data obtained through XBTs. In addition to these events the present study identified three new events: SASD+ from 2011/2012 and 2017/2018 and SASD- from 2015/2016.

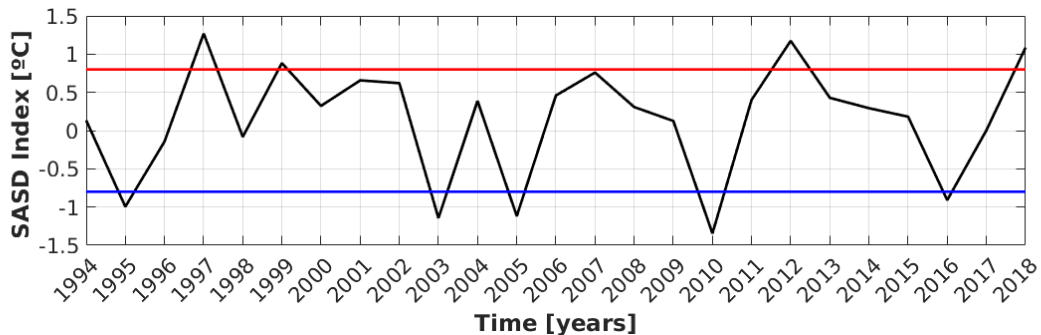


**Fig. 2:** SASDI time series computed based on Morioka *et al.* [2011], using ERAI SST products. The horizontal red (blue) line represents the SASDI = +0.8 °C (SASDI = -0.8 °C) thresholds.

**Tab. 1:** Years of occurrence of the SASD variability pattern. The years in which positive (negative) events occurred are indicated by SASD+ (SASD-).

PHASE	Years of occurrence				
SASD+	96/97	98/99	11/12	17/18	
SASD-	94/95	02/03	04/05	09/10	15/16

Following will be presented the results obtained with respect to physical processes associated with the dynamics of upwelling in the two study areas. In

order to observe differences in the responses of upwelling processes occurring in the SBC and on the SAC related to SASD, the results for each region will be presented separately.

### 3.1 Southern-South Brazilian Coast

In this chapter, we will cover the SBC and its main upwelling systems at CFB and CSM regions. We will discuss atmospheric changes during the peaks of both SASD events and the consequent of these changes in Ekman dynamics (horizontal Ekman transport and Ekman pumping), in the vertical stratification structure and in the temperature distribution in the water column, in addition to identifying whether these changes outcome in the local concentration of chl-a.

#### 3.1.1 Positive SASD

Figures 3a, 3b and 3c show the composites of neutral years while Fig. 3d, 3e and 3f show the composite anomalies during SASD+ of surface winds speed ( $\text{m}\cdot\text{s}^{-1}$ ), horizontal Ekman transport ( $M_H$ ,  $\text{m}^2\cdot\text{s}^{-1}$ ) and Ekman pumping ( $W_{EK}$ ,  $\text{m}\cdot\text{day}^{-1}$ ). In these last three figures the shades of red (blue) represent positive (negative) differences between the SASD+ and neutral years. The vectors in 3d and 3e represent the anomalous direction of the wind and the horizontal transport of Ekman, respectively. The statistically significant differences (CI: 80%,  $p$ -value  $<0.02$ ) are outlined by the solid black line. Only the differences that respond to this confidence interval will be presented in the numerical results throughout this paper.

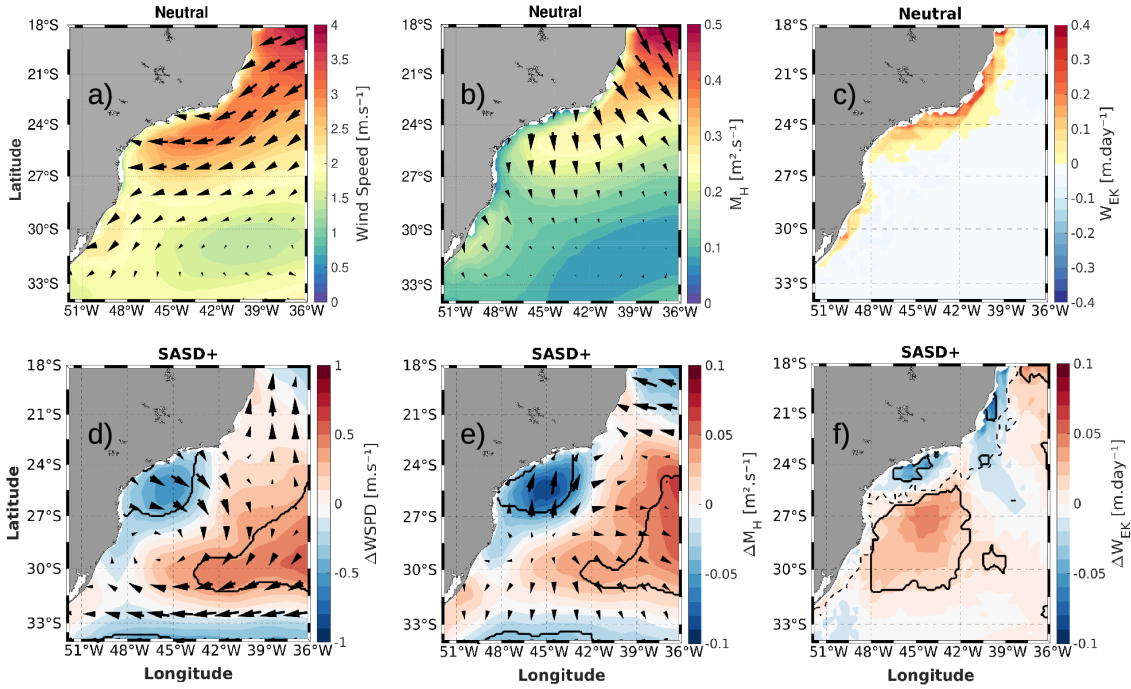


**Fig. 3:** Neutral composites (October-December) of a) the intensity (shading) and direction (vectors) of the wind ( $\text{m}\cdot\text{s}^{-1}$ ), b) the intensity (shading) and direction (vectors) of the Ekman transport ( $M_H$ , in  $\text{m}^2\cdot\text{s}^{-1}$ ) and c) the Ekman pumping ( $W_{EK}$ ,  $\text{m}\cdot\text{day}^{-1}$ ) for the southeastern-south Brazilian coast (SBC). The lower figures show the difference between the SASD+ and neutral composites of d) intensity (shading) and direction (vectors) of the wind speed ( $\Delta WSPD$ ,  $\text{m}\cdot\text{s}^{-1}$ ), e) the intensity (shading) and direction (vectors) of Ekman transport ( $\Delta M_H$ ,  $\text{m}^2\cdot\text{s}^{-1}$ ) and the f) Ekman pumping ( $\Delta W_{EK}$ ,  $\text{m}\cdot\text{day}^{-1}$ ). The solid black lines in the lower figures indicate the regions with significant differences for the 80% confidence interval. In f) the dashed contour line show the position in c) where  $W_{EK} = 0$ .

The anomalies observed in the wind field during the occurrence of SASD+ (Fig. 3d) are mainly marked by an anomalous cyclonic structure centered between  $28^\circ\text{S}$  and  $30^\circ\text{S}$ . This anomalous structure reduces the intensity of the winds in the Santos Basin region (between  $23^\circ\text{S}$ - $28^\circ\text{S}$  and  $42^\circ\text{W}$ - $49^\circ\text{W}$ ). In this region, the average of the significant differences in the magnitude of the wind speed is  $-0.4 \pm 0.1 \text{ m}\cdot\text{s}^{-1}$ , a reduction ranging from -10% to -20% in relation to neutral periods. The variability becomes more marked when we observe the persistence of patterns in Ekman dynamics (Fig. 3e and 3f). At the center of the cyclonic structure, an anomalous divergence from the  $M_H$  is generated, which implies in  $W_{EK}$  positive anomalies. The edge of this cyclone reduces the offshore Ekman transport in front of the coastal region

between 23°S and 26°S (Fig. 3e). In this case, the reduction result from the weakening of the wind previously described, decreasing Ekman transport by an average of  $-0.06 \pm 0.02 \text{ m}^2 \cdot \text{s}^{-1}$ , approximately one third of the transport during neutral years at local. In relation to the Ekman pumping anomalies (Fig. 3f), wind anomalies on the Brazilian coast between 23°S and 26°S result in a averaged significant weakening of approximately  $-0.04 \pm 0.01 \text{ m} \cdot \text{day}^{-1}$  of the positive vertical velocities in that area. In some parts of the Santos Basin coastal region the differences reach reductions up to 60%.

In the coastal region north of 23°S it is also possible to observe a weakening of positive vertical velocities (Fig. 3f). However, this occurs in a slightly different way from that observed in the Santos Basin. To the north of 23°S the winds have their direction slightly changed (Fig. 3d) by anomalies of south wind parallel to the coastline. In view of this, there is a weakening of the removal of water from the coastal region, which represents a disadvantage of the climatological process of upwelling through Ekman pumping. In this area, during the SASD+ years, positive vertical velocities are reduced by  $-0.06 \pm 0.01 \text{ m} \cdot \text{day}^{-1}$  ( $\sim -40\%$ ) on average.

As demonstrated by Sterl and Hazeleger (2003) and Morioka *et al.* (2011), there are differences in NHF anomalies between the poles of the SASD. During the SASD+ years, negative NHF anomalies in the northeast pole are more intense than positive anomalies in the southwest pole. The authors also show that these differences can also be noticed in the spatial distribution of these anomalies, so that the anomalies of the northeast pole are spatially more distributed during SASD- than SASD+ years. Thus, the distance from the Brazilian coast to the northeastern pole of the SASD+ means that this study

area has a heterogeneous and less intense distribution of NHF anomalies (Fig. 4b), especially in the continental shelf area. In the coastal region south of 27°S there is a weakening of the NHF to the ocean. In the north, in the region of the Santos Basin, the values of these differences are predominantly positive, intensifying the NHF towards the atmosphere to the ocean. No region showed statistically significant differences within the assigned confidence interval, indicating little influence of SASD+ on the spatial distribution of NHF along the SBC.

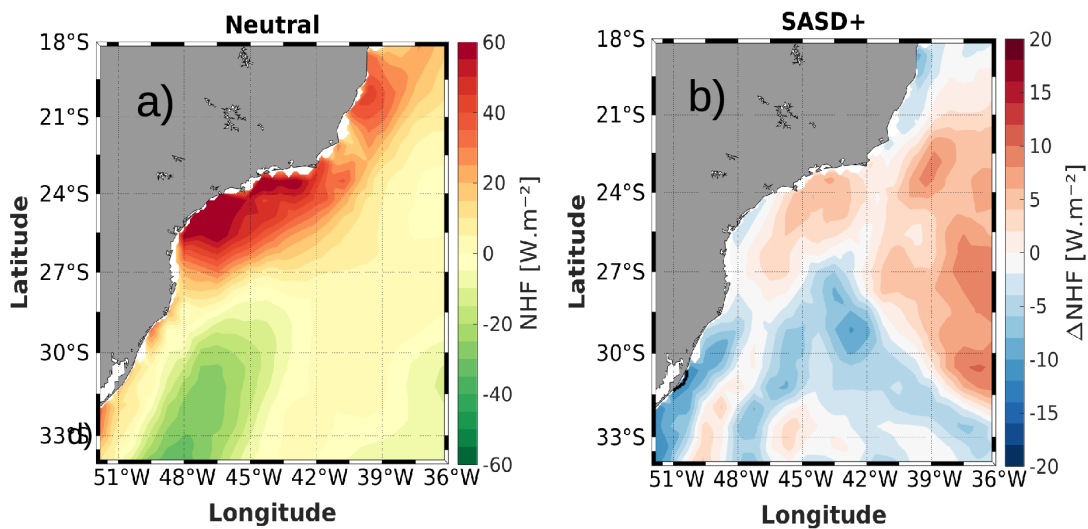


**Fig. 4:** a) Neutral years composite (October-December) of the net heat flux (NHF, in W.m<sup>-2</sup>) and b) SASD+ anomalies composite of the NHF ( $\Delta$ NHF, in W.m<sup>-2</sup>) in the southeastern-south Brazilian coast (SBC). Positive values in a) indicate a NHF from the atmosphere to the ocean.

It is known that others climate modes of variability can modify the surface chla-a concentration in the oceans, globally or locally (Yoder and Kennelly, 2003; Jing *et al.*, 2011; Espinoza-Morriberón *et al.*, 2017; Sankar *et al.*, 2019). Thus, using the OC-CCI chla-a data, we can observe whether anomalies in the ocean-atmosphere interaction mechanisms during SASD events influence the surface chla-a concentration. For that, time series of the composites of the  $W_{EK}$  (Eq. 3, m.day<sup>-1</sup>), the stratification parameter  $\Phi$  (Eq. 5, Jm<sup>-3</sup>) and the chla-a

surface concentration were obtained from the two sections of the main areas of coastal upwelling of SBC: CFB and CSM. The time series presented in Figs. 5a and 5b represent the spatial averages within the area of 200 km from the coast (magenta lines in Fig. 1b) and describe the climatological behavior of neutral years (from June to May). The Figs. 5c and 5d show the time series of the composite differences between the SASD+ and neutral years along the period of development of the climate mode.

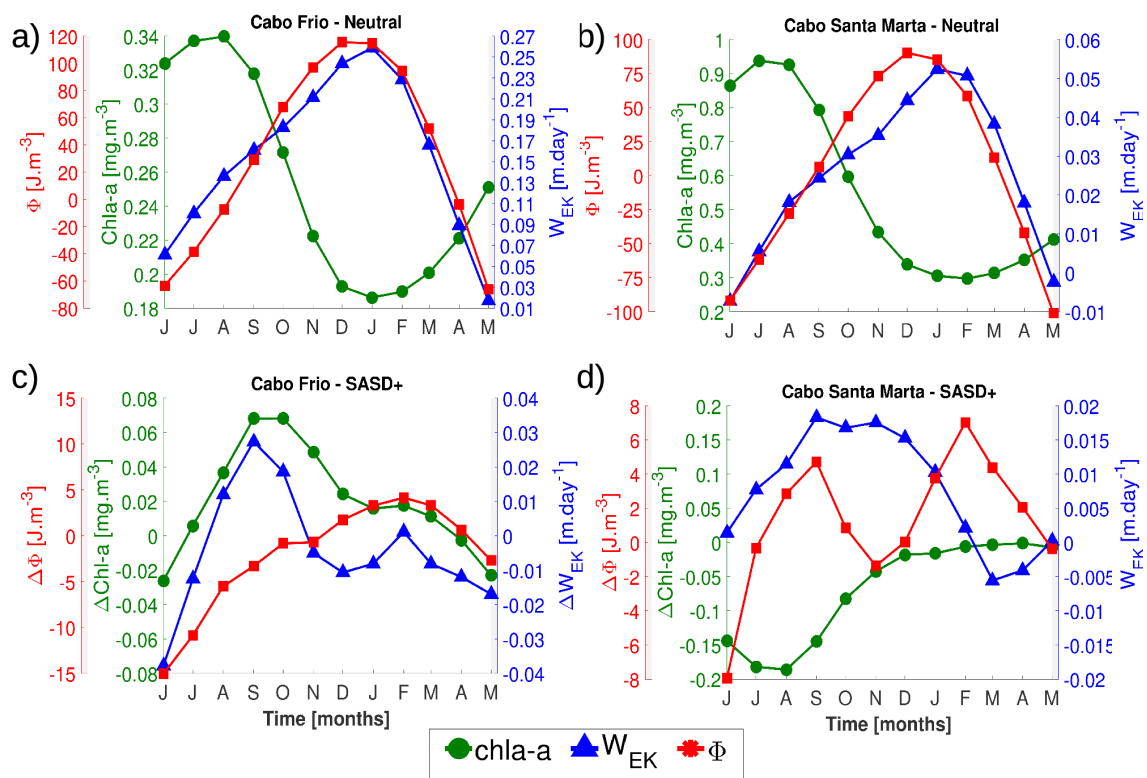


**Fig. 5:** a) Cabo Frio (CFB) and b) Cabo Santa Marta (CSM) time series of the neutral composites of the chlorophyll-a (chl-a, green line, in  $mg.m^{-3}$ ), Ekman pumping ( $W_{EK}$ , blue line, in  $m.day^{-1}$ ) and stratification parameter  $\Phi$  calculated according to equation 5 of the text ( $\Phi$ , red line, in  $J.m^{-3}$ ). In c) and d) the time of the SASD+ anomalies composite of the same variables ( $\Delta chl-a$ ,  $\Delta W_{EK}$ ,  $\Delta\Phi$ ) as a) and b). The time series were smoothed with a 3-month moving average filter.

In Figs. 5a and 5b we can see that the regions of CFB ( $\sim 23^{\circ}S$ ) and CSM ( $\sim 28^{\circ}S$ ) have a similar annual variability pattern during neutral years, but with different intensities. As already described by several authors (e.g. Gonzalez-Rodriguez, 1994; Castelao and Barth, 2006; Campos *et al.*, 2013; Mazzini and

Barth, 2013), during the austral summer both regions reach coastal upwelling favorable winds (N/NE) peak. The stratification parameter  $\Phi$  also reaches a positive maximum during the summer period, indicating strong stratification linked to solar radiation. This is because the parameter  $\Phi$  is directly proportional to the NHF, which is mainly modulated by the shortwave solar radiation (Simpson and Sharples, 2012a, 2012b). During this period, the concentration of chl-a is minimal, as stratification acts as a physical barrier that separates phytoplankton organisms from nutrient-rich waters. This barrier is broken by the wind induced vertical turbulent mixing during the austral winter/spring (Gonzalez-rodriguez *et al.*, 1992; Lopes *et al.*, 2006; Simpson and Sharples, 2012b), which allows the chl-a peak concentrations observed in both regions during the neutral years. The anomalies shown in Figs. 5c and 5d demonstrate how the SASD+ changes the dynamics of the CFB and CSM during its evolution period.

In the CFB (Fig. 5c) the period of atmospheric changes related to the formation of SASD+ occurs during the period from August to November. The  $W_{EK}$  anomalies are the result of the wind speed and direction anomalies, while parameter  $\Phi$  anomalies indicate how the interaction between wind speed and NHF changes the stratification structure of the water column. During the neutral years, from July to August the parameter  $\Phi$  is negative, which indicates a mixed water column. While from September the column begins to become more and more stratified. Hence, from July to August the parameter  $\Phi$  anomalies indicate an intensification of the vertical mixture and, from September to October they indicate a slight weakening of the stratification. These changes in the vertical structure of the water column, combined with the positive anomalies of  $W_{EK}$  from

August to October (which favor the rise of nutrient-rich waters in the photic zone) allow a more favorable environment for the development of photosynthetic organisms. This can be seen in chl-a anomalies, which reach a positive peak of  $\sim 0.07 \text{ mg}\cdot\text{m}^{-3}$  during the months of September and October, continuing with positive anomalies up to December. In Fig. 6b, it is possible to observe the entrance of colder waters (than those observed during neutral periods) through the continental shelf. The composite in Fig. 6b refer to the austral summer and show the intensified upwelling favorable conditions in the previous months throughout the evolution of SASD+. In this figure it is possible to see that the 18 °C isotherm (dashed line in the figure), relative to the South Atlantic Central Water (SACW) temperature upper limit (Castro and Miranda, 1998), approaches the surface. The intrusion of this water mass onto the platform is also a characteristic of the Brazilian coastal upwelling process (Gonzalez-Rodriguez *et al.*, 1992; Guimaraens and Coutinho, 2000; Coelho-Souza *et al.*, 2012). The fact that this isotherm is closer to the surface during the SASD+ years corroborates the upwelling process intensification observed in Fig. 5c.

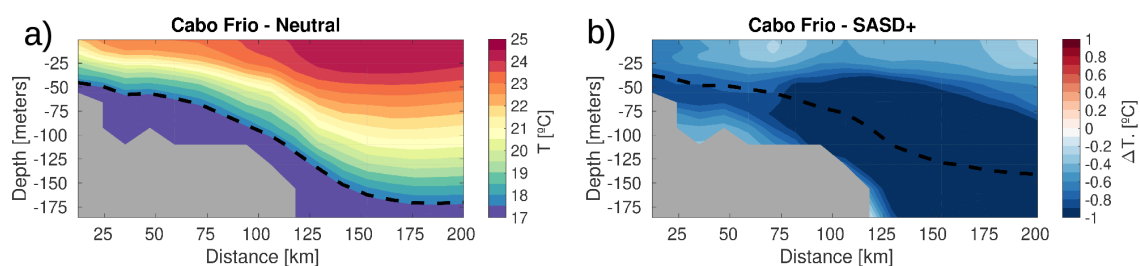


**Fig. 6:** Vertical section of a) the neutral years composite (December-February) and b) the SASD+ anomalies composite of the water column temperature ( $T$ , in  $^{\circ}\text{C}$ ) at Cabo Frio (CFB). The dashed line show the 18  $^{\circ}\text{C}$  isotherm (SACW  $<18^{\circ}\text{C}$ ) of a) the neutral years composite and b) the SASD+ events composite.

When we look at Fig. 5d, we can notice that the variation of chl-a in CSM does not have a direct relationship with the variability of the  $W_{\text{EK}}$  or with



that of the parameter  $\Phi$ . From July to January Ekman pumping maintains positive anomalies, indicating upwelling dynamics intensification. In comparison with CFB, the CSM region has vertical velocities that are up to an order of magnitude less intense (Fig. 5a and 5b). This causes the anomaly  $W_{EK}$  during SASD+ periods proportionately more pronounced, reaching an increase of  $W_{EK}$  up to 84%. However, in this case, the increase in the Ekman pumping process does not seem to be directly associated with an increase in the chl-a surface concentration. In the CSM region, with the exception of the November, the stratification parameter  $\Phi$  anomalies are positive along the SASD+ evolution process. This is a unfavorable upwelling condition, as can be seen in the negative anomalies of chl-a from July to January, even coinciding with the period of  $W_{EK}$  positive anomalies, indicating that in this case the stratification anomalies is more important than the  $W_{EK}$  anomalies. As in the CFB (Fig. 6), in the CSM (Fig. 7b) it is also possible to observe the 18 °C isotherm approaching the surface, reaching a depth of 10 m in the regions closest to the coast, indicating the intrusion of colder and nutrient-rich waters into the photic zone.

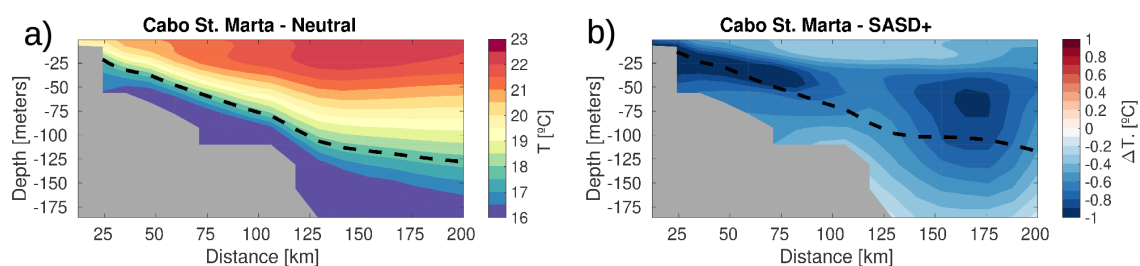


**Fig. 7:** Vertical section of a) the neutral years composite (December-February) and b) the SASD+ anomalies composite of the water column temperature ( $T$ , in °C) at Cabo Santa Marta (CSM). The dashed line show the 18 °C isotherm (SACW <18°C) of a) the neutral years composite and b) the SASD+ events composite.

### 3.1.2. Negative SASD

The negative SASD- is characterized by negative anomalies of the southeast trade winds and positive anomalies intensifying the mid-latitude

westerlies (Venegas *et al.*, 1997 ; Haarsma *et al.*, 2003; Sterl and Hazeleger, 2003). In Fig. 8, we show the neutral years composites of wind speeds, horizontal Ekman transport and Ekman pumping (Fig. 8a, 8b and 8c), as well as the composite anomalies of SASD- years (Fig. 8d, 8e and 8f).

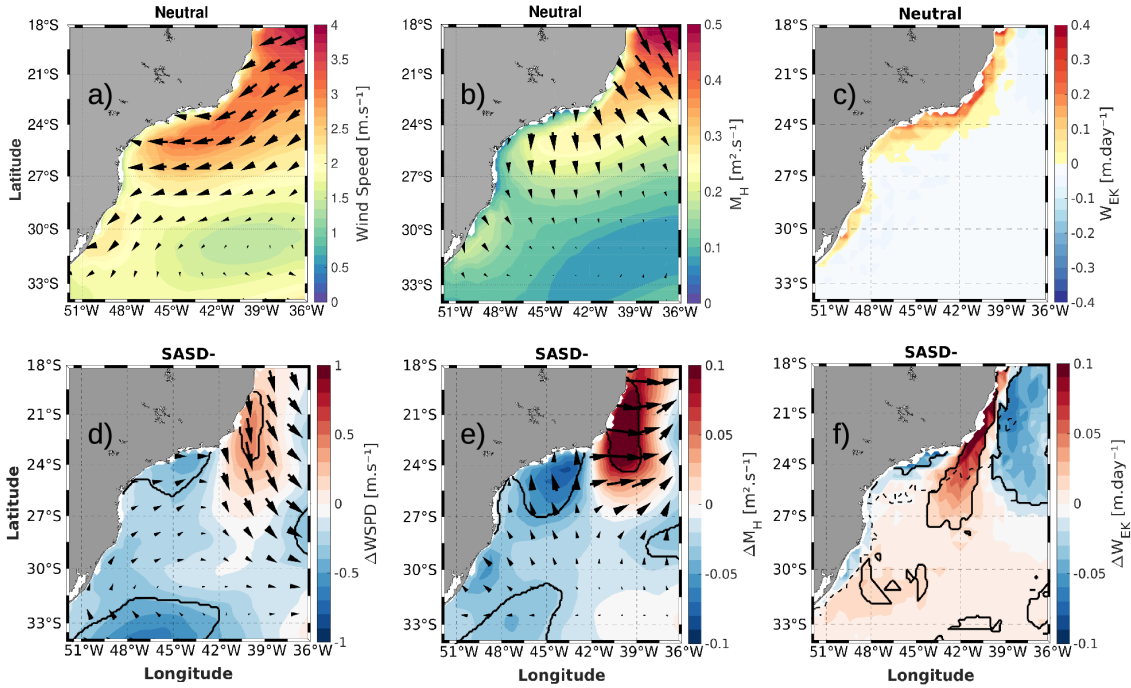


**Fig. 8:** Neutral composites (October-December) of a) the intensity (shading) and direction (vectors) of the wind ( $\text{m.s}^{-1}$ ), b) the intensity (shading) and direction (vectors) of the Ekman transport ( $M_H$ , in  $\text{m}^2.\text{s}^{-1}$ ) and c) the Ekman pumping ( $W_{EK}$ ,  $\text{m}.\text{day}^{-1}$ ) for the southeastern-south Brazilian coast (SBC). The lower figures show the difference between the SASD- and neutral composites of d) intensity (shading) and direction (vectors) of the wind speed ( $\Delta WSPD$ ,  $\text{m.s}^{-1}$ ), e) the intensity (shading) and direction (vectors) of Ekman transport ( $\Delta M_H$ ,  $\text{m}^2.\text{s}^{-1}$ ) and the f) Ekman pumping ( $\Delta W_{EK}$ ,  $\text{m}.\text{day}^{-1}$ ). The solid black lines in the lower figures indicate the regions with significant differences for the 80% confidence interval. In f) the dashed contour line show the position in c) where  $W_{EK} = 0$ .

In a counterintuitive way, in the SAC north of  $24^\circ\text{S}$  (including the region of CFB section) we can see an wind speed intensification (Fig. 8d) during SASD- events. In this area, the statistically significant differences have an average of  $0.38 \pm 0.05 \text{ m.s}^{-1}$ . The changes in wind speeds calculated in this area can reach 17% and are responsible for the changes observed in  $M_H$  and  $W_{EK}$  in Figs. 8e-f, respectively. On average, the offshore Ekman transport increases significantly by about  $0.1 \pm 0.02 \text{ m}^2.\text{s}^{-1}$ , which results in an average increase of

approximately 30% in transport, with some points with differences of 47%. The divergence generated by the wind anomalies at the site drives the positive vertical velocities anomalies in the coast. The combined action between the  $M_H$  and  $W_{EK}$  amplification, the main mechanisms responsible for the upwelling dynamics in the region (Aguilar *et al.*, 2014), is possibly leading to an intensification of coastal upwelling around CFB. During the SASD- vertical velocities are strongly intensified within the area already naturally coastal upwelling favorable (Fig. 8f). About a third of the area with significant differences has, at least, doubled its speed during the spring/summer of the development of the climatic mode. Regarding the modification of winds, CFB has all the conditions that lead to an intensification of the upwelling process. On the other hand, the surroundings of the CSM region do not show any statistically significant difference (Fig. 8a and 8b).

If there is upwelling favorable wind anomalies in the CFB region, the same cannot be said about the NHF. During SASD- there is an intense increase in the heat flux from the atmosphere to the ocean, with the maximum significant differences located in front of the CFB region (Fig. 9b). Morioka *et al.* (2011) show that the positive anomalies (northeastern pole) of the latent heat flux during the growth of SASD- extend over a larger area than the negative anomalies (in the same northeastern pole) during SASD+. Knowing this, it was expected to find high values of NHF anomalies. However, it is likely that the significant differences in the surroundings of the CFB region are related to the intensification of the upwelling process, which ends up bringing cooler waters to the vicinity of the surface, potentiating the flow of heat from the atmosphere to the ocean. The differences can reach the value of  $21 \text{ W.m}^{-2}$ , intensifying the

NHF from the atmosphere to the ocean around 50%. Positive anomalies spread across the Brazilian continental shelf. However, to the continental shelf south of the intense anomalous CFB region, no other location shows significant differences during the period of the compositions. Corroborating the presented so far in this paper, Goes *et al.* (2019) identified negative anomalies in surface and subsurface temperatures near the coast of the CFB region during the summer of 2009/2010, the period of occurrence of SASD-, evidencing the process discussed earlier.

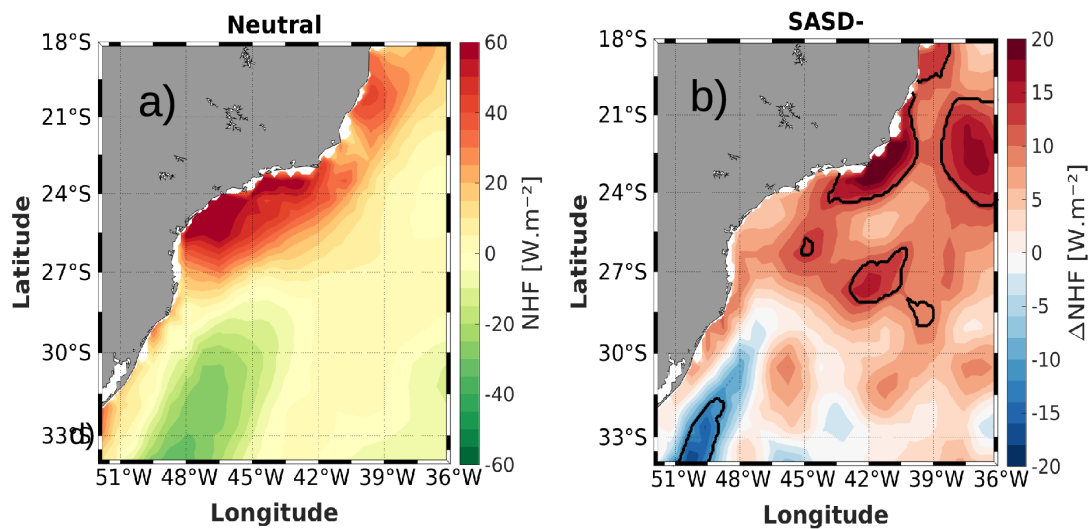


**Fig. 9:** a) Neutral years composite (October-December) of the net heat flux (NHF, in  $W.m^{-2}$ ) and b) SASD- anomalies composite of the NHF ( $\Delta NHF$ , in  $W.m^{-2}$ ) in the southeastern-south Brazilian coast (SBC). Positive values in a) indicate a NHF from the atmosphere to the ocean. The solid black lines indicate the regions with significant differences for the 80% confidence interval.

Looking at the results presented above, it is not clear how the variability in the concentration of chla-a would respond to the ocean-atmosphere changes resulting from SASD-. In CFB there is an intense collaboration of the wind, intensifying the Ekman dynamics, but an intense increase in the NHF, which would hinder the development of phytoplankton due to the increase in stratification. In the CSM region, anomalies in the speed and direction of the wind and the NHF act in an unfavorable way to the coastal upwelling process.

However, they do not have significant anomalies in the region. This type of difference in the performance of climatic modes was observed by Jing *et al.* (2011) in the South China Sea, which show how during the same phase the ENSO can intensify the upwelling dynamics in certain regions and weaken in others through wind anomalies.

In Fig. 10 we show the time series of the composite of  $W_{EK}$ , parameter  $\Phi$  and concentration of chl-a in the regions of CFB and CSM. The positive  $W_{EK}$  anomalies at CFB (Fig. 10c) begin in July, reaching a peak during October and continuing until January. These differences show a strong intensification of vertical velocities during the spring and early summer, causing during the SASD- that the peak of vertical velocities is reached in December (figure not show), that is, with a month in advance with respect to neutral years. Using equation 5, we can see that, as the variation of parameter  $\Phi$  shows during the evolution period of SASD- (Fig. 10c), the addition of NHF to the oceans is more important than the increase in the speed of local winds, resulting in an intensification of vertical stratification in the region. The maximum differences (October-December) increase the stratification parameter  $\Phi$  by approximately  $13 \text{ J.m}^{-3}$ , which seems to be sufficient to weaken the development of phytoplankton organisms. The result of this interaction, then, is expressed in the variability of the concentration of chl-a (Fig. 10c). From July to September chl-a has negative differences in relation to neutral years, since the environment is under positive parameter  $\Phi$  anomalies and the differences in  $W_{EK}$  have not acted long enough. With the arrival of the month of October, the differences in vertical velocities are maximum and, even with the high local stratification, it is possible to observe a peak of positive chl-a anomalies (0.03

mg.m<sup>-3</sup>). Indeed, this peak of anomaly is lower than the peak observed in the SASD+ series (0.07 mg.m<sup>-3</sup>, Fig. 3c), however it is worth noting that this result expresses the importance of the differences in SASD intensities between its phases and even the variation in intensity between the same phase.

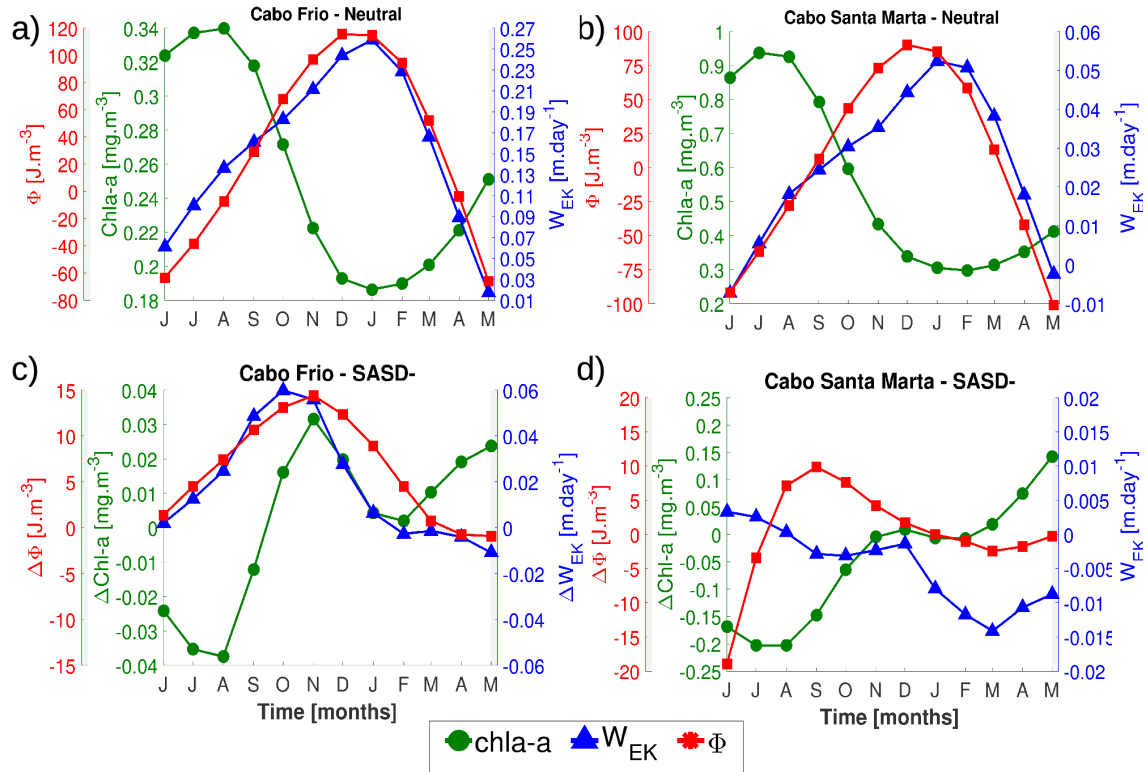


**Fig. 10:** a) Cabo Frio (CFB) and b) Cabo Santa Marta (CSM) time series of the neutral composites of the chlorophyll-a (chl-a, green line, in mg.m<sup>-3</sup>), Ekman pumping (WEK, blue line, in m.day<sup>-1</sup>) and stratification parameter  $\Phi$  calculated according to equation 5 of the text ( $\Phi$ , red line, in J.m<sup>-3</sup>). In c) and d) the time of the SASD- anomalies composite of the same variables ( $\Delta$ chl-a,  $\Delta$ WEK,  $\Delta\Phi$ ) as a) and b). The time series were smoothed with a 3-month moving average filter.

In the vertical section shown in Fig. 11b we can see the composite anomalies of SASD-. In it we can see that, even with the increase in temperature linked to the increase in NHF, there are regions where the differences are negative. These negative anomalies are the result of the incursion of cold waters, induced by the intensification of Ekman pumping, which move towards the surface. The negative differences of each year of occurrence of SASD- (not shown) in the region of platform break (~120 km from

the coast) are observed in all SASD- events. But two specific events are responsible for the negative temperature anomalies closest to the surface (~50 km from the coast): the events of 2002/2003 and 2009/2010. During these periods, the most intense SASD- events occur within the studied time interval, according to SASDI. During these years, the 18 °C isotherm reaches depths around 25 m (not shown), which corroborates the results presented previously and the anomalous resurgence found by Goes *et al.* (2019). In the other years, the isotherm is restricted to 50 m depth.

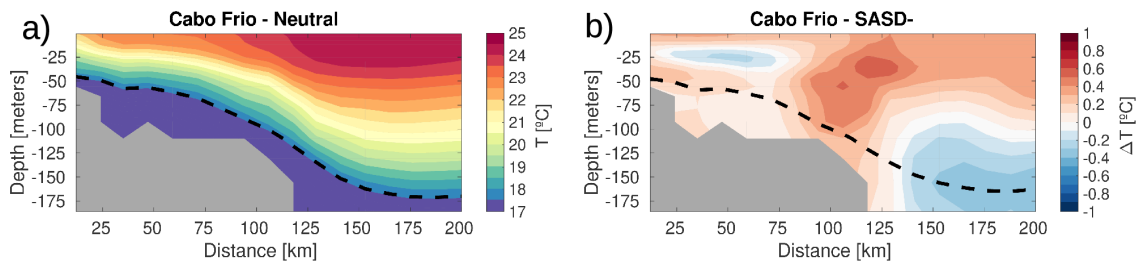


**Fig. 11:** Vertical section of a) the neutral years composite (December-February) and b) the SASD- anomalies composite of the water column temperature ( $T$ , in °C) at Cabo Frio (CFB). The dashed line show the 18 °C isotherm (SACW <18°C) of a) the neutral years composite and b) the SASD- events composite.

The Fig. 10d shows the variability of  $W_{EK}$ ,  $\Phi$  and chl-a in the CSM throughout the development of SASD-. As we saw in Figs. 8 and 9, the CSM region has its winds weakened and the NHF is intensified during the peak action of SASD-. This set reflects the increase in stratification observed through the variation of the stratification parameter  $\Phi$  in Fig. 8c. During August there is a reduction in the vertical turbulent mixing process ( $\Phi < 0$  and  $\Delta\Phi > 0$ ), followed by an intensification of the stratification ( $\Phi > 0$  and  $\Delta\Phi > 0$ ) until November, reaching the maximum value of  $\sim 10 \text{ J}\cdot\text{m}^{-3}$  in September. This fact alone would be enough to hinder the development of photosynthetic organisms at CSM. The region is far from weakened southeast trade winds and also away from intensified westerlies. So that the peak of negative  $W_{EK}$  anomalies occurs during



March, when it was expected to be observed close to the period of the atmospheric peak of SASD- (Sterl and Hazeleger, 2003; Morioka *et al.*, 2011). As a result, it is possible that other factors not addressed here that affect the ocean in the CSM, such as the large rivers discharge (Piola *et al.*, 2005; Möller *et al.*, 2008; Palma *et al.*, 2008) and the proximity to the Brazil-Malvinas Confluence (Garcia *et al.*, 2004) have a greater importance in the chla-a variability seen in the result expressed in Fig. 10d. Unlike the vertical sections previously observed (Fig. 6, 7 and 11), there is not an 18 ° C isotherm shift in the CSM region during the SASD- (Fig. 12b), as expected based on the results previously described. There is a generally heating of the entire section, expected in view of the increase in the local heat flux from the atmosphere to the ocean. Positive anomalies are intensified on the continental shelf, an area of important dynamics for upwelling processes due to friction with the bottom (Campos *et al.*, 2013) and results in a slightly deepening of the 18° C isotherm.

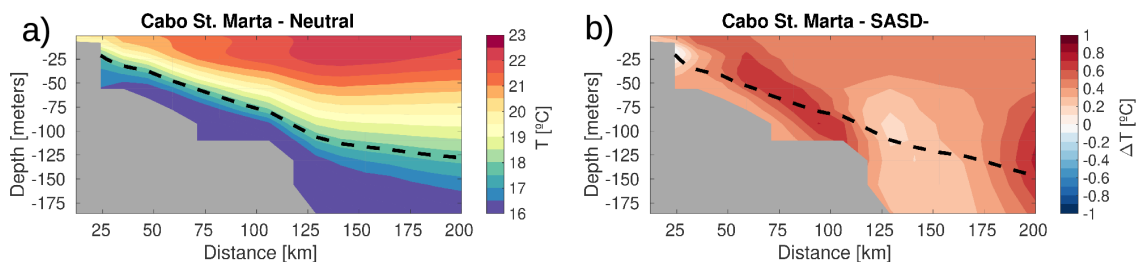


**Fig. 12:** Vertical section of a) the neutral years composite (December-February) and b) the SASD- anomalies composite of the water column temperature (T, in °C) at Cabo Santa Marta (CSM). The dashed line show the 18 °C isotherm (SACW <18°C) of a) the neutral years composite and b) the SASD- events composite.

### 3.2 Southwestern African Coast

The SAC results are described below. As in chapter 3.1, we evaluated the spatial distribution of changes in the wind pattern, the result of Ekman dynamics variability, the distribution in the water column of temperature



anomalies, in addition to the temporal variation of the stratification parameter  $\Phi$  and of chl-a throughout the development of the SASD.

### 3.2.1 Positive SASD

The southeast trade winds and Ekman dynamics on the Benguela Upwelling System (BUS) is highlighted in Fig. 13. As well described by other authors (Shannon and Nelson, 1996; Fennel, 1999), the wind pattern blows parallel to the coast (Fig. 13a), causing coastal offshore Ekman transport (Fig. 13b), resulting in positive vertical velocities close to the shore (Fig. 13c). The spatial distribution of wind speed anomalies, generated during the months of October-December under the influence of SASD+, interact with the northern BUS (north of 27°S) in an opposite way to the southern BUS (south of 27°S) (Fig. 13d). North of 27°S, in front of the Namibia coast from where we obtained the section of the Cape Frio region (CFN in Fig. 1c), there is an intense increase in wind speeds (on average  $0.5 \pm 0.1 \text{ m.s}^{-1}$ ), with significant anomalies (CI = 80%) reaching  $\sim 0.8 \text{ m.s}^{-1}$ . The anomalies can generate winds with speeds above  $8 \text{ m.s}^{-1}$ . This wind speed is more intense than the anomalous winds caused by El-Niño in the South China Sea coast (Jing *et al.*, 2011) and less intense than the anomalous winds generated in the India south coast by the negative Indian Ocean Dipole event (Sankar *et al.*, 2019). As expected, the intensification of southeastern trade winds (result of positive anomalies in the high pressure center over the SAO) enhances neutral years coastal upwelling. As a consequence of the increase in trade wind speeds, offshore Ekman transport also increases (Fig. 13e). Estimates show that offshore transport is intensified by about  $0.2 \pm 0.07 \text{ m}^2.\text{s}^{-1}$ , which represents an increase of  $\sim 17 \pm 0.4\%$

in water removal to offshore. This factors increases the divergence in the vicinity in the northern SAC, which intensifies the vertical velocities of seawater to the surface through Ekman pumping (Fig. 13f). This intensification can induce the rise of a larger volume of cold and nutrient-rich waters, which in turn can enhance the development of phytoplankton organisms. The averaged values of the significant wind speed positive anomalies are similar in the SAC ( $\sim 0.5 \pm 0.1 \text{ m.s}^{-1}$ ) and SBC ( $\sim 0.4 \pm 0.05 \text{ m.s}^{-1}$ ) during SASD+ and SASD- respectively. However, the southeast trade winds blowing in the SAC are almost twice as intense as the northeast winds in the SBC, which cause a proportionality less intense changes in SAC.

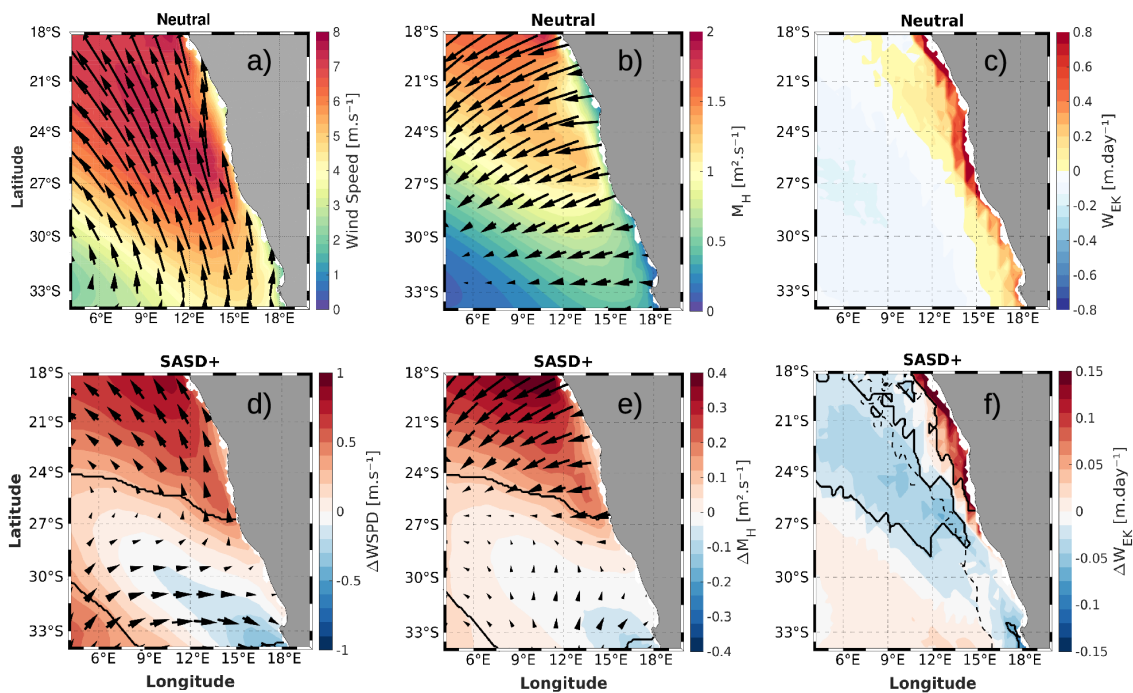


**Fig. 13:** Neutral composites (October-December) of a) the intensity (shading) and direction (vectors) of the wind ( $\text{m.s}^{-1}$ ), b) the intensity (shading) and direction (vectors) of the Ekman transport ( $M_H$ , in  $\text{m}^2.\text{s}^{-1}$ ) and c) the Ekman pumping ( $W_{EK}$ ,  $\text{m.day}^{-1}$ ) for the southwestern African coast (SAC). The lower figures show the difference between the SASD+ and neutral composites of d) intensity (shading) and direction (vectors) of the wind speed ( $\Delta WSPD$ ,  $\text{m.s}^{-1}$ ), e) the intensity (shading) and direction (vectors) of Ekman transport ( $\Delta M_H$ ,  $\text{m}^2.\text{s}^{-1}$ ) and the f) Ekman pumping ( $\Delta W_{EK}$ ,  $\text{m.day}^{-1}$ ). The solid black lines in the lower figures indicate the regions with significant differences for the 80% confidence interval. In f) the dashed contour line show the position in c) where  $W_{EK} = 0$ .

The effects in the southern part of the BUS (south of 27°S) during SASD+ are not the same as those observed for the northern portion (Fig. 13d). Wind speed anomalies gradually decrease towards the south, until they pass to negative values after 30°S. In this area there is a seasonal variability of the wind, so that the southeast winds, favorable to the local coastal upwelling processes during the austral summer, change to west/northwest winds during the winter due to the passage of cyclonic systems (Andrews and Hutchings, 1980). The anomalies observed in Figs. 13d-f indicate a weakening of the upwelling favorable wind in the southern SAC during the SASD+ events, which weakens the offshore Ekman transport leading to reduction of positive Ekman pumping near coast.

The composite of the neutral years of the NHF and the anomalies composites during the SASD+ events are shown in Figs. 14a and 14b, respectively. Positive NHF values indicate a NHF from the atmosphere to the ocean, facilitating the strengthening of the water column vertical stratification (Simpson and Sharples, 2012b). The negative NHF anomalies observed in Fig. 14b indicate a decrease in NHF from the atmosphere to the ocean. This reduction is more intense far from the coast, where the intensification of the near surface wind play a dominant role inducing the latent heat flux anomalies from the ocean to the atmosphere (e.g. Fauchereau *et al.*, 2003). Few places near the coast have significant anomalies. Northern SAC, in surrounding CFN, the differences are around  $-8 \text{ W.m}^{-2}$ . In the vicinity of Santa SHB, the NHF anomalies can pass  $-15 \text{ W.m}^{-2}$ . The NHF negative anomalies and wind speed positive anomalies in the northern SAC deepen the mixed layer, leading to a

unfavorable condition to shortwave radiation heating (Morioka *et al.*, 2011), which may reduce vertical thermal stratification consequently.

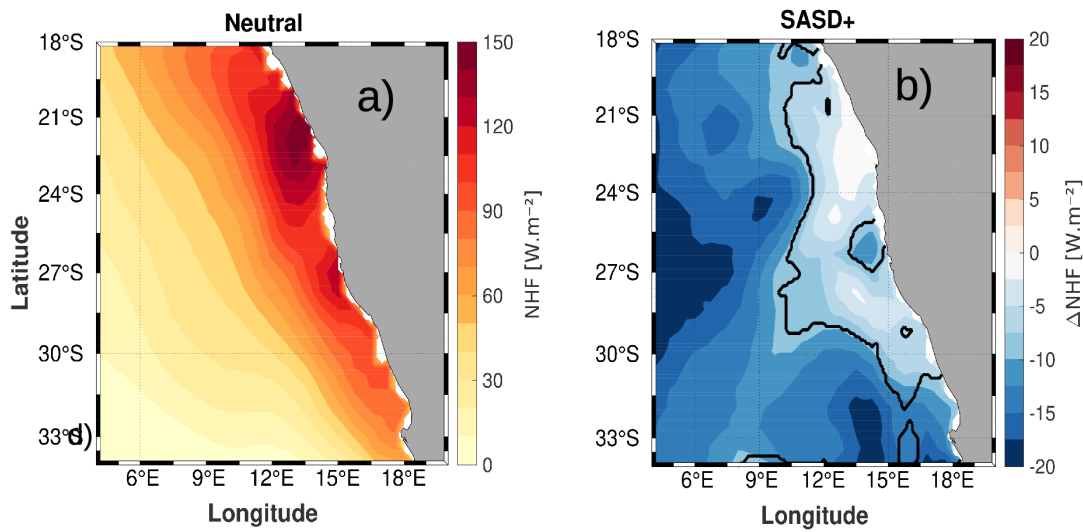


**Fig. 14:** a) Neutral years composite (October-December) of the net heat flux (NHF, in  $W.m^{-2}$ ) and b) SASD+ anomalies composite of the NHF ( $\Delta NHF$ , in  $W.m^{-2}$ ) in the southwestern African coast (SAC). Positive values in a) indicate a NHF from the atmosphere to the ocean.

The results discussed above, about the wind speed and NHF anomalies, also can be seen in the time series of composites anomalies of the Ekman pumping and the stratification parameter  $\Phi$  at the CFN ( $\sim 18^{\circ}S$ ) and SHB ( $\sim 32^{\circ}S$ ) (Fig. 15c and 15d). Figs. 15a-b illustrate the annual Ekman pumping cycle throughout neutral years, already extensively documented (Andrews and Hutchings, 1980; Shannon and Nelson, 1996; Fennel, 1999), which reaches the peak of positive vertical velocities during the austral winter (summer) period in the northern (southern) BUS. Whether in CFN or SHB the stratification parameter  $\Phi$  follows the seasonal variability of the solar radiation, with a peak of maximum (minimum) stratification in summer (winter). In the CFN, the time series of the composite of the neutral years does not reach negative values during the winter (Fig. 15a), unlike what occurs in winter in the SHB. The annual variability of the surface chl-a concentration is linked to water column stabilization (e.g. Riley, 1942; Sverdrup, 1953). During the austral winter, the

northern BUS is under the influence of the maximum wind speeds, while in the southern region there are intense storms passing by. The intense process of wind-induced turbulent mixing, along with the reduced light incidence during winter, limit the development of large concentrations of phytoplankton organisms. The reduction in turbulence and the increase in light incidence during spring/summer lead the peak of chla-a seen in Figs. 15a-b (Pitcher and Nelson, 2006; Hutchings *et al.*, 2012).

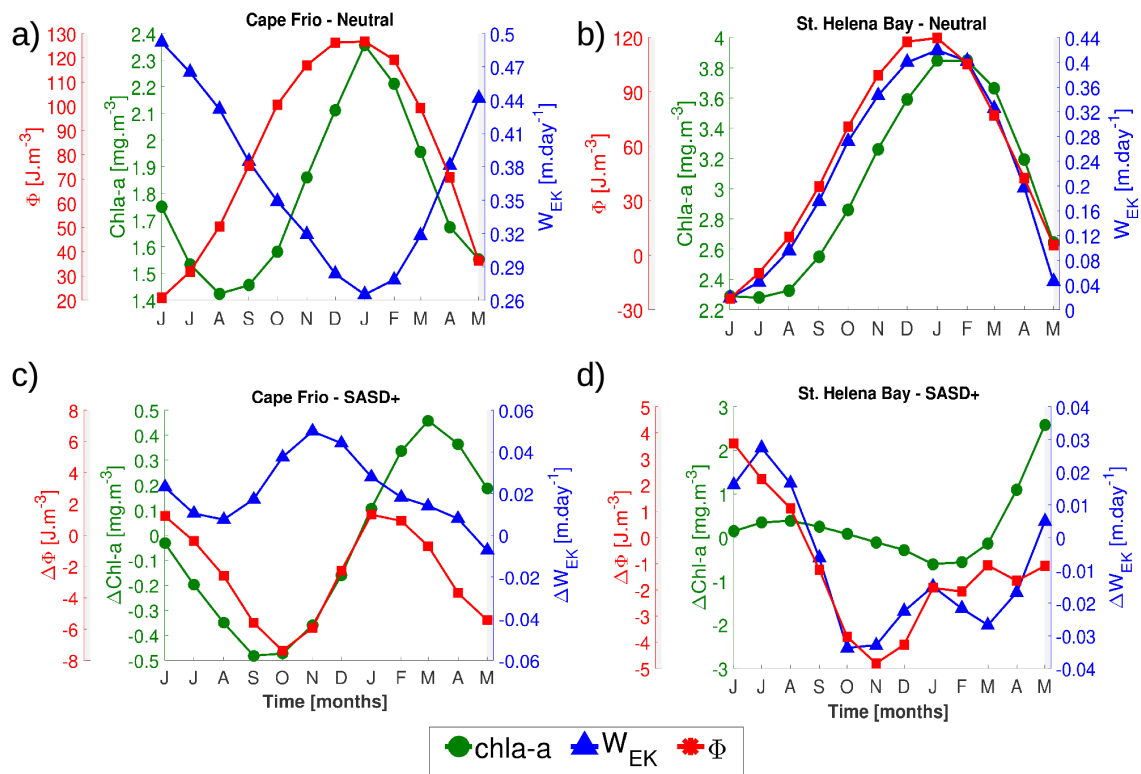


**Fig. 15:** a) Cape Frio (CFN) and b) St. Helena Bay (SHB) time series of the neutral composites of the chlorophyll-a (chla-a, green line, in  $\text{mg}\cdot\text{m}^{-3}$ ), Ekman pumping ( $W_{EK}$ , blue line, in  $\text{m}\cdot\text{day}^{-1}$ ) and stratification parameter  $\Phi$  calculated according to equation 5 of the text ( $\Phi$ , red line, in  $\text{J}\cdot\text{m}^{-3}$ ). In c) and d) the time of the SASD+ anomalies composite of the same variables ( $\Delta\text{chl-a}$ ,  $\Delta W_{EK}$ ,  $\Delta\Phi$ ) as a) and b). The time series were smoothed with a 3-month moving average filter.

Throughout the SASD+ atmospheric changes, the ocean dynamics and the chla-a concentration in the CFN region of Namibia are profoundly modified (Fig. 15c). With the exception of May,  $W_{EK}$  is under the influence of positive anomalies along the time series. The peak period (October-December) coinciding with the maximum intensity anomalies seen in Fig. 13d. The wind

speed intensification combined with the weakened NHF should lead to the stratification parameter  $\Phi$  negative anomalies. And that is exactly what we can see in July-December in Fig. 15c. Unlike what is observed during SASD+ events in the SBC, specifically at CFB, (Fig. 5c), this dynamic does not directly result in chl-a positive anomalies. On the contrary, during the maximum anomalies in the Ekman pumping and the minimum in the stratification, chl-a negative anomalies are observed, reaching values of approximately  $-0.5 \text{ mg.m}^{-3}$ . The wind speed increase hinders the development of phytoplanktonic organisms during spring/summer by increasing turbulent mixing, but possibly providing an increase in nutrients to the photic zone by increasing Ekman pumping. In this way, when wind anomalies start to decrease after the peak of SASD+ the water column becomes more stable, allowing phytoplankton to consume the extra nutrients available, which in turn generates peak of chl-a positive anomalies during the austral summer/spring referred to in Fig. 15c. This four-month lag that can be seen between the peak of the  $W_{EK}$  and the chl-a in CFN in Namibia, but does not exist in the CFB in Brazil, can be explained by the difference in the wind speed of the two regions. We can see in the composites of the neutral years (Figs. 5a and 13a) that the typical speeds around CFB in Brazil and around CFN in Namibia are approximately 3 and 7  $\text{m.s}^{-1}$  respectively. Even if equal positive anomalies during the SASD+ events reach these two locations, the anomalous wind-induced turbulent mixing in the CFN will be greater than the anomalous in CFB. Elsberry and Raney (1978) propose a numerical index that represents the wind-induced vertical turbulent mixing, which helps us to understand the lag between the  $W_{EK}$  peak and the chl-a peak anomalies observed in the CFN region (Fig. 15c). This index is calculated

by the third power of wind speed. Thus, for wind speeds during the neutral years of CFB in Brazil ( $3 \text{ m}\cdot\text{s}^{-1}$ ) and CFN in Namibia ( $7 \text{ m}\cdot\text{s}^{-1}$ ) we would have a mixing index of  $27 \text{ m}^3\cdot\text{s}^{-3}$  and  $343 \text{ m}^3\cdot\text{s}^{-3}$  respectively. If we consider wind speed anomalies of  $0.5 \text{ m}\cdot\text{s}^{-1}$  in the two regions (approximately the averages of the calculated anomalies previously described), that would increase the CFB (now with a wind speed of  $3.5 \text{ m}\cdot\text{s}^{-1}$ ) turbulent mixing index from  $27 \text{ m}^3\cdot\text{s}^{-3}$  to  $42.9 \text{ m}^3\cdot\text{s}^{-3}$ , a index anomaly of  $15.9 \text{ m}^3\cdot\text{s}^{-3}$ . While in the CFN (now with wind speeds of  $7.5 \text{ m}\cdot\text{s}^{-1}$ ) would increase the turbulent mixing index from  $343 \text{ m}^3\cdot\text{s}^{-3}$  to  $421.9 \text{ m}^3\cdot\text{s}^{-3}$ , an anomaly of  $78.9 \text{ m}^3\cdot\text{s}^{-3}$ , which is equivalent to almost five times the CFB anomaly.

In addition to the response to SASD+ in the surface chla-a concentration seen in Fig. 15c, the anomalies composite (Fig. 16b) shows that there is temperature negative anomalies (Fig. 16b), throughout the water column in the CFN, in relation to the neutral composite (Fig. 16a). Two changes that may be affecting the water column temperature in the region have already been discussed: NHF negative anomalies and the intensification of coastal upwelling processes. The influence of the enhanced upwelling can also be observed when we look at the  $16 \text{ }^\circ\text{C}$  isotherm (indicated by the dashed line in Figs. 16A-b), the upper limit of SACW in the northern BUS (Duncombe Rae, 2005). It is possible to see the  $16 \text{ }^\circ\text{C}$  isotherm outcrop to the surface, also a characteristic of the SAC upwelling. However, a third element may also be contributing to the water column temperature negative anomalies, which may even be responsible for the most intense negative anomalies near the coast. The Angola-Benguela front ( $\sim 10^\circ\text{S}$  to  $18^\circ\text{S}$ ), responsible for the transport of the tropical warm waters from the Angola Gyre to the BUS, has its position modulated, in part, by the

intensity of the winds (Meeuwis and Lutjeharms, 1990; Rouault *et al.*, 2007). As we have seen, there is an intensification of the southeast trade winds during the SASD+ events. These anomalous winds may make tropical water difficult to flow southwards during the spring/summer, corroborating with the column water temperature negative anomalies seen in Fig. 16b.

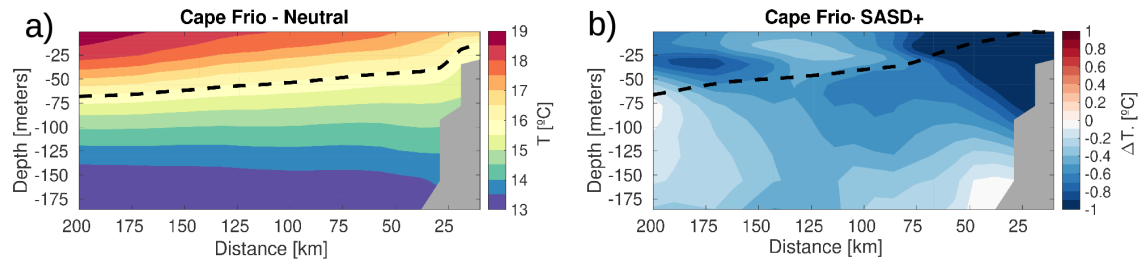


**Fig. 16:** Vertical section of a) the neutral years composite (December-February) and b) the SASD+ anomalies composite of the water column temperature ( $T$ , in  $^{\circ}\text{C}$ ) at Cape Frio (CFN). The dashed line show the  $16^{\circ}\text{C}$  isotherm (SACW  $< 16^{\circ}\text{C}$ ) of a) the neutral years composite and b) the SASD+ events composite.

In Figs. 13d-f it is possible to see that during the SASD+ the SHB region is under the influence of negative anomalies of wind speed,  $M_H$  and  $W_{EK}$ , while Fig. 14b shows that the NHF anomalies are also negative for the region. The Fig. 15d shows the anomalies of the stratification parameter  $\Phi$ , the  $W_{EK}$  and the surface chl-a concentrations. In this figure it is possible to observe the extensive period of Ekman pumping weakening that starts in September and lasts until the April. The same pattern is observed for stratification parameter  $\Phi$ . The peaks of maximum differences observed for the Ekman pumping and the stratification parameter  $\Phi$  occur during the austral spring/summer. The combination of these factors, initially, results in chl-a negative anomalies in January and February similar to those observed during the spring in CFN ( $\sim -0.5 \text{ mg}\cdot\text{m}^{-3}$ ). However, with the arrival of the season of fall and winter, starting in April, the climatological condition of the local wind intensely reduces the upwelling favorable winds, even being able, in certain periods, to cause



downwelling in the southern BUS (Andrews and Hutchings, 1980). During this period, onshore transport works by trapping phytoplankton organisms in regions very close to the coast, substantially increasing the surface chl-a concentration. The unfavorable offshore water transport condition (Fig. 13e) and, consequently, unfavorable offshore phytoplankton transport is intensified with the change from southeast to the west wind regime that happens in the region after the end of the summer. This entrapment of organisms near to the coast is then intensified and possibly results in the major anomalies of chl-a (reaching a maximum of  $\sim +2.5 \text{ mg.m}^{-3}$ ) observed after the summer in SASD+ events. In Figs. 17a-b we illustrate, respectively, the neutral and SASD+ anomalies composites of the water column temperature during the summer, and reinforce the weakening of the upwelling process discussed above. Even with the NHF reduction in the SHB region, temperature positive anomalies can be observed throughout the water column on the continental shelf. In addition, it is worth noting that the  $14^\circ \text{C}$  isotherm, upper limit of the temperature of the Eastern South Atlantic Central Water (ESACW) in the southern BUS (Duncombe Rae, 2005), no longer outcrop to the surface, demonstrating the reduction of the offshore surface water exports.

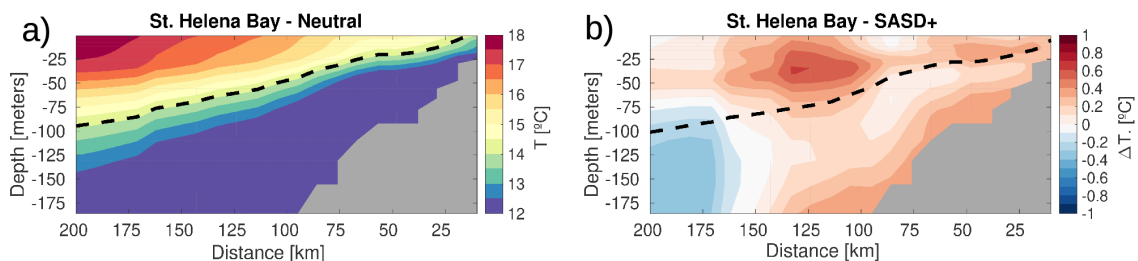


**Fig. 17:** Vertical section of a) the neutral years composite (December-February) and b) the SASD+ anomalies composite of the water column temperature (T, in °C) at St. Helena Bay (SHB). The dashed line show the  $14^\circ \text{C}$  isotherm (ESACW  $< 14^\circ \text{C}$ ) of a) the neutral years composite and b) the SASD+ events composite.

### 3.2.2 Negative SASD

During SASD- events SLP negative anomalies generate anomalous cyclonic winds, which reduces the intensity of the southeast trades. The significant anomalies are far from the coast in almost the entire SAC during SASD- (Fig. 18d).

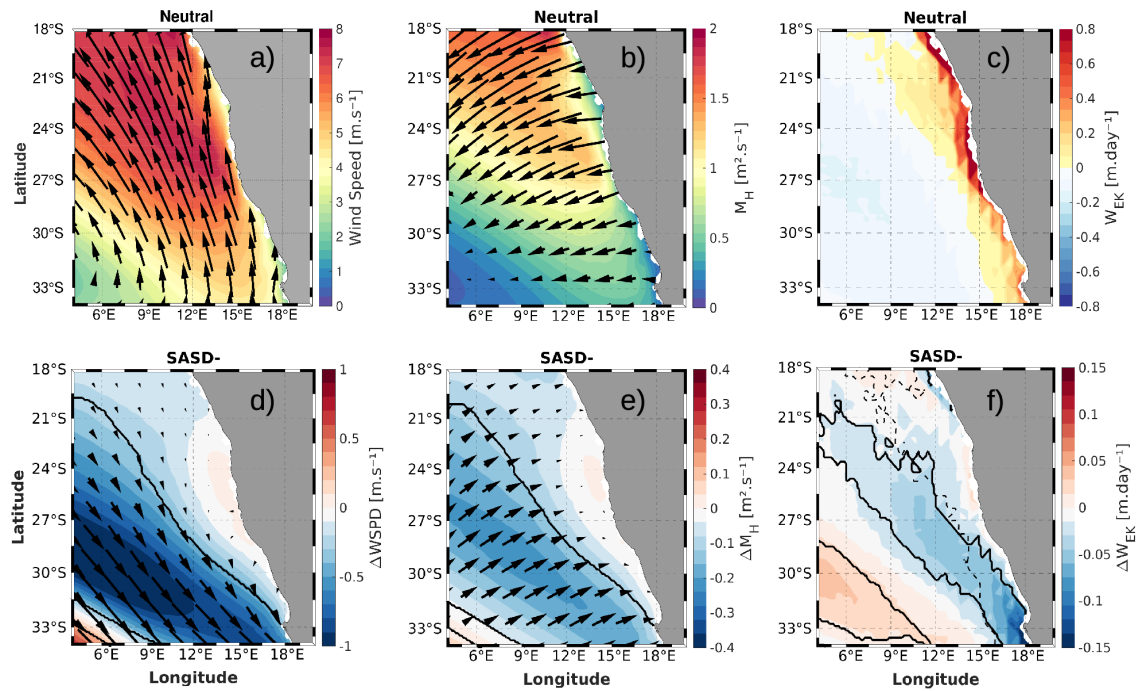


**Fig. 18:** Neutral composites (October-December) of a) the intensity (shading) and direction (vectors) of the wind ( $\text{m}\cdot\text{s}^{-1}$ ), b) the intensity (shading) and direction (vectors) of the Ekman transport ( $M_H$ , in  $\text{m}^2\cdot\text{s}^{-1}$ ) and c) the Ekman pumping ( $W_{EK}$ ,  $\text{m}\cdot\text{day}^{-1}$ ) for the southwestern African coast (SAC). The lower figures show the difference between the SASD- and neutral composites of d) intensity (shading) and direction (vectors) of the wind speed ( $\Delta WSPD$ ,  $\text{m}\cdot\text{s}^{-1}$ ), e) the intensity (shading) and direction (vectors) of Ekman transport ( $\Delta M_H$ ,  $\text{m}^2\cdot\text{s}^{-1}$ ) and the f) Ekman pumping ( $\Delta W_{EK}$ ,  $\text{m}\cdot\text{day}^{-1}$ ). The solid black lines in the lower figures indicate the regions with significant differences for the 80% confidence interval. In f) the dashed contour line show the position in c) where  $W_{EK} = 0$ .

The coastal region between  $23^\circ\text{S}$  and  $28^\circ\text{S}$  has weak positive wind anomalies, however, they are not significant differences ( $CI = 80\%$ ). In some regions over the ocean, wind speed anomalies exceed  $-1 \text{ m}\cdot\text{s}^{-1}$ . The anomalous northwest winds (Fig. 18d) induce anomalies in the  $M_H$  (Fig. 18e) and  $W_{EK}$  (Fig. 18f). The main changes close to the coast are observed in the vicinity of SHB, where the weaker winds reduces offshore Ekman transport and results in a upwelling

unfavorable condition. Ekman pumping negative anomalies up to  $-0.15$  m.day can be observed in front of Cape Columbine ( $\sim 33^{\circ}\text{S}$ ) in South Africa, which can directly affects SHB.

**SASD and the Agulhas rings** – Different from that was observed during SASD+ events, Fig. 19b shows that the anomalies composite of the NHF during SASD- does not have a homogeneous spatial distribution. The NHF was expected to respond to the variability of the latent heat flux generated by the wind and show positive anomalies across the region (Fauchereau *et al.*, 2003; Sterl and Hazeleger, 2003). Nevertheless, statistically significant NHF negative anomalies are observed in front of the coastal region in the southern BUS. Like the wind anomalies, the NHF anomalies can also directly modify the coastal dynamics surrounding SHB. The southern BUS interacts with the rings released by the Agulhas Current retroflection, which introduces warmer and saltier waters in that region (Garzoli and Gordon, 1996; Biastoch *et al.*, 2015; Veitch and Penven, 2017). It is known that the region of release of the Agulhas rings undergoes a meridional displacement related to the zero wind stress curl position, which is linked to the intensity of the westerlies in the south hemisphere (Beal *et al.*, 2011; Durgadoo *et al.*, 2013). According to Sterl and Hazeleger (2003) and Faucherau *et al.* (2003), the SLP anomalies over the South Atlantic Ocean during the SASD years cause a north-south displacement of the southern westerly wind belt. As the rings released by the Agulhas Current retroflection transport relatively warmer waters than those located in the coastal region of the BUS, the latent heat flux from the ocean to the atmosphere is much greater in the waters coming from the Indian Ocean (Villas Bôas *et al.*, 2015). Thus, there is a possible release of a greater number of Agulhas rings

during the SASD- events, probably due to the south displacement of the zero wind stress curl line, which would be responsible for the NHF negative anomalies observed on the south coast of the BUS during SASD- events. However, this relationship between the position of zero wind stress curl line during the SASD and the intensity of the release of Agulhas rings needs to be further studied in order to have more information about this interaction.

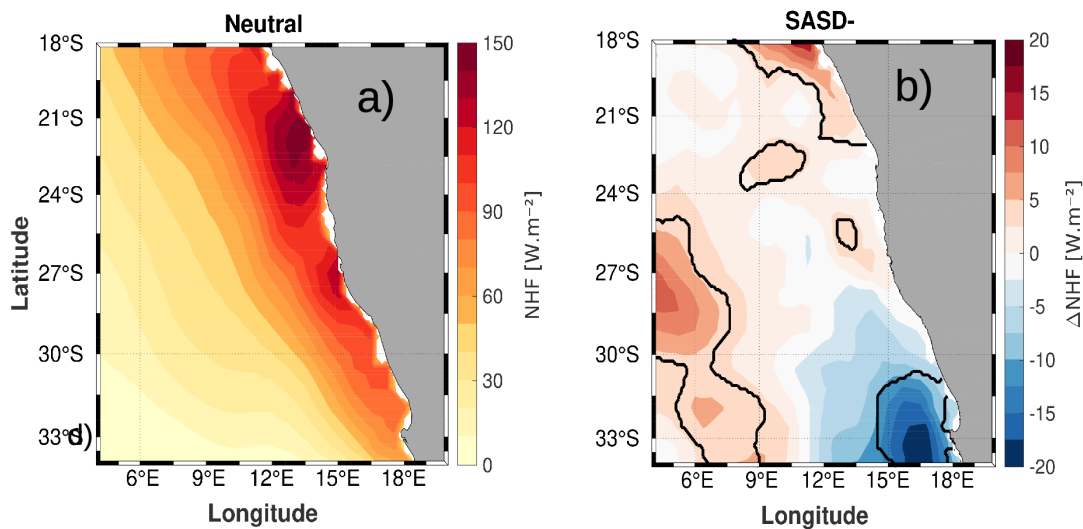


**Fig. 19:** a) Neutral years composite (October-December) of the net heat flux (NHF, in  $W.m^{-2}$ ) and b) SASD- anomalies composite of the NHF ( $\Delta NHF$ , in  $W.m^{-2}$ ) in the southwestern African coast (SAC). Positive values in a) indicate a NHF from the atmosphere to the ocean. The solid black lines indicate the regions with significant differences for the 80% confidence interval.

The changes in the ocean-atmosphere interaction in the CFN and SHB throughout the evolution of SASD- are shown in Figs. 20c-d. As seen in Figs. 18d-f, anomalous northwest winds result in a weakening of Ekman pumping near CFN. This weakening occurs during August-December, reaching a negative peak of  $-0.03 \text{ m.day}^{-1}$  in September and changing to positive values from January. These are weaker and of a shorter duration anomalies than the Ekman pumping positive anomalies observed for the region during SASD+ (Fig. 15c). Together, the reduction in wind speeds and an abnormally positive NHF around CFN (Fig. 19b) act to stabilize the water column resulting in stratification

parameter  $\Phi$  positive anomalies. The reduction in the turbulent mixture generated by the reduction in wind speed has a greater influence over chla-a anomalies during August-December. The environment becomes less turbulent during the period of greatest water column stratification, which allows chla-a positive anomalies that reach up to  $0.4 \text{ mg.m}^{-3}$ . The situation is reversed from mid-summer to mid-fall. The Ekman pumping negative anomalies in the previous months, added to the reduction of stratification during summer/autumn, reduced the concentration of chla-a by  $\sim -0.4 \text{ mg.m}^{-3}$  during February and March in CFN.

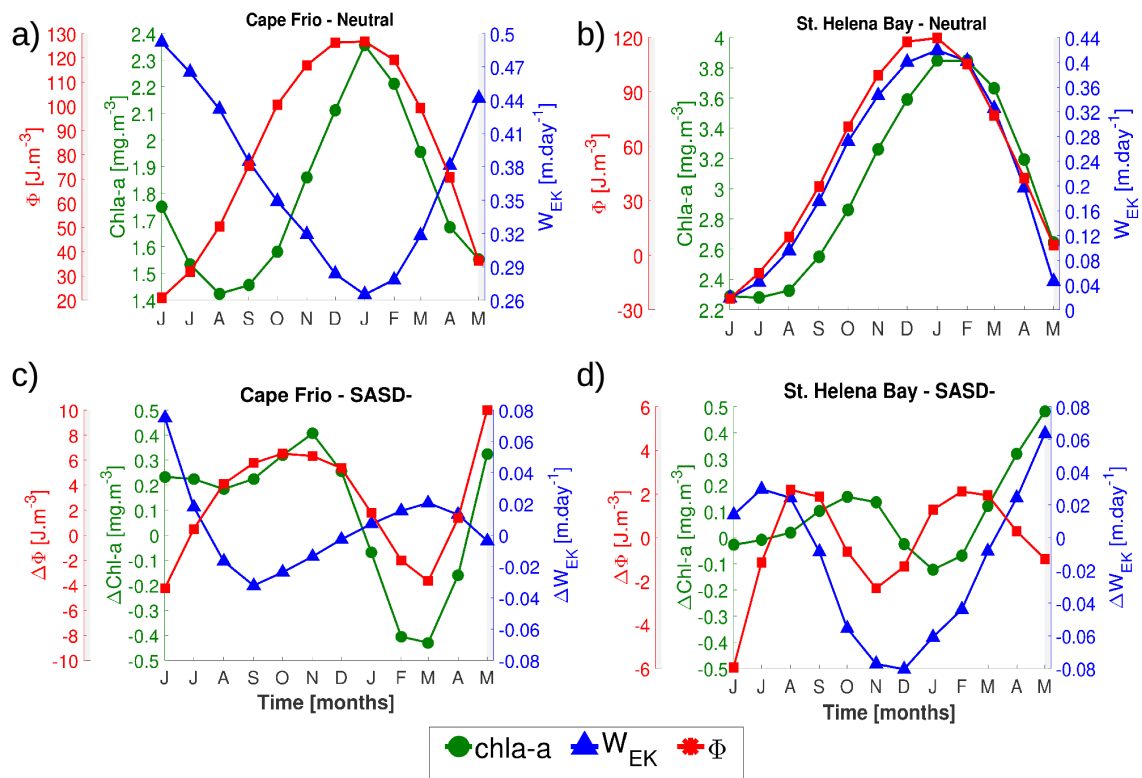


**Fig. 20:** a) Cape Frio (CFN) and b) St. Helena Bay (SHB) time series of the neutral composites of the chlorophyll-a (chla-a, green line, in  $\text{mg.m}^{-3}$ ), Ekman pumping (WEK, blue line, in  $\text{m.day}^{-1}$ ) and stratification parameter  $\Phi$  calculated according to equation 5 of the text ( $\Phi$ , red line, in  $\text{J.m}^{-3}$ ). In c) and d) the time of the SASD- anomalies composite of the same variables ( $\Delta\text{chl-a}$ ,  $\Delta\text{WEK}$ ,  $\Delta\Phi$ ) as a) and b). The time series were smoothed with a 3-month moving average filter.

The increase in stratification can still be seen in the anomalies composites (December-January) of the water column temperature (Fig. 21b).

The increase in the NHF from the atmosphere to the ocean and the anomalous

upwelling unfavorable winds generate intense temperature positive anomalies over continental shelf ( $> 1^{\circ}\text{C}$ ). This leads to a deepening of the  $16^{\circ}\text{C}$  isotherm (upper limit of the SACW) in approximately 50 m. Another process that may contribute to the temperature positive anomalies observed is related to the flow of warm tropical waters from the Angola Basin. During the SASD- events, the weakening of the trade winds may facilitate the intrusion of warm waters over the continental shelf in the northern BUS, just as the intensification of the trade winds appears to hinder this intrusion during the SASD+ events. These processes occurring simultaneously would account for the distribution of the temperature anomalies observed in Fig. 21b.

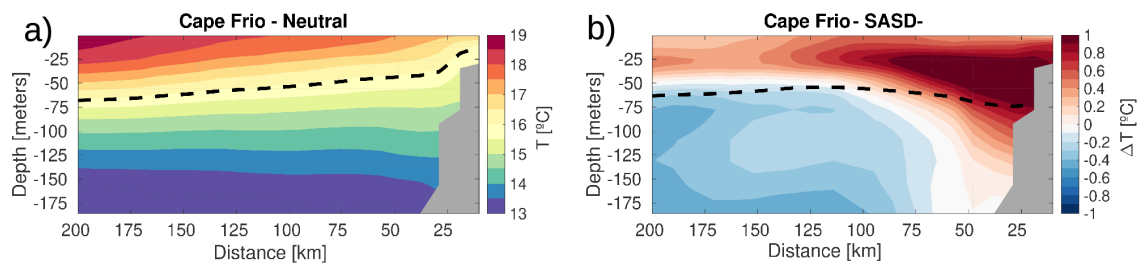


**Fig. 21:** Vertical section of a) the neutral years composite (December-February) and b) the SASD- anomalies composite of the water column temperature ( $T$ , in  $^{\circ}\text{C}$ ) at Cape Frio (CFN). The dashed line show the  $16^{\circ}\text{C}$  isotherm (SACW  $< 16^{\circ}\text{C}$ ) of a) the neutral years composite and b) the SASD- events composite.

The  $W_{\text{EK}}$  negative anomalies in the SHB (Fig. 20d) over the period of action of the SASD- is more intense than that observed for the CFN, with a peak of negative anomalies attaining the value of  $-0.08 \text{ m}\cdot\text{day}^{-1}$ . This represents more than twice the weakness during the SASD+ events (Fig. 15d). The weakening of the winds that reduces Ekman pumping also reduces the local wind-induced turbulent mixing. However, although the Ekman pumping negative anomalies are more intense than those observed in the CFN, the positive anomalies of chl-a do not reach  $0.2 \text{ mg}\cdot\text{m}^{-3}$ . In addition, the intense Ekman pumping weakening, which at most reaches values twice the peak in CFN, does

not subsequently reduce the chl-a concentration with the same intensity. This lack of reduction in chl-a concentrations may be associated with the possible increase in the release Agulhas rings in the southern BUS during October-December, as previously discussed. Through results obtained by modeling Villar *et al.* (2015) show that the rings released by the Agulhas Current retroflection favor the development of photosynthetic organisms due to supply of nutrients to the region. The dispute between the reduction of Ekman pumping and the intrusion of Indian Ocean waters makes the distribution of chl-a anomalies over the period of evolution of the SASD- does not present well-marked fluctuations as can be seen in CFN.

In addition to the action in the chl-a concentrations, the processes cited above also modify the water column temperature in SHB. As can be seen in Fig. 22b, almost the entire water column has temperature positive anomalies, possibly due to the combination of the weakening processes of Ekman pumping and the intrusion of relatively warmer waters from the Agulhas Current. This result in temperature positive anomalies up to 1 °C close to the surface over the continental shelf. In the regions closest to the coast, the 14 °C isotherm does not outcrop to surface, again corroborating the results previously described here of the upwelling unfavorable conditions.

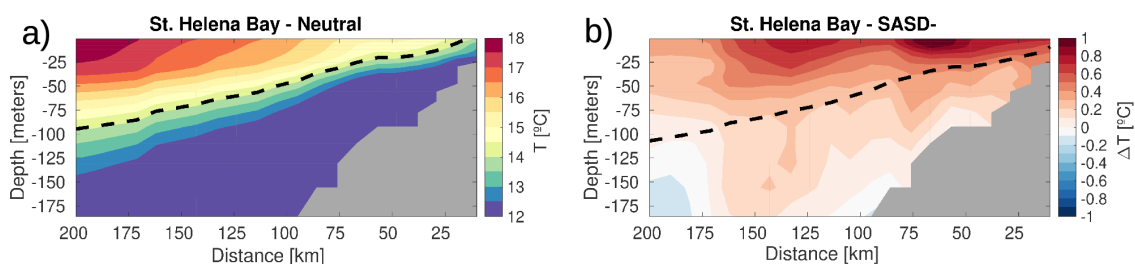


**Fig. 22:** Vertical section of a) the neutral years composite (December-February) and b) the SASD- anomalies composite of the water column temperature ( $T$ , in °C) at St. Helena Bay (SHB). The dashed line show the 14 °C isotherm ( $ESACW < 14$  °C) of a) the neutral years composite and b) the SASD- events composite.



#### 4. CONCLUSIONS

The ocean-atmosphere interactions during SASD events were studied through composites built with ERAI and GLO reanalysis data. Nine SASD events were identified in the range from 1993 to 2018 based in the SASDI calculation (Morioka *et al.*, 2011), with four SASD+ and five SASD- events. In addition to those already observed by previous studies that studied SASD until 2010 (Morioka *et al.*, 2011; Rodrigues *et al.*, 2015), the index also allowed us to identify three other recent events (SASD +: 2011/2012 and 2017/2018; SASD-: 2015/2016). The effects of SASD+ over the main upwelling systems of SBC (CFB and CSM) intensify the vertical velocities related to Ekman pumping and slightly reduce the vertical water column thermal stratification. The enhanced coastal upwelling process in these regions is also marked in the water column temperature, which can be noted by the elevation of the 18°C isotherm (SACW <18°C) closer to the surface than that observed in neutral years. However, in SBC, only in CFB this configuration favors the appearance of chla-a positive anomalies. During the SASD- events, the CFB region is also directly affected. However, instead of observing an expected weakening of the northeast winds due to negative anomalies in the SLP, there is an intensification of these winds. This intensification favors positive velocities related to Ekman pumping, which also favors the appearance of chla-a positive anomalies. This upwelling favorable condition has its potential reduced due to the increase in vertical stratification relative to the increase in NHF from the atmosphere to the ocean. It is makes the chla-a anomalies in CFB during the SASD- less than those observed during the SASD+ events.



In SAC, the influence of the SASD+ events in the coastal region is determined by the variation of latitude. So, to the north of 27°S, there is an intensification of the southeast trade winds and a weakening of the NHF from the atmosphere to the ocean. Together, the wind speed and NHF anomalies leads to an upwelling process enhance, which result in surface chla-a concentration positive anomalies. This anomalies appear with a certain delay of approximately four months, which occurs due to the increase wind-induced turbulent mixing and hinders the development of photosynthetic organisms. The SASD+ can also alter the SAO circulation, preventing tropical warm waters from the Angola Gyre from penetrating over the continental shelf of the northern BUS (north of 27°S). The opposite occurs in this area during SASD- events. The tropical water intrusion can be seen by the high water column temperature positive anomalies over the continental shelf and by the deepening of the 16°C isotherm close to the shore (SACW <16°C). In the southern BUS (south of 27°S) there is a weakening in the removal of water from the coast during SASD+. Consequently, a weakening of the positive vertical velocities induced by the Ekman pumping. Thus, during the SASD+, the region traps phytoplankton organisms closest to the coast, reducing their export to deep ocean regions. It is possible to observe a great increase in the concentration of chla-a in the region around SHB, which occurs due to the aforementioned trapping and the reduction of the wind-induced turbulent mixing. With regard to SASD-, the main point observed in this study is the interaction of the southern portion of the BUS with the Agulhas rings. The latest possibly released in greater numbers due to the poleward displacement of the southern westerlies belt. As a consequence, this migration would cause a displacement to the south

of the position where the wind stress curl over the ocean surface is zero. This modification would facilitate the release of a greater number of Agulhas rings to the SAO. The interaction can be observed through the NHF negative anomalies around the southern BUS. The anomalies are linked to the intense latent heat flux from the ocean to the atmosphere due to the warmest waters of the Indian Ocean carried by the rings.

The regions studied here have several other local processes related to coastal upwelling and which were only superficially addressed in this work. Thus, the relationship between the SASD and the Brazil Current, the SASD and the Angola Gyre and this climate mode and the Agulhas Current need further analysis. With this, it will be possible to complement the results obtained by this study, which will allow a greater understanding of the relationship between the SASD and the SAO coastal upwelling dynamics.

#### ACKNOWLEDGEMENTS

L.H.O. da Silva acknowledges the support from the Coordenação de Aperfeiçoamento de Pessoal de Nível Superior (CAPES) scholarship. The authors thank the European Centre for Medium-Range Weather Forecasts and the Copernicus Marine Environment Monitoring Service for provide open access to available data. L.H.O. da Silva also would like to thank the professor Dr. Paulo Henrique Rezende Calil (Helmholtz-Zentrum Geesthacht) and the friend Dr. Rodrigo Mogollón (Instituto del Mar del Perú) for valuable discussions.

## Capítulo V: Síntese da Discussão e Conclusões

Utilizando o cálculo do IDSAS para o intervalo de 1993 a 2018 foram computados nove anos de ocorrência do DSAS, sendo quatro eventos de DSAS+ (1996/1997, 1998/1999, 2011/2012 e 2017/2018) e cinco eventos DSAS- (1994/1995, 2002/2003, 2004/2005, 2009/2010 e 2015/2016). Os demais períodos são considerados anos neutros. Esses eventos foram utilizados para construir as composições para os determinados eventos e períodos neutros.

A costa brasileira sofre alterações localizadas e pouco intensas durante os períodos de SASD+. Na região costeira próxima a Baía de Santos (entre 23°S e 27°S) e ao norte de CFB (23°S) há enfraquecimento da dinâmica de ressurgência induzida pelo vento durante o período das composições (outubro-dezembro). Entretanto, a série temporal das composições para a região de CFB mostra que existem anomalias positivas no bombeamento de Ekman anteriores a esse período (agosto-outubro), as quais intensificam o processo de ressurgência local. Essas anomalias positivas no bombeamento de Ekman resultam em anomalias positivas na concentração superficial de clorofila-a. Durante o mesmo período a região do CSM também está sob influência de anomalias positivas do bombeamento de Ekman, contudo são mais fracas do que as observadas em CFB e não estão ligadas a uma elevação na concentração de clorofila-a. Em ambas as regiões, as composições da temperatura da coluna de água (dezembro-fevereiro) mostram elevação da isoterma de 18°C, limite superior da Água Central do Atlântico Sul (ACAS), para mais próximo da superfície durante os eventos de DSAS+. Isso corrobora com as anomalias positivas no bombeamento de Ekman, reforçando a ideia de intensificação do processo de ressurgência em ambos os locais durante os anos de DSAS+.

Uma interessante particularidade ocorre na CSB durante os eventos de DSAS-. Na região costeira ao norte de 24°S há forte intensificação na dinâmica atmosférica, com aumento nas velocidades dos ventos de nordeste durante outubro-dezembro. Esse incremento nos ventos favoráveis à ressurgência

levam ao aumento nas velocidades verticais positivas do oceano, as quais são ligadas ao bombeamento de Ekman. A mesma região possui intenso aumento no  $Q_{NET}$  da atmosfera para o oceano, o que leva ao aumento da estratificação vertical da coluna de água nesta região. A série temporal das composições das anomalias de bombeamento de Ekman, parâmetro de estratificação  $\Phi$  e clorofila-a da região de CFB ilustram essas modificações atmosféricas observadas. Durante agosto-janeiro CFB tem grandes anomalias positivas no bombeamento de Ekman e, no mesmo período, intenso aumento na estratificação devido ao forte aumento no  $Q_{NET}$  da atmosfera para o oceano. Mesmo com as velocidades verticais duas vezes maiores nos eventos de DSAS- do que nos eventos de DSAS+, as anomalias positivas na concentração superficial de clorofila-a nos anos de DSAS- alcançam apenas metade do valor observado durante os anos de DSAS+. Isso ocorre devido ao aumento na estratificação vertical relacionado ao aumento no  $Q_{NET}$  anteriormente descrito. As composições da temperatura da coluna de água, tanto em CFB quanto em CSM, apresentam anomalias positivas de temperatura durante os anos de DSAS-. Todavia, o aumento no bombeamento de Ekman observado em CFB está marcado com anomalias negativas de temperatura em parte da plataforma continental e na região de quebra de plataforma.

A influência do DSAS+ na CSA depende diretamente da latitude. Durante o período de outubro-dezembro as velocidades dos ventos alísios são intensificadas em frente a região costeira ao norte de 27°S. Como resultado desta intensificação, há um aumento nas velocidades verticais positivas relativas ao bombeamento de Ekman. Ao sul de 27°S ocorre o oposto. As velocidades do vento na parte sul do SRB enfraquecem, o que leva à redução nas velocidades verticais positivas do oceano. Deste modo, temos ao norte de 27°S amplificação dos processos de ressurgência e enfraquecimento ao sul. As anomalias do  $Q_{NET}$  (outubro-dezembro) são praticamente homogêneas, sendo observadas anomalias negativas em quase toda a área da CSA, o que corrobora com a redução da estratificação vertical. A série temporal das composições das anomalias do bombeamento de Ekman, do parâmetro de estratificação  $\Phi$  e da clorofila-a da região de CFN reafirmam a variabilidade atmosférica supracitada. Entre os meses de setembro e janeiro observa-se

aumento nas velocidades verticais e redução da estratificação vertical. Em conjunto, esses fatores deveriam ser favoráveis ao surgimento de anomalias positivas na concentração superficial de clorofila-a. Porém, o observado é o oposto. Acontece que, na região da CSA, a estabilidade da coluna de água é um importante fator no desenvolvimento de organismos fitoplanctônicos. O aumento observado na velocidade do vento também aumenta a mistura turbulenta vertical induzida por este. Isso reflete em anomalias negativas de clorofila-a de julho a dezembro. Contudo, após o período de pico das anomalias de velocidade do vento e, conseqüentemente, das anomalias de bombeamento de Ekman, há a redução da mistura turbulenta. Deste modo, durante os meses de janeiro a março, uma coluna de água mais estável permite com que os organismos fitoplanctônicos venham a consumir o *input* extra de nutrientes disponibilizados durante o pico de julho a dezembro. A estrutura da composição da temperatura da coluna de água (dezembro-fevereiro) em CFN também indica a intensificação dos processos de ressurgência. Durante o verão austral, após o pico das modificações atmosféricas descritas anteriormente, a isoterma de 16 °C (limite superior da ACAS na região) aflora à superfície sobre a plataforma continental. Este afloramento evidencia a redução na estratificação e impulsionamento do bombeamento de Ekman positivo. As mais intensas anomalias negativas sobre a plataforma também podem ter um terceiro elemento além do bombeamento de Ekman e do  $Q_{NET}$ . A intensificação dos ventos de sudeste também colaboraria para a redução da entrada de águas quentes vindas do Giro da Angola, tornando as águas sobre a plataforma continental em frente a CFN mais frias do que o observado nos anos neutros. Ao sul de 27°S, especificamente na região de SHB o contrário é observado quando nos referimos ao bombeamento de Ekman. A redução da exportação de água para sentido *offshore* é reduzido, bem como o parâmetro de estratificação da coluna de água devido ao  $Q_{NET}$ . Entretanto, devemos lembrar que nessa região há o enfraquecimento dos ventos, o que vem a reduzir a mistura turbulenta induzida pelo vento. De modo que o destaque desta região durante os anos de DSAS+ fica por conta de grandes anomalias positivas na concentração superficial de clorofila-a após o mês de março. Essas anomalias podem estar relacionadas

com a redução do transporte de Ekman *offshore* em conjunto com a redução da turbulência, o que vêm a reter os organismos próximos a região costeira e bem próximos a superfície, o que ampliaria os valores de concentração obtidos através de sensores remotos. Na seção vertical de temperatura da região de SHB é possível observar o resultado da variabilidade do vento na coluna de água, induzindo as anomalias positivas de temperatura devido ao enfraquecimento do processo de ressurgência. O aprofundamento da isoterma de 14 °C (Água Central do Atlântico Sul Leste) é mais um indicador do enfraquecimento do processo de ressurgência costeira na região sul do SRB.

O DSAS- atua reduzindo a intensidade dos ventos de sudeste em quase toda a região da CSA. Com ventos anômalos de noroeste o modo climático resulta em enfraquecimento do bombeamento de Ekman em quase toda a região costeira. Em relação as anomalias no  $Q_{NET}$ , era esperado que o enfraquecimento dos ventos fosse responsável por gerar anomalias positivas do  $Q_{NET}$  por toda região da CSA. Entretanto, ao sul de 27°S são observadas anomalias negativas de  $Q_{NET}$ , possivelmente ligadas à liberação dos Vórtices das Agulhas. Enquanto que na região de CFN as modificações observadas durante a evolução do DSAS- são exatamente opostas as observadas durante o DSAS+ (e.g. aumento da estabilidade da coluna de água levando a anomalias positivas de clorofila-a e enfraquecimento do vento permitindo maior intrusão de águas quentes do Giro da Angola sobre a plataforma), as principais alterações observadas na região sul da CSA (sul de 27°S) durante os anos de DSAS- são associadas à interação entre a região sul do SRB e os Vórtices das Agulhas. As modificações marcantes na dinâmica de interação oceano-atmosfera ocorrem no entorno de SHB. As composições das anomalias de vento mostram enfraquecimento destes ao sul de 27°S, o que leva, assim como nos anos de DSAS+, ao enfraquecimento das velocidades verticais positivas na região. Entretanto, a disposição espacial das anomalias do  $Q_{NET}$  não é homogênea como observamos durante o DSAS+. A distribuição espacial de anomalias positivas do  $Q_{NET}$  da atmosfera para o oceano é quebrada por anomalias negativas em frente a região de SHB, se estendendo ao norte para aproximadamente 27°S. As águas dos Vórtices das Agulhas carregam para o Oceano Atlântico águas relativamente mais quentes vindas do oceano Índico.

Com isso, o fluxo de calor latente do sentido oceano para atmosfera é muito mais intenso do que o observado nas águas frias do SRB. Deste modo, é possível que, durante os eventos de DSAS-, ocorra um deslocamento no sentido do polo Sul da linha do rotacional nulo do estresse do vento. Esse deslocamento faria com que fossem liberados mais vórtices, levando às anomalias negativas de  $Q_{NET}$  observadas na porção sul do SRB durante os eventos de DSAS-.

## Referências Bibliográficas

- Aguiar AL, Cirano M, Pereira J, Marta-Almeida M (2014) Upwelling processes along a western boundary current in the Abrolhos-Campos region of Brazil. *Cont Shelf Res* 85, 42–59. <https://doi.org/10.1016/j.csr.2014.04.013>
- Guimaraens MA, Coutinho R (2000) Temporal and spatial variation of *Ulva* spp. and water properties in the Cabo Frio upwelling region of Brazil. *Aquat Bot* 66, 101–114. [https://doi.org/10.1016/S0304-3770\(99\)00070-4](https://doi.org/10.1016/S0304-3770(99)00070-4)
- Andrews WRH, Hutchings L (1980) Upwelling in the Southern Benguela Current *Prog Oceanogr* 9, 1–81. [https://doi.org/10.1016/0079-6611\(80\)90015-4](https://doi.org/10.1016/0079-6611(80)90015-4)
- Bachèlery M, Illig S, Dadou I (2016) Interannual variability in the South-East Atlantic Ocean, focusing on the Benguela Upwelling System: Remote versus local forcing Marie-Lou. *J Geophys Res Ocean* 121, 284–310. <https://doi.org/10.1002/2015JC011168>
- Bakun A, Nelson CS (1991) The seasonal cycle of wind-stress curl in subtropical eastern boundary current regions. *J Phys Oceanogr* [https://doi.org/10.1175/1520-0485\(1991\)021<1815:TSCOWS>2.0.CO;2](https://doi.org/10.1175/1520-0485(1991)021<1815:TSCOWS>2.0.CO;2)
- Beal LM (2009) A time series of agulhas undercurrent transport. *J Phys Oceanogr* 39, 2436–2450. <https://doi.org/10.1175/2009JPO4195.1>
- Beal LM, De Ruijter WPM, Biastoch A, Zahn R, Cronin M, Hermes J, Lutjeharms J, Quartly G, Tozuka T, Baker-Yeboah S, Bornman T, Cipollini P, Dijkstra H, Hall I, Park W, Peeters F, Penven P, Ridderinkhof H, Zinke J (2011) On the role of the Agulhas system in ocean circulation and climate. *Nat* 472, 429–436. <https://doi.org/10.1038/nature09983>
- Biastoch A, Durgadoo JV, Morrison AK, Van Sebille E, Weijer W, Griffies SM (2015) Atlantic multi-decadal oscillation covaries with Agulhas leakage. *Nat Commun* 6. <https://doi.org/10.1038/ncomms10082>
- Campos EJD, Goncalves JE, Ikeda Y (1995) Water mass characteristics and geostrophic circulation in the South Brazil Bight: summer of 1991. *J Geophys Res* 100. <https://doi.org/10.1029/95jc01724>
- Campos PC, Möller OO, Piola AR, Palma ED (2013) Seasonal variability and coastal upwelling near Cape Santa Marta (Brazil). *J Geophys Res Ocean* 118, 1420–1433. <https://doi.org/10.1002/jgrc.20131>



- Carr ME (2001) Estimation of potential productivity in Eastern Boundary Currents using remote sensing. *Deep Res Part II Top Stud Oceanogr* 49, 59–80. [https://doi.org/10.1016/S0967-0645\(01\)00094-7](https://doi.org/10.1016/S0967-0645(01)00094-7)
- Castelao RM, Barth JA (2006) Upwelling around Cabo Frio, Brazil: The importance of wind stress curl. *Geophys Res Lett* 33, 2–5. <https://doi.org/10.1029/2005GL025182>
- Castelao RM, Campos EJD, Miller JL (2004) A Modelling Study of Coastal Upwelling Driven by Wind and Meanders of the Brazil Current. *J Coast Res* 203, 662–671. [https://doi.org/10.2112/1551-5036\(2004\)20\[662:amsocu\]2.0.co;2](https://doi.org/10.2112/1551-5036(2004)20[662:amsocu]2.0.co;2)
- Castro B, Miranda L (1998) Physical oceanography of the western Atlantic Continental Shelf located between 4°N and 34°S coastal segment (4,W). *sea* 14A, 209–251.
- Chavez FP, Messié M (2009) A comparison of Eastern Boundary Upwelling Ecosystems. *Prog Oceanogr* 83, 80–96. <https://doi.org/10.1016/j.pocean.2009.07.032>
- Chen Z, Yan XH, Jo YH, Jiang L, Jiang Y (2012) A study of Benguela upwelling system using different upwelling indices derived from remotely sensed data. *Cont Shelf Res* 45, 27–33. <https://doi.org/10.1016/j.csr.2012.05.013>
- Coelho-Souza SA, López MS, Guimarães JRD, Coutinho R, Candella RN (2012) Biophysical interactions in the cabo frio upwelling system, Southeastern Brazil. *Braz J Oceanogr* 60, 353–365. <https://doi.org/10.1590/S1679-87592012000300008>
- Cury P, Shannon L (2004) Regime shifts in upwelling ecosystems: Observed changes and possible mechanisms in the northern and southern Benguela. *Prog Oceanogr* 60, 223–243. <https://doi.org/10.1016/j.pocean.2004.02.007>
- Mahiques MM, Bicego MC, Silveira ICA, Sousa SHM, Lourenço RA, Fukumoto MM (2005) Modern sedimentation in the Cabo Frio upwelling system, Southeastern Brazilian shelf. *An Acad Bras Cienc* 77, 535–548. <https://doi.org/10.1590/s0001-37652005000300013>
- Durgadoo JV, Loveday BR, Reason CJC, Penven P, Biastoch A (2013) Agulhas leakage predominantly responds to the southern hemisphere westerlies. *J Phys Oceanogr* 43, 2113–2131. <https://doi.org/10.1175/JPO-D-13-047.1>
- Ekman VW (1905) On the Influence of the Earth's Rotation on Ocean-Currents. *Ark Mat Astr Fys*
- Elsberry RL, Raney SD (1978) Sea Surface Temperature Response to Variation in Atmospheric Wind Forcing.

- Espinoza-Morriberón D, Echevin V, Colas F, Tam J, Ledesma J, Vásquez L, Graco M (2017) Impacts of El Niño events on the Peruvian upwelling system productivity. *J Geophys Res Ocean* 122, 5423–5444. <https://doi.org/10.1002/2016JC012439>
- Fauchereau N, Trzaska S, Richard Y, Roucou P, Camberlin P (2003) Sea-surface temperature co-variability in the southern Atlantic and Indian Oceans and its connections with the atmospheric circulation in the Southern Hemisphere. *Int J Climatol* 23, 663–677. <https://doi.org/10.1002/joc.905>
- Fennel W (1999) Theory of the Benguela upwelling system. *J Phys Oceanogr* 29, 177–190. [https://doi.org/10.1175/1520-0485\(1999\)029<0177:TOTBUS>2.0.CO;2](https://doi.org/10.1175/1520-0485(1999)029<0177:TOTBUS>2.0.CO;2)
- Garcia CAE, Sarma YVB, Mata MM, Garcia VMT (2004) Chlorophyll variability and eddies in the Brazil-Malvinas Confluence region. *Deep Res Part II Top Stud Oceanogr* 51, 159–172. <https://doi.org/10.1016/j.dsr2.2003.07.016>
- Garzoli SL (1993) Geostrophic velocity and transport variability in the Brazil-Malvinas Confluence. *Deep Res Part I* 40, 1379–1403. [https://doi.org/10.1016/0967-0637\(93\)90118-M](https://doi.org/10.1016/0967-0637(93)90118-M)
- Garzoli SL, Garraffo Z (1989) Transports, frontal motions and eddies at the Brazil-Malvinas currents confluence. *Deep Sea Res Part A Oceanogr Res Pap.* 36, 681–703. [https://doi.org/10.1016/0198-0149\(89\)90145-3](https://doi.org/10.1016/0198-0149(89)90145-3)
- Garzoli SL, Gordon AL (1996) Origins and variability of the Benguela Current. *J Geophys Res* 101, 897–906.
- Garzoli SL, Richardson P.L, Duncombe Rae CM, Fratantoni DM, Goñi GJ, Roubicek AJ (1999) Three Agulhas rings observed during the Benguela Current Experiment. *J Geophys Res Ocean* 104, 20971–20985. <https://doi.org/10.1029/1999JC900060>
- Goes M, Cirano M, Mata MM, Majumder S (2019) Long-Term Monitoring of the Brazil Current Transport at 22°S From XBT and Altimetry Data: Seasonal, Interannual, and Extreme Variability. *J Geophys Res Ocean* 124, 3645–3663. <https://doi.org/10.1029/2018JC014809>
- Gonzalez-Rodriguez E (1994) Yearly variation in primary productivity of marine phytoplankton from Cabo Frio (RJ, Brazil) region. *Hydrobiologia* 294, 145–156. <https://doi.org/10.1007/BF00016855>
- Gonzalez-rodriguez E, Valentin JL, Andre DL, Paulo A, Rua M (1992) Upwelling and down welling at Cabo Frio ( Brazil ): comparison of biomass and primary production responses. *J Plank Res* 14, 289–306.

- Haarsma RJ, Campos EJD, Hazeleger W, Severijns C, Piola AR, Molteni F (2005) Dominant modes of variability in the South Atlantic: A study with a hierarchy of ocean-atmosphere models. *J Clim* 18, 1719–1735. <https://doi.org/10.1175/JCLI3370.1>
- Haarsma RJ, Campos EJD, Molteni F (2003) Atmospheric response to South Atlantic SST dipole. *Geophys Res Lett* 30, 2–5. <https://doi.org/10.1029/2003GL017829>
- Hutchings L, Jarre A, Lamont T, van den Berg M, Kirkman SP (2012) St Helena Bay (southern Benguela) then and now: Muted climate signals, large human impact. *African J Mar Sci* 34, 559–583. <https://doi.org/10.2989/1814232X.2012.689672>
- Hutchings L, van der Lingen CD, Shannon LJ, Crawford RJM, Verheye HMS, Bartholomae CH, van der Plas AK, Louw D, Kreiner A, Ostrowski M, Fidel Q, Barlow RG, Lamont T, Coetzee J, Shillington F, Veitch J, Currie JC, Monteiro PMS (2009) The Benguela Current: An ecosystem of four components. *Prog Oceanogr* 83, 15–32. <https://doi.org/10.1016/j.pocean.2009.07.046>
- Jing Z, Qi Y, Du Y (2011) Upwelling in the continental shelf of northern South China Sea associated with 1997–1998 El Niño. *J Geophys Res Ocean* 116, 1–11. <https://doi.org/10.1029/2010JC006598>
- Lamont T, García-Reyes M, Bograd SJ, van der Lingen CD, Sydeman WJ (2017) Upwelling indices for comparative ecosystem studies: Variability in the Benguela Upwelling System. *J Mar Syst* 188, 3–16. <https://doi.org/10.1016/j.jmarsys.2017.05.007>
- Lopes RM, Katsuragawa M, Dias JF, Montú MA, Muelbert JH, Gorri C, Brandini FP (2006) Zooplankton and ichthyoplankton distribution on the southern Brazilian shelf: An overview. *Sci Mar* 70, 189–202. <https://doi.org/10.3989/scimar.2006.70n2189>
- Mackas D, Strub P, Thomas A, Montecino V (2006) Eastern ocean boundaries pan-regional overview. *Sea* 14 21–59.
- Mann KH, Lazier JRN (2005) Dynamics of Marine Ecosystems, Dynamics of Marine Ecosystems. <https://doi.org/10.1002/9781118687901>
- Marcello F, Wainer I, Rodrigues RR (2018) South Atlantic Subtropical Gyre Late Twentieth Century Changes. *J Geophys Res Ocean* 123, 5194–5209. <https://doi.org/10.1029/2018JC013815>
- Mazzini PLF, Barth JA (2013) A comparison of mechanisms generating vertical transport in the Brazilian coastal upwelling regions. *J Geophys Res Ocean* 118, 5977–5993. <https://doi.org/10.1002/2013JC008924>

- Meeuwis JM, Lutjeharms JR (1990) Surface thermal characteristics of the angola-benguela front. *South African J Mar Sci* 9, 261–279. <https://doi.org/10.2989/025776190784378772>
- Mogollón R, Calil PHR (2017) On the effects of ENSO on ocean biogeochemistry in the Northern Humboldt Current System (NHCS): A modeling study. *J Mar Syst* 172, 137–159. <https://doi.org/10.1016/j.jmarsys.2017.03.011>
- Möller OO, Piola AR, Freitas AC, Campos EJD (2008) The effects of river discharge and seasonal winds on the shelf off southeastern South America. *Cont Shelf Res* 28, 1607–1624. <https://doi.org/10.1016/j.csr.2008.03.012>
- Morioka Y, Tozuka T, Yamagata T (2011) On the growth and decay of the subtropical dipole mode in the South Atlantic. *J Clim* 24, 5538–5554. <https://doi.org/10.1175/2011JCLI4010.1>
- Nelson G, Hutchings L (1983) The Benguela upwelling area. *Prog Oceanogr* 12, 333–356. [https://doi.org/10.1016/0079-6611\(83\)90013-7](https://doi.org/10.1016/0079-6611(83)90013-7)
- Palastanga V, Vera CS, Piola AR (2002) On the Leading Modes of Sea Surface Temperature Variability in the South Atlantic Ocean. *CLIVAR Exch.* 25, 12–16.
- Palma ED, Matano RP (2009) Disentangling the upwelling mechanisms of the South Brazil Bight. *Cont Shelf Res* 29, 1525–1534. <https://doi.org/10.1016/j.csr.2009.04.002>
- Palma ED, Matano RP, Piola AR (2008) A numerical study of the Southwestern Atlantic Shelf circulation: Stratified ocean response to local and offshore forcing. *J Geophys Res Ocean* 113, 1–22. <https://doi.org/10.1029/2007JC004720>
- Peard KR (2007) Seasonal and interannual variability of wind-driven upwelling at Lüderitz, Namibia. University of Cape Town.
- Peterson RG, Stramma L (1991) Upper-level circulation in the South Atlantic. *Ocean Prog Oceanogr* 26, 1–73. [https://doi.org/10.1016/0079-6611\(91\)90006-8](https://doi.org/10.1016/0079-6611(91)90006-8)
- Pezzi LP, Cavalcanti IFA (2001) The relative importance of ENSO and tropical Atlantic sea surface temperature anomalies for seasonal precipitation over South America: a numerical study. *Clim Dyn* 17, 205–212. <https://doi.org/10.1007/s003820000104>
- Piola AR, Matano RP, Palma ED, Möller OO, Campos EJD (2005) The influence of the Plata River discharge on the western South Atlantic shelf. *Geophys Res Lett* 32, 1–4. <https://doi.org/10.1029/2004GL021638>
- Pitcher GC, Nelson G (2006) Characteristics of the surface boundary layer important to the development of red tide on the southern Namaqua shelf of the

- Benguela upwelling system. *Limnol Oceanogr* 51, 2660–2674. <https://doi.org/10.4319/lo.2006.51.6.2660>
- Rae CD (2005) A demonstration of the hydrographic partition of the Benguela upwelling ecosystem at 26°40'S. *African J Ma. Sci.* 27, 617–628. <https://doi.org/10.2989/18142320509504122>
- Reason CJC (1998) Warm and cold events in the Southeast Atlantic/Southwest Indian ocean region and potential impacts on circulation and rainfall over Southern Africa. *Meteorol Atmos Phys* 69, 49–65. <https://doi.org/10.1007/BF01025183>
- Riley GA (1942) The Relationship of Vertical Turbulence and Spring Diatom Flowerings. *J. Mar. Res.* 5, 67–87.
- Rodrigues RR, Campos EJD, Haarsma R (2015) The impact of ENSO on the south Atlantic subtropical dipole mode. *J Clim* 28, 2691–2705. <https://doi.org/10.1175/JCLI-D-14-00483.1>
- Rodrigues RR, Lorenzetti JA (2001) A numerical study of the effects of bottom topography and coastline geometry on the Southeast Brazilian coastal upwelling. *Cont Shelf Res* 21, 371–394. [https://doi.org/10.1016/S0278-4343\(00\)00094-7](https://doi.org/10.1016/S0278-4343(00)00094-7)
- Rouault M, Illig S, Bartholomae C, Reason CJC, Bentamy A (2007) Propagation and origin of warm anomalies in the Angola Benguela upwelling system in 2001. *J Mar Syst* 68, 473–488. <https://doi.org/10.1016/j.jmarsys.2006.11.010>
- Roux J.P, Shannon LJ (2004) Ecosystem approach to fisheries management in the northern Benguela: The Namibian experience. *African J Mar Sci.* 26, 79–93. <https://doi.org/10.2989/18142320409504051>
- Saji NH, Goswami PN, Vinayachandran PN, Yamagata, T (1999) Saji, N.A et al., dipole mode in the tropical Indian ocean. *Nat* 401, 360–363.
- Sankar S, Thondithala Ramachandran A, Franck Eitel KG, Kondrik D, Sen R, Madipally R, Pettersson LH (2019) The influence of tropical Indian Ocean warming and Indian Ocean Dipole on the surface chlorophyll concentration in the eastern Arabian Sea. *Biogeosciences Discuss* 1–23. <https://doi.org/10.5194/bg-2019-169>
- Shannon LV, Nelson G (1996) The Benguela: Large Scale Features and Processes and System Variability. *South Atl* 163–210. [https://doi.org/10.1007/978-3-642-80353-6\\_9](https://doi.org/10.1007/978-3-642-80353-6_9)
- Simpson JH, Allen CM, Morris NCG (1978) Fronts on the continental shelf. *J Geophys Res* 83, 4607. <https://doi.org/10.1029/JC083iC09p04607>

- Simpson JH, Bowers D (1981) Models of stratification and frontal movement in shelf seas. *Deep Sea Res Part A Oceanogr Res Pap* 28, 727–738. [https://doi.org/10.1016/0198-0149\(81\)90132-1](https://doi.org/10.1016/0198-0149(81)90132-1)
- Simpson JH, Sharples J (2012a). Physical forcing of the shelf seas: what drives the motion of ocean?, in: *Introduction to the Physical and Biological Oceanography of Shelf Seas*. Cambridge University Press, Cambridge, pp. 25–49. <https://doi.org/10.1017/CBO9781139034098.005>
- Simpson JH, Sharples J (2012b) Seasonal stratification and the spring bloom, in: *Introduction to the Physical and Biological Oceanography of Shelf Seas*. Cambridge University Press, Cambridge, pp. 173–204. <https://doi.org/10.1017/CBO9781139034098.009>
- Sterl A, Hazeleger W (2003) Coupled variability and air-sea interaction in the South Atlantic Ocean. *Clim Dyn* 21, 559–571. <https://doi.org/10.1007/s00382-003-0348-y>
- Stramma L, England M (1999) On the water masses and mean circulation of the South Atlantic Ocean. *J Geophys Res Ocean* 104. <https://doi.org/10.1029/1999JC900139>
- Sun X, Cook KH, Vizy EK (2017) The South Atlantic subtropical high: Climatology and interannual variability. *J Clim* 30, 3279–3296. <https://doi.org/10.1175/JCLI-D-16-0705.1>
- Sverdrup HU (1953) On conditions for the vernal blooming of phytoplankton. *ICES J Mar Sci* 18, 287–295. <https://doi.org/10.1093/icesjms/18.3.287>
- Talley LD, Pickard GL, Emery WJ, Swift JH (2011) *Dynamical Processes for Descriptive Ocean Circulation*. *Descr Phys Oceanogr* 1–72. <https://doi.org/10.1016/b978-0-7506-4552-2.10019-8>
- Tchikalanga P, Dengler M, Brandt P, Kopte R, Macuéria M, Coelho P, Ostrowski M, Keenlyside NS (2018) Eastern boundary circulation and hydrography off Angola building Angolan oceanographic capacities. *Bull Am Meteorol Soc* 99, 1589–1605. <https://doi.org/10.1175/BAMS-D-17-0197.1>
- Tim N, Zorita E, Hünicke B (2015) Decadal variability and trends of the Benguela upwelling system as simulated in a high-resolution ocean simulation. *Ocean Sci* 11, 483–502. <https://doi.org/10.5194/os-11-483-2015>
- Tomczak M, Godfrey S (2003) Chapter 14: The Atlantic Ocean. *Reg. Oceanogr. An Introd.* 2, 229–252. <https://doi.org/10.1016/B978-0-12-455521-1.50010-3>



- Veitch JA, Penven P (2017) The role of the Agulhas in the Benguela Current system: A numerical modeling approach. *J Geophys Res Ocean* 122, 3375–3393. <https://doi.org/10.1002/2016JC012247>
- Venegas SA, Mysak A, Straub DN (1996) variability in the South Atlantic. *Geophys Res Lett* 23, 2673–2676.
- Venegas SA, Mysak LA, Straub DN (1997) Atmosphere-ocean coupled variability in the South Atlantic. *J Clim* 10, 2904–2920. [https://doi.org/10.1175/1520-0442\(1997\)010<2904:AOCVIT>2.0.CO;2](https://doi.org/10.1175/1520-0442(1997)010<2904:AOCVIT>2.0.CO;2)
- Villar E, Farrant GK, Follows M, Garczarek L, Speich S, Audic S, Bittner L, Blanke B, Brum JR, Brunet C, Casotti R, Chase A, Dolan JR, D’Ortenzio F, Gattuso J-P, Grima N, Guidi L, Hill CN, Jahn O, Jamet J-L, Le Goff H, Lepoivre C, Malviya S, Pelletier E, Romagnan J-B, Roux S, Santini S, Scalco E, Schwenck SM, Tanaka A, Testor P, Vannier T, Vincent F, Zingone A, Dimier C, Picheral M, Searson S, Kandels-Lewis S, Acinas SG, Bork P, Boss E, de Vargas C, Gorsky G, Ogata H, Pesant S, Sullivan MB, Sunagawa S, Wincker P, Karsenti E, Bowler C, Not F, Hingamp P, Iudicone D (2015) Environmental characteristics of Agulhas rings affect interocean plankton transport. *Science* (80-. ). 348, 1261447–1261447. <https://doi.org/10.1126/science.1261447>
- Villas Bôas AB, Sato OT, Chaigneau A, Castelão GP (2015) The signature of mesoscale eddies on the air-sea turbulent heat fluxes in the South Atlantic Ocean. *Geophys Res Lett* 42, 1856–1862. <https://doi.org/10.1002/2015GL063105>
- Vizy EK, Cook KH (2016) Understanding long-term (1982–2013) multi-decadal change in the equatorial and subtropical South Atlantic climate. *Clim Dyn* 46, 2087–2113. <https://doi.org/10.1007/s00382-015-2691-1>
- Wainer I, Prado LF, Khodri M, Otto-Bliesner B (2014) Reconstruction of the south atlantic subtropical dipole index for the past 12,000 years from surface temperature proxy. *Sci Rep* 4, 1–8. <https://doi.org/10.1038/srep05291>
- Yoder JA, Kennelly MA (2003) Seasonal and ENSO variability in global ocean phytoplankton chlorophyll derived from 4 years of SeaWiFS measurements. *Global Biogeochem Cycles* 17, n/a-n/a. <https://doi.org/10.1029/2002gb001942>